# Modelling and inversion of time-lapse seismic data using scattering theory

**Kenneth Muhumuza**

Thesis for the degree of Master of Science in Petroleum Geophysics

DEPARTMENT OF EARTH SCIENCE

UNIVERSITY OF BERGEN

June 2015

My success was due to good luck, hard work, and support and advice from friends and mentors. But most importantly, it depended on me to keep trying after I had failed.

—**Mark Warner**

*Dedicated to*

**My Mum Adyeeri Kasamba Harriet and Dad Apuuli John Kairu.**

# Abstract

Waveform inversion methods can be used to obtain high-resolution images of the elastic and acoustic property changes of petroleum reservoirs under production, but remains computationally challenging. Efficient approximations in modelling the wavefield based on scattering approaches are desirable for solving time-lapse inversion problems and to test the settings in which they give accurate predictions. In this thesis, we are concerned with acoustic waveform modelling and inversion in frequency domain with emphasis on first-order scattering methods.

Key themes of review and discussion include the derivation of scattering problems using Green's function techniques; Born approximation, distorted-Born approximation, Distorted Born iterative T-matrix method (DBIT); and the concepts of seismic waveform inversion and its application to different approaches in time-lapse seismic imaging. We employ the Born approximation and distorted-Born to simulate time-lapse synthetic seismograms and test the settings in which these methods are valid by benchmarking them against the exact T-matrix approach. The new distorted-Born approximation presented considers a general heterogeneous reference medium and provides a framework for imaging of regions of time-lapse variation using the baseline survey as a reference and the monitor survey as perturbed to directly estimate the perturbation. This poses a linear inverse scattering problem for which suitable linear and non-linear inversion methods are applicable.

Synthetic testing based on different 2D models demonstrate that the new distorted-Born approximation provides accurate predictions of the difference data seismograms, at least in the settings considered while the Born approximation is limited to applications involving small volume and velocity contrasts. The inversion results show that Born inversion (in its limits) and DBIT method sufficiently retrieves the time-lapse velocity changes even in the cases of relatively low signal to noise ratio. Inversion of the difference data (differential approach) not only gives improved results but also proves to be useful and efficient since a single inversion procedure is performed for a pair of seismic experiments and hence computationally less expensive. The DBIT method which considers a dynamic background media and a variational T-matrix approach may be very useful in seismic characterisation of petroleum reservoirs under production and may be more efficient in monitoring of $CO_2$ sequestration.

# Acknowledgment

I would like to thank the Almighty Lord for the gift of life and for leading me through this tiresome exercise, in fact with God everything is possible.

There is a less obvious debt to the Earth Science Department at the University of Bergen where, under the different lecturers, I have received guidance and technical advice for this project and learning Geophysics in general.

I am indebted to my supervisor Professor Morten Jakobsen and co-supervisor Dr. Bent Ruud for their devoted help and professional advice that enabled me to learn a lot during the project work. I appreciate their vast knowledge and skills in the areas of seismic modelling and inversion. In particular, Prof. Morten Jakobsen introduced me to the world of scattering theory and his great efforts to explain things clearly and simply helped to make geophysical problems fun for me. He also shared his MATLAB code that has inspired my work on non-linear inversion.

I am grateful to a PhD student, Michael Ernesto Lopez for the many interesting discussions throughout the development of this work. He provided encouragement, sound advice, lots of good ideas and valuable help on my research.

Great thanks are due to my family members for the moral support and the Government of Norway for their financial support during the entire period of my Master's study and making this project a success.

Lastly, I wish to thank my parents who bore me, raised me, supported me, taught me, and showed me unending love.

# Contents

# List of Figures

# List of Tables

# List of Abbreviations

**2D** Two-dimensional

**3D** Three-dimensional

**CSG** Common-shot gather

**AVO** Amplitude Versus Offset

**AVA** Amplitude Versus Angle

**SNR** Signal to noise Ratio

**FWI** Full waveform inversion

**DBIT** Distorted Born iterative T-matrix

**DBI** Distorted Born iterative

# List of Symbols

| | |
|---|---|
| $\omega$ | temporal frequency |
| $t$ | travel time |
| $f$ | frequency |
| $\nabla$ | Laplacian operator |
| $\mathbf{d}$ | seismic data |
| $\mathbf{m}$ | the earth model |
| $\mathbf{m}_{est}$ | model estimate |
| $\boldsymbol{\eta}$ | additive noise |
| $\lambda$ | regularization parameter for inversion |
| $\mathbf{G}$ | forward modelling operator |
| $\mathbf{G}^{-1}$ | inverse operator |
| $\mathbf{G}^{T}$ | transpose operator |
| $\delta$ | Dirac delta function |
| $k$ | wave number |
| $G$ | Green's function |
| $\partial$ | partial derivative |
| $V_P$ | P-wave velocity |

# Chapter 1

# Introduction

Waveform inversion of time-lapse seismic data remains an important tool in line with reservoir characterization and monitoring. This diagnostic tool attempts to obtain the images of the subsurface parameters from the seismic data acquired from real seismic acquisition experiments or synthetic seismic data resulting from forward modelling. In this chapter we review the basic concepts of how seismic data is acquired and give an overview of seismic inversion and its application to time-lapse studies. We state the objectives for our work and summarise the thesis.

## 1.1   Introduction to exploration seismology

Exploration seismology attempts to improve the understanding of the Earth's interior, primarily the top few kilometres of the crust where most sub-surface natural resources are located. This is achieved by seismically imaging the earth's reflectivity distribution, a technique that involves recording and studying seismic waves that are excited by seismic sources. Seismic sources may be man-made such as mechanical devices and explosives or natural such as earthquakes (Aki and Richards, 2002). The goal of exploration seismology is to help discover and enhance production of natural resources, chiefly petroleum which is our subject of interest (e.g., Ikelle and Amundsen, 2005; Yilmaz, 2001; Sheriff and Geldart, 1995).

## 1.2   Seismic data acquisition

The collection of seismic data is a key concern for hydrocarbon exploration and it is therefore imperative that we describe how these data are acquired. The subject of seismic acquisition is given an in-depth treatment in hundreds of books (e.g., Zhou, 2014; Ashcroft, 2011; Liner, 2004; Vermeer and Beasley, 2002 and Yilmaz, 2001). Acquisition involves seismic surveys that can be conducted along lines to produce a vertical profile (2D survey) or over an area to generate a 3D sub-surface volume. In this thesis, simple 2D seismic survey configurations are considered. In 2D reflection seismic surveying both the sources and the receivers (numbering up to a hundred or more per shot) are moved along a straight line while in 3D reflection seismic surveying the sources and a dense array of receivers are moved on a given area .

In a seismic data acquisition experiment, acoustic energy is usually provided by controlled sources such as explosive charges or by large vibroseis trucks on land or by an air gun in marine surveys. The energy spreads out through the subsurface as a spherical wave front scattering in all directions. Interfaces between different types of rocks will both reflect and transmit this wave front. The reflected signals return to the surface where they are detected by receivers deployed along a pre-set geometry (called receiver array). Those receivers are called geophones for land surveys and hydrophones for marine surveys. They can record one or all three components of the vector of particle velocity or pressure in the case of a hydrophone. In this thesis, however, we have concentrated on the vertical component which consists of the compression (P) waves alone.

Figure 1.1 shows a sketch of a 2D seismic survey typical for a hydrocarbon exploration data acquisition experiment. The black arrows show the possible paths taken by the seismic energy. The reflected energy detected by the receiver groups is used to construct an image of the subsurface to investigate the underlying structure. Travel time information between source and receiver is particularly used to estimate the depth of each interface.

A pair of source-receiver generates a seismic trace and a set of traces recorded by all receivers for a given source is called a common-shot gather (CSG) or common-shot section. Another interesting form of gather is a common-offset gather. This can be viewed as a
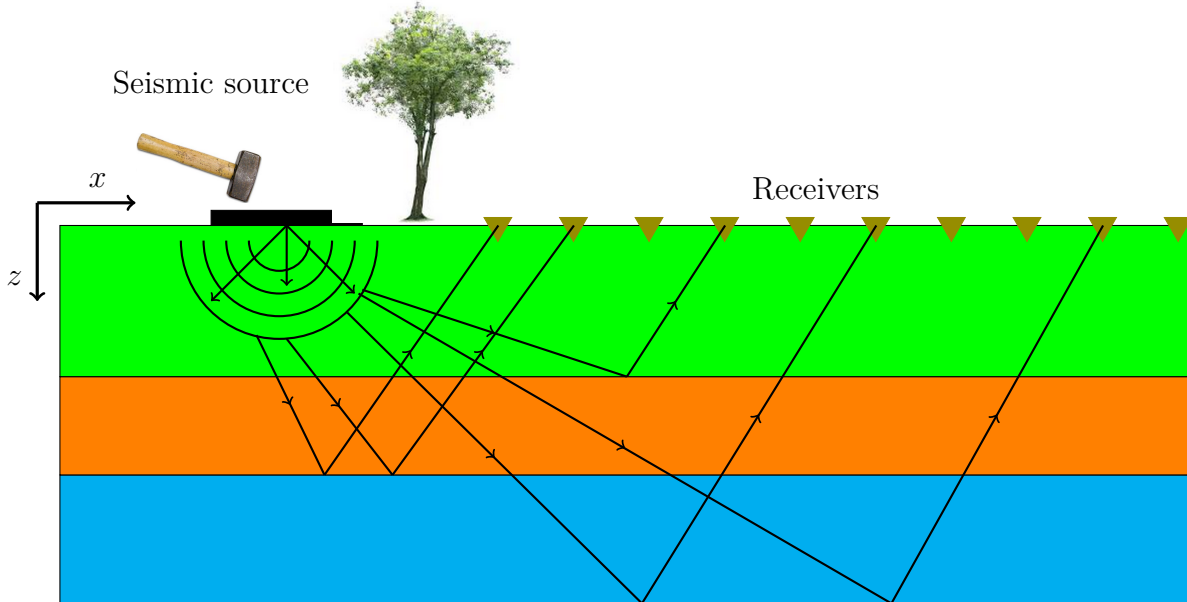
Figure 1.1: Sketch of a 2D seismic survey for data acquisition experiment: layer cake model, seismic energy (black arrows) is transmitted or reflected at interfaces between rock layers with different elastic properties.

synthetic seismic experiment which maintains a fixed source-receiver separation (offset) as they are moved as a pair along the seismic line.

The zero-offset seismic section where source and receiver points coincide is particularly important for exploration seismics; this presents the image of a geologic cross-section or depth section of geological interfaces. This type of gather can not be obtained directly by seismic reflection measurements but can be obtained by forward modelling or modelled from other seismic data. Figure 1.2 shows an illustration of the CSG used in this thesis and a corresponding hypothetical section of seismic traces expected. The details of all the different acquisition techniques and types of seismic gathers or sections and how they are obtained is not considered in this thesis.

## 1.3   Overview of seismic inversion

Seismic inversion is a useful technique for converting the acquired seismic data from the reflectivity domain (geological interface property) to the impedance domain (rock property). It is therefore helpful in the interpretation of the recorded seismic data by recovering the

(a) Common-shot arrangement          (b) Common-shot gather section
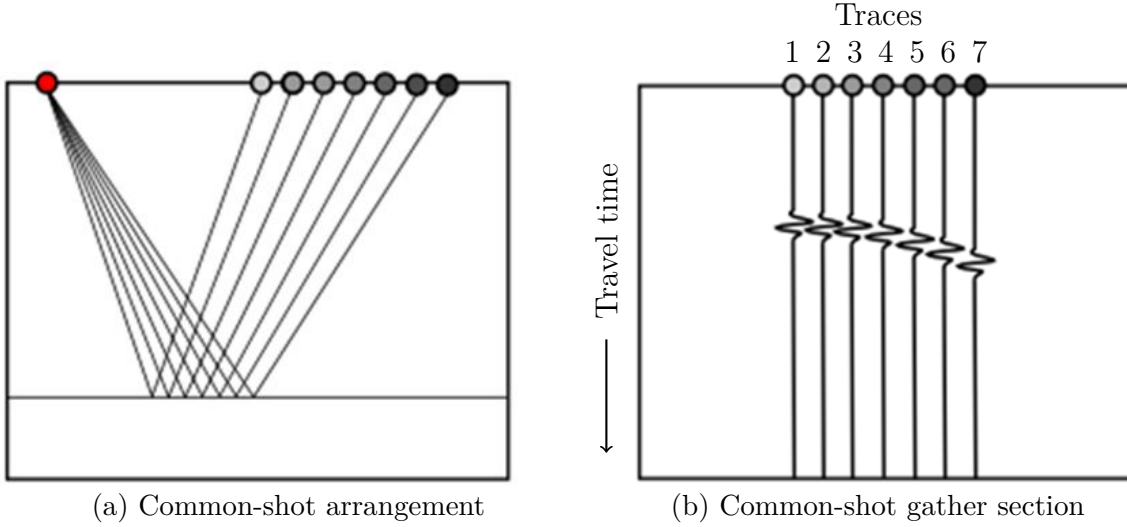
Figure 1.2: Simple illustration of common-shot gather measurements; this is the way the data is recorded.

2D or 3D map of the subsurface and in the quantitative estimation of the rock properties such as seismic velocities. In our study, we generate the synthetic seismic data using forward modelling in order to perform the inversion following the three steps which are summarised by Tarantola (2005). A seismic inverse problem can represented mathematically as,

$$\mathbf{d} = \mathbf{Gm} + \boldsymbol{\eta} \tag{1.1}$$

where $\mathbf{d}$ is an $N$ vector of recorded data such post-stack data, $\mathbf{m}$ is an $M$ vector of the model parameters such as acoustic velocities, $\mathbf{G}$ is an $N \times M$ matrix that describes the forward modelling operator for example the convolution operator and $\boldsymbol{\eta}$ denotes the quantified error (seismic noise) such as multiples or random noise. Our interest in a typical seismic inverse problem is to estimate the distribution of the model parameters $\mathbf{m}$, given $\mathbf{G}$ and a set of measurements $\mathbf{d}$. It is important to stress that $\mathbf{G}$, $\mathbf{m}$ and $\mathbf{d}$ will have different meanings, depending on the selection of the forward modelling operator, type of parametrization and type of data used for inversion. For instance, $\mathbf{G}$ represents an AVO/AVA forward modelling operator in AVO/AVA inversion (e.g., Downton, 2005; Buland and Omre, 2003; Simmons Jr and Backus, 1996) or a modelling operator like a de-migration operator for a migration/de-migration process (e.g, Symes and Kern, 1994; Santos et al., 2000). This thesis is based

on linear and non-linear waveform seismic inversion using the scattering approaches (Born, distorted-Born approximation and T-matrix) for the forward modelling problem. We attempt to retrieve the estimates of the acoustic velocities of the subsurface.

## 1.4 The value of time-lapse inversion

Time-lapse inversion is a further step beyond inversion of a single survey dataset. It involves reconstructing the difference image of the subsurface between repeated survey datasets obtained at different time spans over a producing reservoir. Assuming we have two datasets (baseline, $\mathbf{d}^1$, and a monitor, $\mathbf{d}^2$); the time-lapse inversion problem can be written as:

$$
\begin{aligned}
\mathbf{d}^1 &= \mathbf{G}^1(\mathbf{m}^1) + \boldsymbol{\eta}^1 \\
\mathbf{d}^2 &= \mathbf{G}^2(\mathbf{m}^2) + \boldsymbol{\eta}^2
\end{aligned}
\tag{1.2}
$$

where the superscripts denote the different time spans and $\mathbf{d}$, $\mathbf{m}$, $\mathbf{G}$ and $\boldsymbol{\eta}$ carry the same definitions as in Equation (1.1). When the baseline and monitor data acquisition geometries are similar, and there is a negligible change in the velocity of the modelling operator, then $\mathbf{G}^1 \sim \mathbf{G}^2$. The time-lapse inversion reconstructs and predicts $\mathbf{m}^1 - \mathbf{m}^2$ from the seismic data $\mathbf{d}^1$ and $\mathbf{d}^2$.

Time-lapse inversion can be used to estimate changes in elastic parameters of petroleum reservoirs under production, which can be linked to modifications in geomechanical conditions and fluid changes in the subsurface. Analysis of the time-lapse image can illuminate these changes of reservoir properties, and therefore inversion of time-lapse data has strong potential in connection with reservoir management and well-planning. All published work on time-lapse seismic waveform inversion technique highlight the value of the method in tracking subsurface changes qualitatively and quantitatively. For example, Queißer and Singh (2013), Plessix et al. (2010) recognise the efficiency of the technique in constructing time-lapse velocity models; Ayeni et al. (2012) present a case study where the technique attenuates artifacts caused by differences in the acquisition geometries between monitoring surveys; and Johnston (2013) outlines the benefits of time-lapse elastic inversion in connection to seismic interpretation.

A time-lapse inversion study also relies on how the two datasets in Equation (1.2) are integrated during the inversion. For example, Sarkar et al. (2003) discussed three time-lapse inversion work flows that involve different ways of integrating the datasets and referred to them as uncoupled inversion, coupled inversion and inversion of difference. Abubakar et al. (2003) also studied two strategies of inversion (inverting the baseline and monitor survey separately and inversion of difference data) and concluded that the former is more preferred. These time-lapse strategies in connection to waveform inversion which are part of our investigations in this thesis are further discussed in Chapter 4.

Using rock physics inversion models, one can relate changes in elastic parameters to static and dynamic parameters of the reservoir, such as porosity, saturation and pressure. Much research have been done on seismic time-lapse inversion to monitor reservoir changes in pressure, saturation and porosity. The review of these methodologies and value are not considered because the main focus of this thesis is on the initial step of the time-lapse inversion; mapping the changes in seismic waveforms into a time-lapse velocity model.

## 1.5   Thesis objectives

This thesis presents methods for modelling and inversion of time-lapse seismic waveform data using scattering approaches. It will investigate the use of different background media in modelling seismic data using the Born approximation and distorted-Born approximation and regularization methods for the ill-posed inverse problem. The objective of the thesis is to study the acoustic forward modelling of time-lapse seismic data and conduct linear and non-linear inversion based on scattering approximations to investigate the possibility of utilising scattering approaches for characterisation of time-lapse phenomena. The other objective of the thesis is to investigate the pros and cons of the sequential and differential strategies to time lapse seismic. The objectives will be achieved by performing a series of numerical experiments implemented using seismic forward modelling methods based on the Born approximation, distorted-Born approximation and T-matrix approach. The inversion schemes will be tested using synthetic data.

## 1.6 Thesis overview

The thesis consists of five chapters and its structure is such that each of the chapters containing numerical examples or experiments is treated as independent with an introduction, methodologies and conclusion or summary. The current chapter, Chapter 1, gives an overview of exploration seismology, seismic inversion and its application to time-lapse studies. We briefly review the work done by other scholars especially on inversion and finally provide the objectives of the thesis.

Chapter 2 gives a theoretical knowledge of seismic modelling using the acoustic and elastic wave equation. We derive and discuss the forward modelling formulations in relation to first order scattering approach also known as the Born approximation in the acoustic case. We also discuss the distorted-Born approximation which presents possibilities of incorporating realistic background models to improve the Born approximation modelling results. The theory presented is implemented using numerical examples. We generate synthetic time-lapse seismograms by considering simple 2D models using a homogeneous background and investigate the use of a heterogeneous background medium for modelling time-lapse seismograms.

Chapter 3 deals with the fundamentals of geophysical inversion theory. A brief overview of regularization techniques and different methods employed to solve ill-posed inversion problems is presented. The emphasis in this chapter is put on the least squares method and Tikhonov regularisation technique. We then show the major concepts presented by a simple numerical example.

In chapter 4, we focus on time-lapse inversion. We discuss Born inversion which is a linearized inversion approach and also discuss DBIT method which is a non-linear scattering approach. We try to reconstruct the models provided in chapter 2 and apply the different inversion strategies to characterize velocity-time lapse changes. We compare results obtained and discussed the advantages and limitations of each strategy.

Chapter 5 gives a summary of the research work and also presents important findings that are relevant to the thesis objectives. We will also provide a discussion of the important extensions that can be considered for future research work.

# Chapter 2

# Seismic Forward Modelling in the Acoustic Approximation

## 2.1 Introduction

Seismic forward modelling is the process of generating synthetic seismograms by simulating seismic energy propagation through a hypothetical geological model (Sayers and Chopra, 2009; Chopra et al., 2005; Krebes, 2004). The geological model may be computed from geological information (for example from well logs) of real seismic or algorithms of equations defining the subsurface properties. Seismic forward modelling has been widely used in both earthquake seismology and seismic exploration. In this study, we are concerned with the latter. Applications of seismic forward modelling that include; seismic data acquisition design, testing seismic processing and imaging methods, interpretation of seismic data are discussed by, among others, Alaei (2012) and Sayers and Chopra (2009). Our focus in this work are the applications related to imaging, i.e., using the generated seismic data to reconstruct the image of the subsurface.

Synthetic seismograms for a given earth model and acquisition design (source configuration and receiver geometry), can be computed by seismic forward modelling. Various modelling techniques that include; finite difference (e.g., Kelly et al., 1976; Robertsson and Chapman, 2000; Liu and Sen, 2009), ray theory (e.g., Červený, 2001; Hearn and Krebes, 1990), Born

approximation (e.g., Chapman, 2004; Jakobsen, 2012; Ikelle and Amundsen, 2005; Kirchner and Shapiro, 2001), ray-born (e.g., Červenỳ, 1992; Minakov et al., 2013) and finite element (e.g., Komatitsch and Vilotte, 1998; De Basabe and Sen, 2009; Komatitsch and Tromp, 1999) have been previously used to generate synthetic data that is a representative of the subsurface model response. In addition, AVO/AVA methods that involve analysing amplitude variation with offset/angle have been widely used to model seismic response in order to detect changes in fluid content and lithology of the subsurface structures (e.g., Li et al., 2007; Xu and Bancroft, 1997; Rüger, 2001). These AVO/AVA methods whose underlying principles follow from the Zoeppritz equations are not considered in our work.

In seismic time-lapse applications, we can estimate changes in seismic response corresponding to the same strata at different time intervals. This results into time-lapse (difference) seismograms that can be used to quantitatively study the changes in the subsurface properties. It is important to note that the technique chosen in the modelling dictate the accuracy of the synthetic seismograms and the computational time, depending on the complexity of the model and computer hardware resources. Acoustic modelling is computationally relatively simple and quick but with several uncertainties attached such as the failure to account for the effects of lateral velocity changes and effects that result to attenuation. Since Born modelling is good for complex structures, we expect it to perform well in modelling time-lapse data especially if the background media can be improved to be close to the actual medium.

In this chapter we derive the Lippmann-Schwinger equation, the Born approximation formulation and the distorted-Born approximation, and use the techniques to generate time-lapse synthetic data. We also discuss how to implement the Born integral in the case of multiple sources and frequencies. We generate synthetic time-lapse seismic waveform data using the Born and distorted-Born approximations for different simple subsurface models and background media. We study the effect of the reference medium on the time-lapse seismograms. In all our numerical examples, we use an acoustic approach defined by the scalar (simplest) wave equation (next section) as our starting point for seismic forward modelling. We conclude the chapter by suggesting ideas for further work.

## 2.2   The seismic wave equation

The wave equation is the starting point for modelling seismic data based on various earth models representing different media complexities. Accurate seismic wavefield may be modelled by considering the elastic wave equation

$$\rho \frac{\partial^2 \mathbf{u}}{\partial t^2}(\mathbf{x}, t) - \nabla \cdot \boldsymbol{\sigma}(\mathbf{x}, t) = F(\mathbf{x}, t), \tag{2.1}$$

where the displacement field $\mathbf{u}$ ,the mass density $\rho$, the stress tensor $\boldsymbol{\sigma}$ and external force $F$ (representing the seismic source) are functions of spatial position. Using index notation, the stress tensor $\sigma_{ij}$ is related to the strain tensor $\epsilon_{kl}$ for a general elastic media by the equation,

$$\sigma_{ij} = C_{ijkl}\epsilon_{kl} \qquad\qquad i, j, l = x, y, z. \tag{2.2}$$

The components of $C_{ijkl}$ are the elastic constants that describe elastic properties of the medium and their number will depend on whether the Earth model is treated as isotropic or anisotropic.

In most seismic experiments, modelling of reflection seismic data is achieved by assuming that the subsurface rocks behave acoustically in order to simplify the algorithms and reduce the computational burden (e.g., Prieux et al., 2009; Jakobsen et al., 2010; Ayeni and Biondi, 2010; Jakobsen, 2012). In the acoustic approximation, only P-waves are modelled and the earth is assumed to have a constant density such that the wave propagation is described by the acoustic wave equation:

$$\nabla^2 P(\mathbf{x}, \mathbf{x}_s, t) - \frac{1}{c^2(\mathbf{x})} \frac{\partial^2}{\partial t^2} P(\mathbf{x}, \mathbf{x}_s, t) = -F_s(\mathbf{x}, \mathbf{x}_s, t), \tag{2.3}$$

where $P(\mathbf{x}, \mathbf{x}_s, t)$ is the acoustic pressure field as a function of position $\mathbf{x}$ and time $t$, $c(\mathbf{x})$ is the acoustic wave velocity and $F_s(\mathbf{x}_s, t)$ is the strength of source pulse at position $\mathbf{x}_s$. The acoustic wave equation is used in this study since it is easier to implement (computationally inexpensive) compared to the elastic equation. Moreover, the latter is ably approached to solve realistic problems involving elastic wave propagation in inelastic materials when the

former is well understood. In addition, modelling of acoustic wave propagation is not only computationally efficient but also a good starting point for generating various inversion algorithms suitable for solving inverse problems (Klie and Toro, 2000). A particular inverse problem is recovering the acoustic velocity of the media that the waves have propagated through by inverting the recorded data.

Equation (2.3) can be transformed to the frequency domain by applying the inverse Fourier transform and be written as the Helmholtz equation

$$\nabla^2 p(\mathbf{x}, \mathbf{x}_s, \omega) + k^2(\mathbf{x}, \omega) p(\mathbf{x}, \mathbf{x}_s, \omega) = -f_s(\mathbf{x}_s, \omega), \tag{2.4}$$

where $\omega$ is the angular frequency, $f_s(\mathbf{x}_s, \omega)$ is the Fourier transform of $F_s(\mathbf{x}_s, t)$ and the term $k(\mathbf{x}, \omega)$ is the wave number at position $\mathbf{x}$ defined by

$$k(\mathbf{x}, \omega) = \frac{\omega}{c(\mathbf{x})} \tag{2.5}$$

A fundamental solution to Equation (2.4) known as the Green's function exists for a unique case in which the source is a point impulse. Thus, the Green's function in a medium with constant velocity $c$ is the solution to Equation (2.4) if we replace the right-hand side with a point-source such that:

$$\nabla^2 G(\mathbf{x}, \mathbf{x}_s, \omega) + \frac{\omega^2}{c^2} G(\mathbf{x}, \mathbf{x}_s, \omega) = -\delta(\mathbf{x} - \mathbf{x}_s) \tag{2.6}$$

where $G(\mathbf{x}, \mathbf{x}_s, \omega)$ is the Green's function at location $\mathbf{x}$ due to a source at location $\mathbf{x}_s$ and the term $\delta(\mathbf{x} - \mathbf{x}_s)$ represents the point-source given theoretically by the Dirac delta function $\delta$ acting at location $\mathbf{x}_s$ at time $t = 0$. The Green's function allows us to describe wave propagation and represent the corresponding wavefield by the volume integral as a convolution of the Green's function with a band-limited source function. In this case, integrating all over all the space $V$ results into the integral representation formula of the pressure field (Morse and Feshbach, 1953):

$$p(\mathbf{x}, \omega) = \int G(\mathbf{x}, \mathbf{x}_s, \omega) f_s(\mathbf{x}, \omega) d\mathbf{x} d\omega \tag{2.7}$$

The explicit expressions of Green's functions in one, two or three dimensions useful in solving the Helmholtz equation for the case of homogeneous media are given in Snieder (2009). For a one-dimensional (1D) case, we have

$$G^{1D}(x, x_s) = \frac{-i}{2k} e^{ik(x-x_s)} \tag{2.8}$$

For a two-dimensional (2D) case, we have

$$G^{2D}(x, x_s) = \frac{-i}{4} H_0^{(1)}(k |\mathbf{x} - \mathbf{x}_s|) \tag{2.9}$$

where $H_0^{(1)}$ is the zero-order Hankel function of the first kind. For a three-dimensional (3D) case, we have

$$G^{3D}(x, x_s) = \frac{1}{4\pi} \frac{e^{-ik|\mathbf{x}-\mathbf{x}_s|}}{|\mathbf{x} - \mathbf{x}_s|} \tag{2.10}$$

Useful symmetrical properties of the Green's function such as the reciprocity property is important in studying scattering problems. If $\mathbf{x}_1$ and $\mathbf{x}_2$ are two source points inside some volume $V$ enclosed by a surface $\delta V$ and $G(\mathbf{x}_1, \mathbf{x}_2, \omega)$ shows the value of the Green's function at location $\mathbf{x}_1$ for a source point $\mathbf{x}_2$ and surface $\delta V$, then:

$$G(\mathbf{x}_1, \mathbf{x}_2, \omega) = G(\mathbf{x}_2, \mathbf{x}_1, \omega) \tag{2.11}$$

Equation (2.11) implies that the Green's function remains the same when a wave propagates from the source to the receiver or vice versa. This makes it possible to interchange the source and receiver positions in order to generate the incoming or outgoing-wave Green function. The reciprocal relation is valid when monopole point sources are used and the boundary surface $\delta V$ is a closed surface on which the solution (acoustic field) vanishes. It is also important to note that for generally varying velocity, the construction of the Green's function becomes complicated since symmetry properties are lost but some useful approximations simplify the problem. The discussion of the general solution to Equation (2.4) in the Fourier domain based on scattering follows in the next two sections. This is our basis for acoustic waveform modelling and inversion.

## 2.3 The Lippmann-Schwinger equation

The Lippmann-Schwinger equation makes it possible to solve Equation (2.4) and is very important in scattering theory (Ikelle and Amundsen, 2005). To solve the wave scattering problem, we assume that the Earth's properties can be represented as weak perturbations added to a simpler background model. The Earth's property of our interest is velocity. Thus, we can separate the velocity model $c(\mathbf{x})$ into a slowly varying background model $c_0(\mathbf{x})$ and a perturbation model $c_1(\mathbf{x})$.

$$c(\mathbf{x}) = c_0(\mathbf{x}) + c_1(\mathbf{x}) \tag{2.12}$$

The scattering occurs when a wave propagating from the source through the background model $c_0$ interacts with a scatterer (a contrast between the background and perturbation model) at a point $\mathbf{x}'$ within the scattering volume. The wave is then backscattered and propagates from $\mathbf{x}'$ through the background model to the receiver as illustrated in Figure 2.1. Each point scatterer may be considered as a secondary source of seismic energy. Multiple scatterings are ignored to linearize the Lippmann-Schwinger equation as noted in the next section.

We now work in the frequency domain and follow the treatment given in Lo and Inderwiesen (1994) and Moser (2012) to derive the Lippmann-Schwinger equation and deduce the Born forward formulation equation thereafter. We begin by recognising that the total wavefield $p(\mathbf{x}, \mathbf{x}_s, \omega)$ recorded by the receiver can also be separated into the background wavefield $p^{(0)}(\mathbf{x}, \mathbf{x}_s, \omega)$ and the scattered wavefield $p^{(1)}(\mathbf{x}, \mathbf{x}_s, \omega)$ such that

$$p(\mathbf{x}, \mathbf{x}_s, \omega) = p^{(0)}(\mathbf{x}, \mathbf{x}_s, \omega) + p^{(1)}(\mathbf{x}, \mathbf{x}_s, \omega). \tag{2.13}$$

$p^{(0)}(\mathbf{x}, \omega)$ is the solution to Equation (2.4) when the perturbation $c_1(\mathbf{x}) = 0$ implying that there is no contrast. In this case, Equation (2.4) can be written as:

$$\left[\nabla^2 + k_0^2\right] p^{(0)}(\mathbf{x}, \mathbf{x}_s, \omega) = -f_s(\mathbf{x}_s, \omega) \tag{2.14}$$

where $k_0$ is the known wave number that characterises the homogeneous background model,

its magnitude given by

$$k_0 = \frac{\omega}{c_0} \tag{2.15}$$
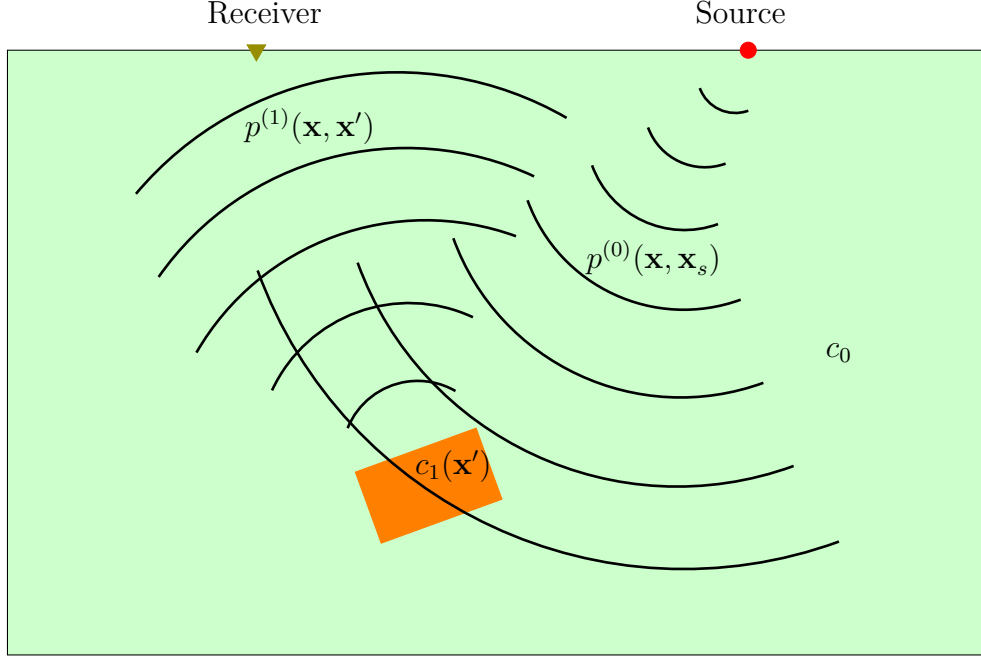


Figure 2.1: Seismic wave scattering problem: The wave $p^{(0)}(\mathbf{x}, \mathbf{x}_s)$ propagates from the source at the constant background velocity $c_0$ until it interacts with a scatterer (inhomogeneity with velocity $c_1$) which acts as a secondary source and scatterers the incoming wavefield. The scattered wavefield $p^{(1)}(\mathbf{x}, \mathbf{x}')$ propagates from the scatter point at the background velocity $c_0$ and is recorded by the receiver.

With the Green's function $G^{(0)}(\mathbf{x}, \mathbf{x}_s, \omega)$ for the homogeneous background model known, the solution to Equation (2.14) is found by a convolution integral and is given as:

$$p^{(0)}(\mathbf{x}, \mathbf{x}_s, \omega) = \int G^{(0)}(\mathbf{x}, \mathbf{x}_s, \omega) f_s(\mathbf{x}_s, \omega) d\mathbf{x} \tag{2.16}$$

For a constant density model, Equation (2.4) describes the propagation of the total recorded wavefield $p(\mathbf{x}, \mathbf{x}_s, \omega)$ through a heterogeneous medium, or

$$\left[ \nabla^2 + k^2(\mathbf{x}, \omega) \right] p(\mathbf{x}, \mathbf{x}_s, \omega) = -f_s(\mathbf{x}_s, \omega) \tag{2.17}$$

If we now express the wave number $k^2(\mathbf{x}, \omega)$ in Equation (2.17) as a perturbation to the wave

number $k_0$ for the background model (Lo and Inderwiesen, 1994) we obtain the result

$$
\begin{aligned}
k^2(\mathbf{x}, \omega) &= k_0^2 + \left[ k^2(\mathbf{x}, \omega) - k_0^2 \right] \\
&= k_0^2 + k_0^2 \left[ \frac{k^2(\mathbf{x}, \omega)}{k_0^2} - 1 \right].
\end{aligned}
\tag{2.18}
$$

The terms $k(\mathbf{x}, \omega)$ and $k_0$ in the the right-hand side brackets of Equation (2.18) can be substituted by Equation (2.5) and (2.15) respectively to obtain

$$
k^2(\mathbf{x}, \omega) = k_0^2 + k_0^2 \left[ \frac{c_0^2}{c^2(\mathbf{x})} - 1 \right].
\tag{2.19}
$$

If we define the bracketed term in Equation (2.19) as the model function (scattering potential) $m(\mathbf{x})$ (see Lo and Inderwiesen, 1994; Ikelle and Amundsen, 2005), the the term $k^2(\mathbf{x}, \omega)$ can be expressed in terms of the model perturbation as

$$
k^2(\mathbf{x}, \omega) = k_0^2 + k_0^2 m(\mathbf{x}),
\tag{2.20}
$$

where $m(\mathbf{x})$ is defined by

$$
m(\mathbf{x}) = \frac{c_0^2}{c^2(\mathbf{x})} - 1.
\tag{2.21}
$$

The model parameter $m$ quantifies the velocity contrasts between the background model and the actual model. By inverting for $m$, the original velocity model $c(\mathbf{x})$ can be recovered. This treatment is considered in Chapter 4.

We can now insert Equations (2.13) and (2.20) in Equation (2.17) to establish a relationship between the scattered wavefield $p^{(1)}(\mathbf{x}, \mathbf{x}_s, \omega)$ and the model function $m(\mathbf{x})$; i.e.,

$$
\left[ \nabla^2 + k_0^2 + k_0^2 m(\mathbf{x}) \right] \left[ p^{(0)}(\mathbf{x}, \mathbf{x}_s, \omega) + p^{(1)}(\mathbf{x}, \mathbf{x}_s, \omega) \right] = -f_s(\mathbf{x}_s, \omega)
\tag{2.22}
$$

Rearranging Equation (2.22) such that the terms containing the model function $m(\mathbf{x})$ are on one side and then subtracting the background wave (Equation (2.14)) results into

$$
\left[ \nabla^2 + k_0^2 \right] p^{(1)}(\mathbf{x}, \mathbf{x}_s, \omega) = -k_0^2 m(\mathbf{x}) \left[ p^{(0)}(\mathbf{x}, \mathbf{x}_s, \omega) + p^{(1)}(\mathbf{x}, \mathbf{x}_s, \omega) \right].
\tag{2.23}
$$

Using the right hand side of Equation (2.23) as the source, we can solve Equation (2.23) for $p^{(1)}(\mathbf{x}, \mathbf{x}_s, \omega)$ by an integral convolution using the properties of the Green's function discussed above. Thus,

$$p^{(1)}(\mathbf{x}, \mathbf{x}_s, \omega) = k_0^2 \int G^{(0)}(\mathbf{x}, \mathbf{x}_s, \omega) m(\mathbf{x}) \left[ p^{(0)}(\mathbf{x}, \mathbf{x}_s, \omega) + p^{(1)}(\mathbf{x}, \mathbf{x}_s, \omega) \right] d\mathbf{x} \qquad (2.24)$$

Equation (2.24) is often referred to as the Lippmann-Schwinger equation (e.g., Cohen and Bleistein, 1977; Lo and Inderwiesen, 1994; Ikelle and Amundsen, 2005; Stolt and Weglein, 2012). The equation relates the model function $m(\mathbf{x})$ to the data (scattered wavefield) $p^{(1)}(\mathbf{x}, \mathbf{x}_s, \omega)$ but also contains the total wavefield $p(\mathbf{x}, \mathbf{x}_s, \omega)$ which makes it non-linear. The non-linearity of Equation (2.24) makes it difficult to perform forward modelling since computationally extensive approaches need to be utilised. Linearising Equation (2.24) by assuming that the scattered wavefield $p^{(1)}(\mathbf{x}, \mathbf{x}_s, \omega)$ is sufficiently weaker than the incident wavefield $p^{(0)}(\mathbf{x}, \mathbf{x}_s, \omega)$ simplifies the problem and leads to the Born approximation.

## 2.4   The Born approximation

Born scattering theory allows us to formulate an approximate forward modelling problem by linearizing the well-known Lippmann-Schwinger equation (e.g., see Lo and Inderwiesen, 1994; Ikelle and Amundsen, 2005). The Born approximation which assumes single scattering has for long been used in seismic studies because it provides a linear approximation for inverse problems with easier systematic procedures. Linearising Equation (2.24) by assuming that the scattered wavefield $p^{(1)}(\mathbf{x}, \mathbf{x}_s, \omega)$ is sufficiently weaker than the incident wavefield $p^{(0)}(\mathbf{x}, \mathbf{x}_s, \omega)$ simplifies the problem. The assumption implies that

$$p^{(0)}(\mathbf{x}, \mathbf{x}_s, \omega) + p^{(1)}(\mathbf{x}, \mathbf{x}_s, \omega) \approx p^{(0)}(\mathbf{x}, \mathbf{x}_s, \omega). \qquad (2.25)$$

Substituting Equation (2.25) into Equation (2.24) results in the Born approximation formulation (e.g., Lo and Inderwiesen, 1994; Bleistein et al., 2001; Moser, 2012):

$$p^{(1)}(\mathbf{x}, \mathbf{x}_s, \omega) = k_0^2 \int G^{(0)}(\mathbf{x}, \mathbf{x}_s, \omega) m(\mathbf{x}) p^{(0)}(\mathbf{x}, \mathbf{x}_s, \omega) d\mathbf{x}. \qquad (2.26)$$

The right-hand side term in Equation (2.26) is the first order Born approximation for the scattered wave. For a point source at $\mathbf{x}_s$ and a receiver at $\mathbf{x}_r$, the incident wavefield $p^{(0)}(\mathbf{x}, \mathbf{x}_s, \omega)$ in Equation (2.26) can be represented by the Green's function $G^{(0)}(\mathbf{x}_r, \mathbf{x}, \omega)$ such that the Born approximation is given as:

$$p^{(1)}(\mathbf{x}_r, \mathbf{x}_s, \omega) = k_0^2 \int m(\mathbf{x}) G^{(0)}(\mathbf{x}, \mathbf{x}_s, \omega) G^{(0)}(\mathbf{x}_r, \mathbf{x}, \omega) d\mathbf{x}. \tag{2.27}$$

The implication of Equation (2.27) is that the data (scattered field) $p^{(1)}(\mathbf{x}_r, \mathbf{x}_s, \omega)$ and the unknown model function $m(\mathbf{x})$ are linearly related which makes linear inversion possible.

### 2.4.1 Some details for Implementation

The Born approximation result (integral Equation (2.26)) can be computationally implemented following an appropriate discretization scheme. Since a typical acquisition geometry for a seismic survey consists of multiple sources with a given frequency band width and receivers, discretizing the data integral involves dividing the survey area (reservoir) into grid cells and getting discrete values for sources, receivers and frequency spectrum. The size of each grid cell should be chosen small compared to the dominant wavelength and the highest frequency should be chosen such that aliasing is avoided. We follow the discretization formulation used in (Jakobsen et al., 2010).

Assuming the sources are located at positions $\mathbf{x}_s$, where $s = 1, ..., S$ and receivers at positions $\mathbf{x}_r$, where $r = 1, ..., R$, then the survey area can be discretized into a set of N grid cells representing the positions of scattering points $x'_n$ with $n = 1, ..., N$. Let the total volume of the scattering domain be denoted $dV$ and the scattering potential $m(\mathbf{x})$ by $m_n$. By considering discrete frequency values $w_w = w w_0$ where $w_0$ is the lowest frequency of the signal and $w = 1, ..., W$, the wave number $k_0 = k$, can be written as $k_w = \frac{w w_0}{c_0}$. The scattered wavefield $p_1(\mathbf{x}_r, \mathbf{x}_s, \omega)$ which is the data vector of our interest $d$ can be written in a discretized version by discretizing Equation (2.26) as:

$$d_{r,s,w} = \sum_{r=1}^{R} \sum_{s=1}^{S} \sum_{w=1}^{W} \left( \sum_{n=1}^{N} G_{r,s,n,w} m_n \right), \tag{2.28}$$

where $G_{r,s,n,w} = k_w^2 G_{r,n,w}^{(0)} p_{n,s,w}^{(0)} dV$ and $\mathbf{x}_r, \mathbf{x}_s, \omega$ have been replaced by indices $r, s, w$ respectively. We can now reduce the three indices $r, s, w$ to one index $j$, using the transformation:

$$r, s, w \rightarrow j = w + (s - 1) \times W + (r - 1) \times W \times S, \qquad j = 1, ...H = S \times R \times W, \quad (2.29)$$

and then Equation (2.28) can be written as a matrix multiplication with the new index $j$ such that:

$$d_j = \sum_{n=1}^{N} G_{j,n} m_n, \qquad \text{or} \qquad \mathbf{d} = \mathbf{Gm}, \tag{2.30}$$

which is the standard form of representing the relationship between the forward and inverse modelling problem (see Equations (1.1) and (3.1)). Equation (2.30) computes the Born approximation forward modelling data used for generating synthetic seismograms and is a linear inverse problem.

### 2.4.2    Validity of Born approximation

It is important to have an understanding of the domain of validity of the Born approximation technique when modelling in order to consider appropriate earth models applicable to this method. The validation conditions of Born approximation generally depend on the properties of the background medium and the scatterer. The validity of the method in relation to seismic modelling is assessed by, among others, Moser (2012), Wu and Xie (2009) and Ikelle and Amundsen (2005). In light of the assumption $p^{(1)}(\mathbf{x}, \mathbf{x}_s, \omega) \ll p^{(0)}(\mathbf{x}, \mathbf{x}_s, \omega))$ made in deriving Equation (2.26), it implies that the Born approximation becomes valid when there is presence of weak model contrasts, and the propagation distance is short. For a homogeneous background medium, these conditions are fulfilled if,

$$\left\| k_0^2 \int G^{(0)}(\mathbf{x}_r, \mathbf{x}, \omega) m(\mathbf{x}) d\mathbf{x} \right\| \ll 1. \tag{2.31}$$

Put simply, the background model used should be close to the perturbed (true) model to have the model function $m(\mathbf{x})$ as a weak scatterer. However, this consideration presents difficulties since we are assumed to know the wavefield in the background medium in terms of the Green's functions.

The Born approximation is also considered valid at low frequencies. However, this validity regime is not precisely defined for high frequency cases. Besides, when high-frequency asymptotic methods like ray theory are used to calculate the background Green's function, there exists no incompatibility with Born approximation. In fact, the assumptions of high frequency and small model contrasts are compatible for asymptotic ray theory (Bleistein et al., 2001). Taking the above into account, the low contrast condition (Equation (2.31)) remains the preferred criterion that ensures validity of the Born approximation.

Although the celebrated Born approximation with homogeneous background is widely used in many seismic studies to simplify forward modelling problems and linearize inverse problems, it has limitations especially in the time domain. The travel times for any (and every) seismic event are computed using the background velocity model and yet these are totally different from the travel times for the wave propagation in the actual medium. This gives rise to incorrect travel times from the forward series. Thus, the time domain is considered the domain of discomfort and space the domain of comfort for the Born approximation forward modelling (Weglein et al., 2003). In such cases, the use of the distorted-Born approximation (Chapman, 2004) which considers a heterogeneous background is particularly worthwhile because it reduces the travel time errors in modelling. In this thesis, we apply a homogeneous background model and extend the validity range by using a heterogeneous background medium in order to apply linear and non-linear inversion for time-lapse data.

## 2.5 Distorted-Born approximation

In order to extend the use of Born approximation to non-constant background models characterised by a wave number $k_0 = k(\mathbf{x})$ that varies with position, the approximate Green's function can be computed using ray theory (e.g., Moser, 2012; Thierry et al., 1998; Červenỳ, 2001) if the model is smooth. However, for any general heterogeneous background medium appropriate numerical methods such as the T-matrix (Jakobsen, 2012) and finite difference (Kirchner and Shapiro, 2001) can be used to compute the Green's functions $G(\mathbf{x}, \mathbf{x}_s, \omega)$ and $G(\mathbf{x}_r, \mathbf{x}, \omega)$ in the background model. In our work we generate approximate Green's function for a heterogeneous background medium based on the theory in Jakobsen and Ursin (2015)

which establishes a connection between the Green's functions $G(\mathbf{x}, \mathbf{x}')$ and $G^{(0)}(\mathbf{x}, \mathbf{x}')$ for the heterogeneous and homogeneous background media respectively through the so-called Dyson equation (Jakobsen and Ursin, 2015)

$$G(\mathbf{x}, \mathbf{x}') = G^{(0)}(\mathbf{x}, \mathbf{x}') + \int_\Omega d\mathbf{x}'' G^{(0)}(\mathbf{x}, \mathbf{x}'') \delta L(\mathbf{x}'') G(\mathbf{x}'', \mathbf{x}), \qquad (2.32)$$

where $\Omega$ denotes the domain where the scattering is non-zero and

$$\delta L(\mathbf{x}) = k_0^2 \left( \frac{1}{c^2(\mathbf{x})} - \frac{1}{c_0^2(\mathbf{x})} \right) \qquad (2.33)$$

represents the scattering potential of any heterogeneity at point $\mathbf{x}$. Equations (2.32) and (2.32) result from the treatment given in equations (2.7), (2.13), (2.15), (2.16) and (2.24). A scattering potential with a (non-normalized) contrast function $m(\mathbf{x})$ compatible with the use of a general heterogeneous background media is given by

$$\tilde{V}(\mathbf{x}_1, \mathbf{x}_2) = m(\mathbf{x}_1) \delta(\mathbf{x}_1, \mathbf{x}_2), \qquad (2.34)$$

where

$$m(\mathbf{x}) = \left( \frac{1}{c^2(\mathbf{x})} - \frac{1}{c_0^2(\mathbf{x})} \right). \qquad (2.35)$$

Following equations (2.24), (2.32), (2.33) and (2.34) we can rewrite the Lippmann-Schwinger and Dyson equations (2.24) and (2.32) for the total wavefield in the form of a product of matrices for ease in discretization (Jakobsen and Ursin, 2015) such that

$$p(\mathbf{x}) = p^{(0)}(\mathbf{x}, \mathbf{x}') + \int_\Omega d\mathbf{x}_1 \int_\Omega d\mathbf{x}_2 \bar{G}^{(0)}(\mathbf{x}, \mathbf{x}_2) \tilde{V}(\mathbf{x}_1, \mathbf{x}_2) p(\mathbf{x}_2), \qquad (2.36)$$

and

$$G(\mathbf{x}, \mathbf{x}') = \bar{G}^{(0)}(\mathbf{x}, \mathbf{x}') + \int_\Omega d\mathbf{x}_1 \int_\Omega d\mathbf{x}_2 \bar{G}^{(0)}(\mathbf{x}, \mathbf{x}_2) \tilde{V}(\mathbf{x}_1, \mathbf{x}_2) \bar{G}(\mathbf{x}_2, \mathbf{x}'), \qquad (2.37)$$

where $\bar{G}^{(0)}(\mathbf{x}, \mathbf{x}')$ is the modified Green's function that incorporate the $k_0^2$ factor to allow for the spatial variation of the scattering potential on the remaining portion of the interaction

(Kouri and Vijay, 2003) and is given by

$$\bar{G}^{(0)}(\mathbf{x}, \mathbf{x}') \equiv k_0^2 G^{(0)}(\mathbf{x}, \mathbf{x}'). \tag{2.38}$$

### 2.5.1 Discretization and Implementation

The Lippmann-Schwinger and Dysons equations (2.36) and (2.37) can be computationally implemented following an appropriate discretization scheme. We follow the discretization formulation used in Jakobsen and Ursin (2015).

Assuming the sources are located at positions $\mathbf{x}_s$, where $s = 1, ..., S$ and multiple receivers at positions $\mathbf{x}_r$, where $r = 1, ..., R$, then the target volume $\Omega$ with non-zero scattering potential $\delta L$ can be discretized into a set of N grid cells representing the positions of the scattering point with centroid $x_n$ with $n = 1, ..., N$. Note that the size of each grid cell should be chosen small compared to the dominant wavelength and the highest frequency should be chosen such that aliasing is avoided. Let the volume of each grid block be denoted $\delta v_n$ and the scattering potential $m(\mathbf{x})$ in equation (2.35) by $m_n$. If we introduce an index $l$ which may be associated with the field at a particular receiver position or inside a particular grid cell within the discretized scattering domain, then a discrete version of equations (2.35) and (2.37) can be written as

$$p_l = p_l^{(0)} + \sum_{n=1}^{N} \sum_{m=1}^{N} \bar{G}_{ln}^{(0)} V_{nm} p_m, \tag{2.39}$$

and

$$\bar{G}_{kl} = \bar{G}_{kl}^{(0)} + \sum_{n=1}^{N} \sum_{m=1}^{N} \bar{G}_{kl}^{(0)} V_{nm} \bar{G}_{ml}, \tag{2.40}$$

where $\delta_{nm}$ is the Kronecker-delta, defined by $\delta_{nm} = 1$ if $n = m$ and $\delta_{nm} = 0$ if $n \neq m$ and

$$V_{nm} = m_n \delta_{nm} \delta v_m. \tag{2.41}$$

For a discretized scattering volume (V) and receivers (R), the wavefields (including the reference field) can be arranged into vectors $\mathbf{P}_R(\mathbf{p}_R^{(0)})$ and $\mathbf{P}_V(\mathbf{p}_V^{(0)})$ that represent the wavefield at the

receiver surfaces and within the scattering domain such that equation (2.39) leads to

$$\mathbf{P}_R = \mathbf{P}_R^{(0)} + \bar{\mathbf{G}}_{RV}^{(0)} \mathbf{V} \mathbf{P}_V, \tag{2.42}$$

$$\mathbf{P}_V = \mathbf{P}_V^{(0)} + \bar{\mathbf{G}}_{VV}^{(0)} \mathbf{V} \mathbf{P}_V, \tag{2.43}$$

where $\mathbf{V}$ is a diagonal matrix with the scattering potential for a heterogeneous model. In a similar manner equation (2.40) leads to

$$\mathbf{P}_R = \mathbf{P}_R^{(0)} + \bar{\mathbf{G}}_{RV}^{(0)} \mathbf{V} \mathbf{P}_V, \tag{2.44}$$

$$\bar{\mathbf{G}}_{RV} = \bar{\mathbf{G}}_{RV}^{(0)} + \bar{\mathbf{G}}_{RV}^{(0)} \mathbf{V} \bar{\mathbf{G}}_{VV}, \tag{2.45}$$

$$\bar{\mathbf{G}}_{VV} = \bar{\mathbf{G}}_{VV}^{(0)} + \bar{\mathbf{G}}_{RV}^{(0)} \mathbf{V} \bar{\mathbf{G}}_{VV}, \tag{2.46}$$

The matrices considered in equations (2.42)–(2.46) are source-independent and contain the modified Green's function introduced in equation (2.38).

Following equation (2.42), the source-dependent relations for the data and domain equations can be expressed through source-receiver Green function matrices $\mathbf{G}_{RS}^{(0)}$ and $\mathbf{G}_{RS}$ given by (Jakobsen and Ursin, 2015)

$$\mathbf{G}_{RS} = \mathbf{G}_{RS}^{(0)} + \bar{\mathbf{G}}_{RV}^{(0)} \mathbf{V} \mathbf{G}_{VS} \tag{2.47}$$

where the corresponding matrices $\mathbf{G}_{VS}^{(0)}$ and $\mathbf{G}_{VS}$ as noted in equation (2.43) are related by

$$\mathbf{G}_{VS} = \mathbf{G}_{VS}^{(0)} + \bar{\mathbf{G}}_{VV}^{(0)} \mathbf{V} \mathbf{G}_{VS}. \tag{2.48}$$

The components of the $R \times S$ matrix $\bar{\mathbf{G}}_{RS}^{(0)}$ in equation (2.47) is associated with source positions $\mathbf{x}_s$, where $s = 1, ..., S$ and one receiver position $\mathbf{x}_r$, where $r = 1, ..., R$. Similarly, the components of the $N \times S$ matrix $\bar{\mathbf{G}}_{VS}^{(0)}$ in equation (2.48) is associated with source positions $\mathbf{x}_s$, where $s = 1, ..., S$ and one grid block position $\mathbf{x}_n$, where $n = 1, ..., N$.

The formulas in Equations (2.47) and (2.48) are referred to as the Dyson equations for

the Lippmann-Schwinger equation for the source-receiver and source-volume Green functions respectively (see Jakobsen and Ursin, 2015). The Dyson equations above physically imply that there exists a connection between the Green's function for the background medium and actual (heterogeneous) medium through a multiple scattering process. From Equation (2.48), it follows that the source-volume Green's function $\mathbf{G}_{VS}$ for the heterogeneous media is computed by matrix inversion as

$$\mathbf{G}_{VS} = (\mathbf{I} - \mathbf{V}\bar{\mathbf{G}}_{VV}^{(0)})^{-1}\mathbf{G}_{VS}^{(0)}. \tag{2.49}$$

Using the above equation (2.49) in conjunction with the Dyson equation (2.47) we calculate the source-receiver Green's function (for the heterogeneous background media) used to calculate the waveform data in frequency domain.

For multiple sources and frequencies, the implementation of the distorted-Born is similar to that of the Born approximation. We begin by writing the scattered wavefield data which is the difference between the total wavefield at the receiver in the actual medium and in the background model, given by

$$\mathbf{d} \equiv (\mathbf{G}_{RS} - \mathbf{G}_{RS}^{(0)})\tilde{\mathbf{f}} = \mathbf{G}_{RV}^{(0)}\mathbf{V}\mathbf{G}_{VS}\tilde{\mathbf{f}}, \tag{2.50}$$

where the S-dimensional vector $\tilde{\mathbf{f}}$ contains all information about the seismic source distribution. We can then write the expression for the scattered wavefield in component form as

$$\tilde{d}_{r,s}(\omega) = \sum_{n=1}^{N} J_{rn,s}(\omega)m_n, \tag{2.51}$$

where

$$J_{rn,s}(\omega) = \left[\bar{G}_{rn}(\omega)\delta v_n G_{ns}(\omega)\right]\bar{f}_s, \tag{2.52}$$

and

$$m_n = (c_n)^{-2} - (c_n^{(0)})^{-2}. \tag{2.53}$$

Here, $c_n$ and $c_n^{(0)}$ is the estimated wave-speed in grid block $n$ for the actual medium and reference medium respectively.

By considering discrete frequency values $w_w$ $(w = 1, ..., W)$, then Equation (2.51) becomes

$$\tilde{d}_{r,sw} = \sum_{n=1}^{N} J_{rn,sw} m_n, \tag{2.54}$$

where

$$\tilde{d}_{r,sw} = \tilde{d}_{r,s}(\omega_w), \tag{2.55}$$

and

$$J_{rn,sw} = J_{rn,s}(\omega_w). \tag{2.56}$$

Equation (2.54) gives a linear relation between the model parameter and the scattered wavefield. We can now reduce the three indices $r, s, w$ to one index $j$;

$$r, s, w \rightarrow j, \qquad j = 1, ...H = S \times R \times W, \tag{2.57}$$

and then Equation (2.54) can be written in abbreviated notation with the new index $j$ such that:

$$d_j = \sum_{n=1}^{N} J_{jn} m_n \tag{2.58}$$

or in matrix notation as

$$\mathbf{d} = \mathbf{Jm}. \tag{2.59}$$

The data vector $\mathbf{d}$ contains all the different frequency components of the scattered wavefield for all sources and all receivers. Equation (2.59) is the standard form of representing the linear relationship between the forward and inverse modelling problem.

## 2.6   Numerical examples and discussions

In this section, we examine the ability of approximate solutions based on scattering theory for forward modelling of time-lapse data. For this purpose, we use three synthetic velocity models that mimic time-lapse scenarios.

### 2.6.1 Simple gas reservoir models

We consider a synthetic test study for two simple velocity models that mimic a gas reservoir. The models are similar to the model considered by Abubakar et al. (2003) except that for the first model, hereafter called model 1, different velocity values have been considered. The models are 2D velocity models for a constant density acoustic wave equation modelling presented in Equation (2.3). These models illustrate what kinds of time-lapse velocity changes might occur in a very simple reservoir due to reservoir management actions.

Model 1 is a small velocity contrast model shown in Figure 2.3 and essentially consists of two-sandstone layers bounded above and below by a shale layer. The model 1 velocities are loosely based on the geological structure encountered in the North Viking Graben (sand-rich clastics) whereby the P-wave velocity values show small contrast between sandstones and shales (Bouma et al., 2000). The velocity in model 1 varies from 2950 $m/s$ to 3150 $m/s$, so the contrasts are small. This kind of model is valid for Born approximation modelling with homogeneous background medium.

The second velocity model, hereafter called Model 2 is shown in Figure 2.8 and has velocity contrasts that are much larger than in model 1. Model 2 consists of a top water layer and the velocities are exactly the same as the ones considered in Abubakar et al. (2003). This model cannot be well modelled using Born approximation with homogeneous background model. We can achieve better results by considering an inhomogeneous background velocity model by making use of the distorted Born approximation. Figures 2.3 and 2.8 illustrate the time-lapse experiment study in which we monitor the movement of fluids in a reservoir demonstrated by variations in the velocity distributions. The baseline 2D velocity models are shown in Figures 2.3(a) and 2.8(a). The monitor velocity models which represent time-lapse velocity are shown in Figures 2.3(b) and 2.8(b). The models for the monitor surveys only change the properties of the third layer; c=3077 becomes c= 3150 for Model 1 and c=2500 becomes c= 2700) for Model 2 as summarised in Table 2.1.

Table 2.1: P-wave velocity change scenarios between monitor and baseline surveys within the reservoirs corresponding to model 1 and 2

| Model scenarios | $V_P$ change in third layer (m/s) | % $V_P$ change in third layer | Maximum $V_P$ model contrast (m/s) |
|:---:|:---:|:---:|:---:|
| Model 1 | 73 | 2% | 200 |
| Model 2 | 200 | 8% | 1500 |

The time-lapse changes in velocity which represents the differences between each of the two model surveys (baseline and monitor) for Models 1 and 2 are shown in Figures 2.3(c) and 2.8(c). The models are defined on a 2-dimensional grid with 80 points in y-direction and 20 points in z-direction and a square grid size of 15 m by 15 m. Thus, each of the resulting models has 1.2 km in lateral direction and 0.3 km deep.

In order to generate synthetic data with the velocity models, we assume the same source signature in all numerical examples; a Ricker wavelet (Ricker, 1953) with central frequency of 7.5 Hz. The analytical form of this wavelet is defined as:

$$h(t) = [1 - 2\pi^2 f_c^2 t^2] exp(-\pi^2 f_c^2 t^2) \tag{2.60}$$

where $f_c$ is the central frequency. The Ricker wavelet is satisfactory in processing seismic data since it leads to a better approximation of the seismic spectra than other families of approximating functions. This wavelet and its amplitude spectrum are shown in Figure 2.2.
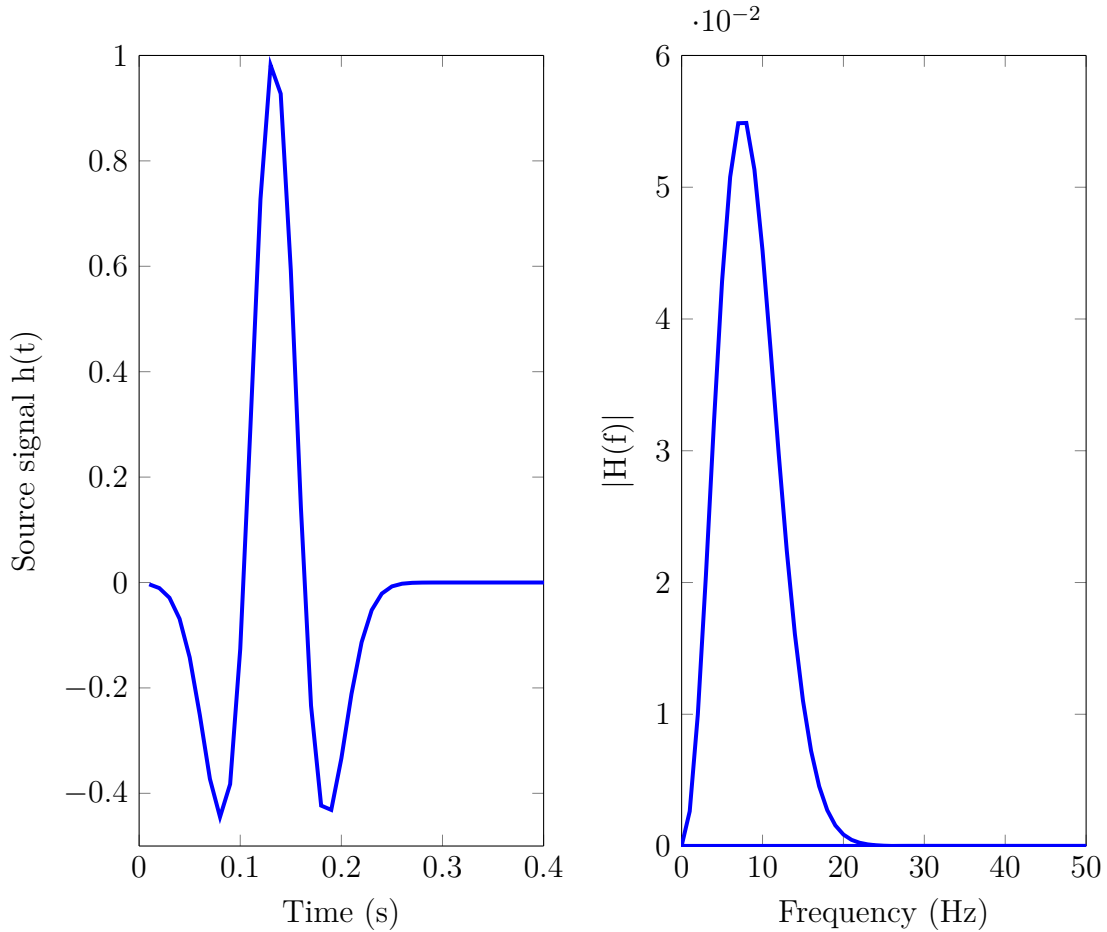
Figure 2.2: Left Panel: a Ricker wavelet presented in equation (2.60) but with a time shift $t_0 = 1/f_c$ to show the causal nature of this function. Right Panel: the frequency spectrum of the source signature used in the computations for the baseline and monitor datasets.

For each data set of Model 1 and 2, there are 30 source positions at equidistant horizontal distances with 50 receivers also at equidistant horizontal distance positions. The sources and receivers are placed at the top of the model and cover the entire survey line.

For model 1, the synthetic data sets for the baseline and monitor survey are modelled with 2D frequency domain acoustic wave equation using the Born approximation with a simple homogeneous background model ($c$=3000) shown in Figure 2.4. Figure 2.5 shows the noise free synthetic seismograms for the two surveys corresponding to model 1. The resulting seismograms obtained after adding some random Gaussian based noise band-limited in the bandwidth of the source wavelet are shown in Figure 2.6. The noise has been added to the noise-free data with a signal to noise ratio (SNR) of 6 dB. The noise greatly distorts

the seismograms for both the monitor and baseline model. For each figure, the synthetic seismograms have been normalized with respect to the maximum amplitude of the baseline seismograms. We notice that in both figures, it is impossible to observe any change in waveforms for the monitor and baseline survey by visual inspection.

In order to demonstrate the time-lapse problem in differential approach, the difference of the two survey data-sets is obtained resulting into time-lapse seismograms shown in the bottom panel of Figure 2.5. It is important to note that the amplitude of time-lapse seismograms is amplified by a factor of 5 after normalisation in order to plot the seismograms at the same scale as as the baseline seismograms and visualise the time-lapse signals which are weak. Very low energy time-lapse signals may complicate the recovery of time-lapse structural changes during inversion. Since we assume the two surveys have the same acquisition geometry and conditions and that overburden remains unchanged, earlier events above the reservoir cancel in the time-lapse waveform data. In addition, this implies repeatability as we can only associate the differences in the acquired data with time-lapse effects.

Figure 2.7 shows a comparison of the predictions of the Born approximation and distorted-Born approximation with the exact T-matrix solution corresponding to model 1. The same amplitude normalization factor is applied while generating the seismograms in Figure 2.7 so that we can be able to compare the amplitudes directly. We can see that the Born approximation gives good predictions for the time-lapse time-shifts and amplitudes for this small velocity and volume contrast model. The distorted-Born approximation gives very accurate predictions similar to those of the exact T-matrix.

The time-lapse synthetic data for model 2 were generated by considering the baseline model as the reference (background) medium and the monitor model as perturbed medium (see Zhang, 2006a) such that the scattered field is directly connected to the difference data (time-lapse data). For this case the difference model correspond to the perturbation. We work in the frequency domain and use the distorted-Born approximation utilising the baseline model (Figure 2.8 a) as the heterogeneous background medium . To understand how well the distorted-Born performs for forward modelling of time-lapse data effects involving models characterised by large velocity contrasts, we compute the wavefield for one shot and 50

receivers at a specified single frequency before extending it to all frequencies and compare the results with the exact solution based on the T-matrix (Jakobsen, 2012). As shown in Figures 2.9 and 2.10, the distorted Born approximation is a very good approximation if the reference model (the baseline model) is close to the actual medium (the monitor model). Note that the only difference between the baseline and monitor models is the time-lapse velocity change in the third layer.

Figure 2.12 shows the comparison of the time-lapse seismograms obtained using the Born approximation, distorted Born and the exact solution based on the T-matrix approach. The results shown correspond to 20 receiver positions, a single shot and reservoir region thickness of 120 m at depths of 150 m. The results show that the predictions of the distorted-Born approximation and the exact T-matrix perfectly match. As expected, the Born approximation gives wrong predictions of the travel times and amplitudes. Note that the seismograms corresponding to the Born approximation were computed using a homogeneous background model with the properties of the first layer. This numerical example shows that the scattered wavefield patterns are generated with significant errors for relatively higher-contrast scatterers. As discussed by Jakobsen (2012), the velocity contrasts need to be moderate or small for the Born approximation to give sufficiently accurate results in time-lapse seismics. The distorted-Born performs perfectly well since it considers the true heterogeneous background model, giving rise to correct travel times and amplitudes.

Figure 2.11 shows the noise free and noisy time domain synthetic waveforms for the difference data between monitor model and baseline model (time-lapse data) for model 2 corresponding to a shot in the middle of the model. The amplitudes of the seismograms are visualised without being amplified since the time-lapse velocity variation is big enough. The noise effect in the time domain that results when a SNR of 6 dB is added is evidenced by a significant distortion in the waveforms. The upper boundary of the computational grid creates some weak reflections seen on the sides of upper parts of the seismograms.

### 2.6.2   Model for monitoring $CO_2$ injection process

We consider a simple 2D example of a reservoir model hereafter called Model 3 designed to simulate $CO_2$ injection process using one injector. We assume there is a $CO_2$ injector at a given depth in the middle of the model whose dimensions are given in Table 2.2 and a source-receiver geometry at the surface above the reservoir. In this particular example, our injection point is at a depth of 500 m about 100 m below the reservoir top. This model may not be especially realistic, at least in terms of the depth of the reservoir; but just as an example of the $CO_2$ sequestration aspect. The baseline case corresponds to a model before $CO_2$ injection (top panel of Figure 2.13) and the monitor case (middle panel of Figure 2.13) after two years of injection. We simulate the injection by a decrease in velocity values of the baseline model using a Gaussian model that simulates the injection of a fluid into a permeable reservoir layer. We obtain a reasonable picture of likely $CO_2$ distributions in the reservoir layer. The velocity decreases up to about 5% within the reservoir region (layer 3). The velocity difference between the monitor and baseline (time-lapse model) are shown in the lower panel of Figure 2.13.

Table 2.2: Modelling parameters for Model 3.

| Model size | Grid size (m) | Sample rate | Source wavelet | Record length |
|---|---|---|---|---|
| $x \times z = 100 \times 40$ | $dz = 24$ $dx = 24$ | 0.01 s | Richer wavelet | 2 s |

The synthetic seismic dataset for the surface seismic monitoring were generated using an acoustic distorted-Born approximation earlier used for Model 2 taking the baseline model (upper panel of Figure 2.13) as the heterogeneous background. The modelling parameters are shown in Table 2.2. Our interest is to model the time-lapse seismograms corresponding to the difference structure accruing in the Earth volume due to injection of $CO_2$ and later reconstruct it within a non-linear inversion approach. We employed 25 sources and 100 receivers equally spaced at the surface along the lateral direction from $x = 0$ m to $x = 2400$ m. We consider the entire survey line for the distribution of all the sources. Shown in Figure 2.13 is a common

shot gather for the difference data (time-lapse data) due to the changes resulting from $CO_2$ injection. The injection effects can be predicted in the difference sections. The effects of random noise on the seismograms are clearly manifested in the lower panel of Figure 2.13. The seismograms would not be visible at all with more noise added.

In Figure 2.15, we have compared the time-lapse seismograms calculated using the Born approximation, distorted-Born and exact T-matrix. Important differences exist especially with the predictions of the Born approximation. The $CO_2$ injection model difference seismograms obtained using the Born approximation are inaccurate and the $CO_2$ effects on the velocity field is not well distinguished. This demonstrates yet another inadequacy of the Born approximation in distinguishing seismically the effects of $CO_2$ injection on the seismic velocity field within the reservoir volume. Wrong predictions of the time-lapse time-shifts and amplitudes by the Born approximation are expected for reservoirs with large contrast volumes (Ikelle and Amundsen, 2005). Note that the spatial extension of the perturbation in Model 3 is large and the reservoir thickness is big. The distorted-Born approximation still performs very well in predicting the time-lapse seismograms even when the thickness and depth of the reservoir increases. The reflectivity due to the injection process is well imaged on the seismic data. Clearly, one sees that the distorted-Born approximation and exact T-matrix give pretty similar results. In the real world, the reservoir is usually thin and therefore the distorted-Born approximation can be applicable for time-lapse seismics provided the reference model is close to the monitor model.

## 2.7 Concluding remarks

In this Chapter, we discussed the forward seismic modelling process based on the fist-order scattering theory. First, we discussed the concept of forward modelling and introduced the Helmholtz form of the acoustic wave equation for a constant density earth model with variable velocity. We then explained the relevance of Green's function and discussed the implication of the reciprocity theorem as applied to the Green's function. We also derived the important formulas for Born scattering and discussed how the Born approximation integral equation is formulated. The validity of the Born approximation and Implementation of the Born integral by discretization were also discussed. A discussion of the distorted-Born approximation which

extends the validity range of the traditional Born approximation is also given a detailed treatment.

We implemented numerical modelling using Born approximation and distorted-Born approximation. We effectively modelled time-lapse waveforms by assuming only velocity is changed during the time-lapse acquisition and benchmarked our results against an exact T-matrix solution. We show that with these methods in time-lapse seismics, we can easily visualise changes in waveforms between monitor survey and baseline survey by the data difference to detect variations in seismic velocities. The distorted Born performs impressively well for models with large velocity and volume contrasts thus improving the validity range of traditional Born approximation. The distorted-Born also demonstrates sufficient accuracy in elucidating the $CO_2$ injection effects on the seismic velocities, at least for the injection model considered.

In this chapter, only numerical experiments based on 2D acoustic wave equation for constant density modelling are discussed. However, the algorithm can easily be modified for 3D modelling. Similarly, a formulation for an elastic isotropic and/ or elastic anisotropic case (Appendix B) is a straight forward approach. Changes in other parameters other than velocity alone and rock physics relations need to be incorporated in the modelling to make it more realistic.
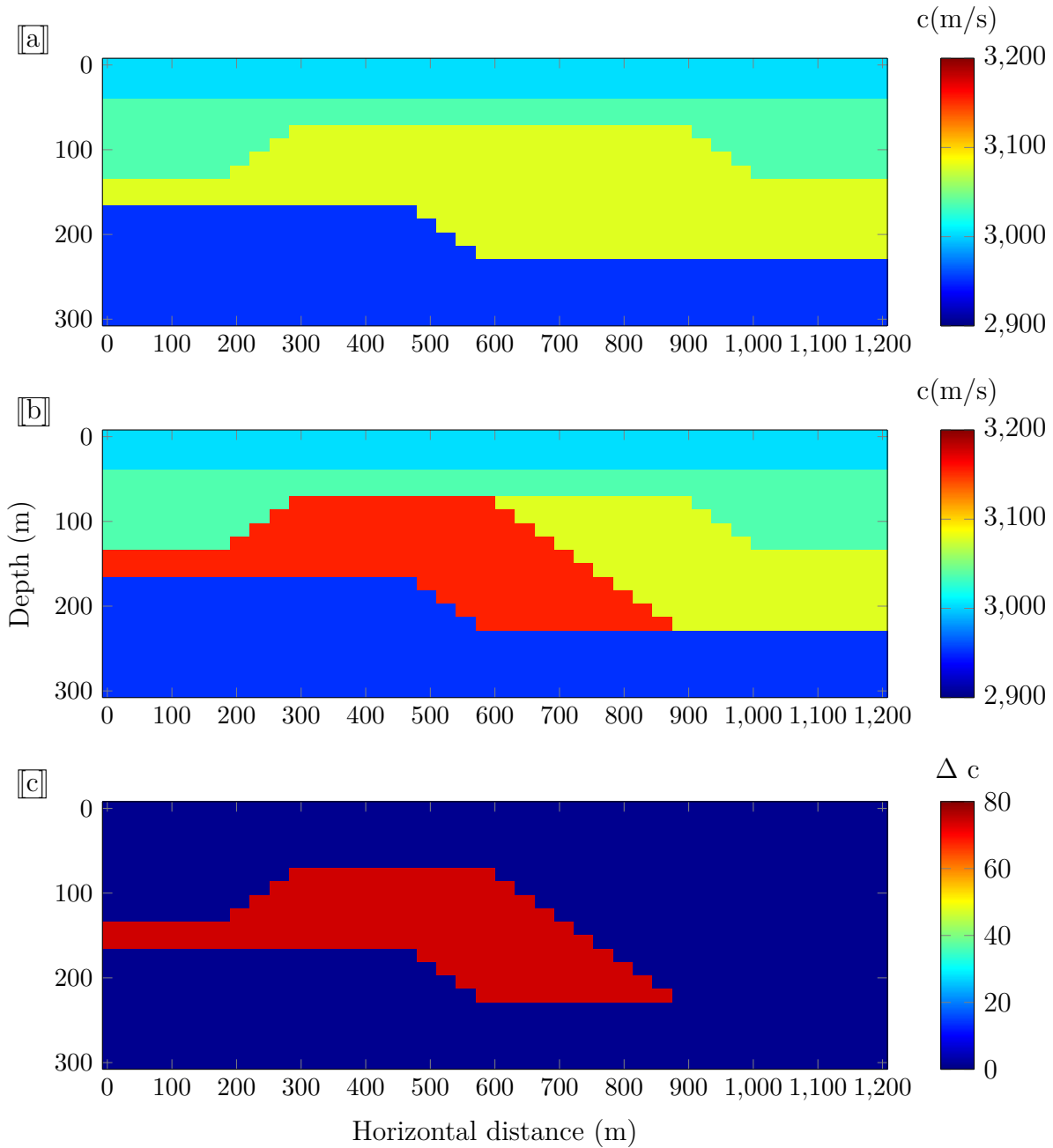
Figure 2.3: The 2D velocity models used in this study, from Abubakar et al. (2003) associated with Model 1: (a) the baseline velocity model; (b) the monitor velocity model; (c) baseline-monitor model difference.
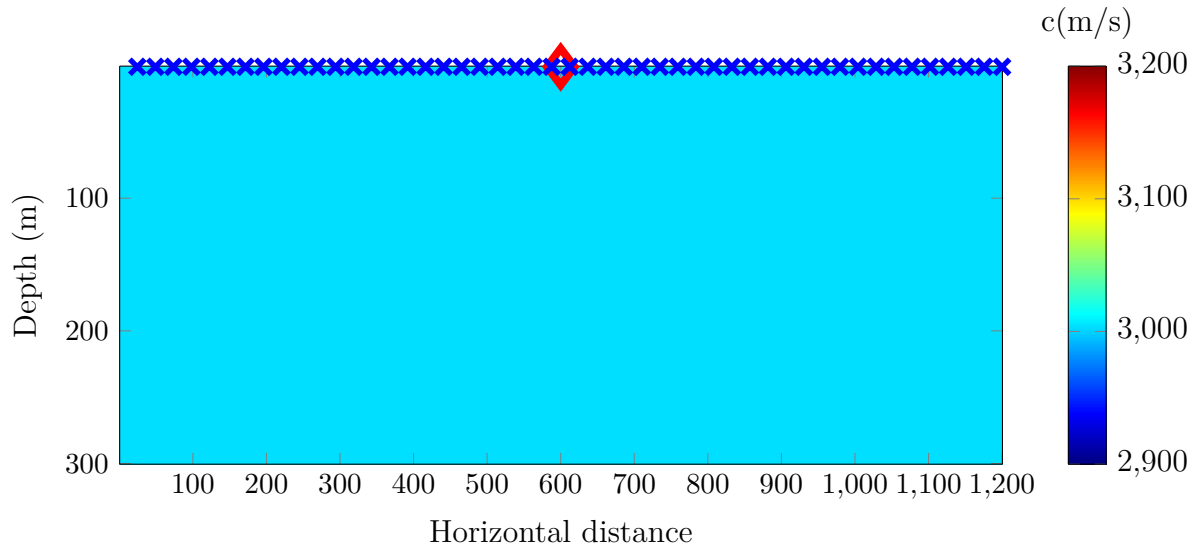
Figure 2.4: The constant background velocity model used for modelling the baseline and monitoring models corresponding to Model 1. Also shown is a source located at the top center of the model (red mark) and a distribution of the receivers (blue marks).
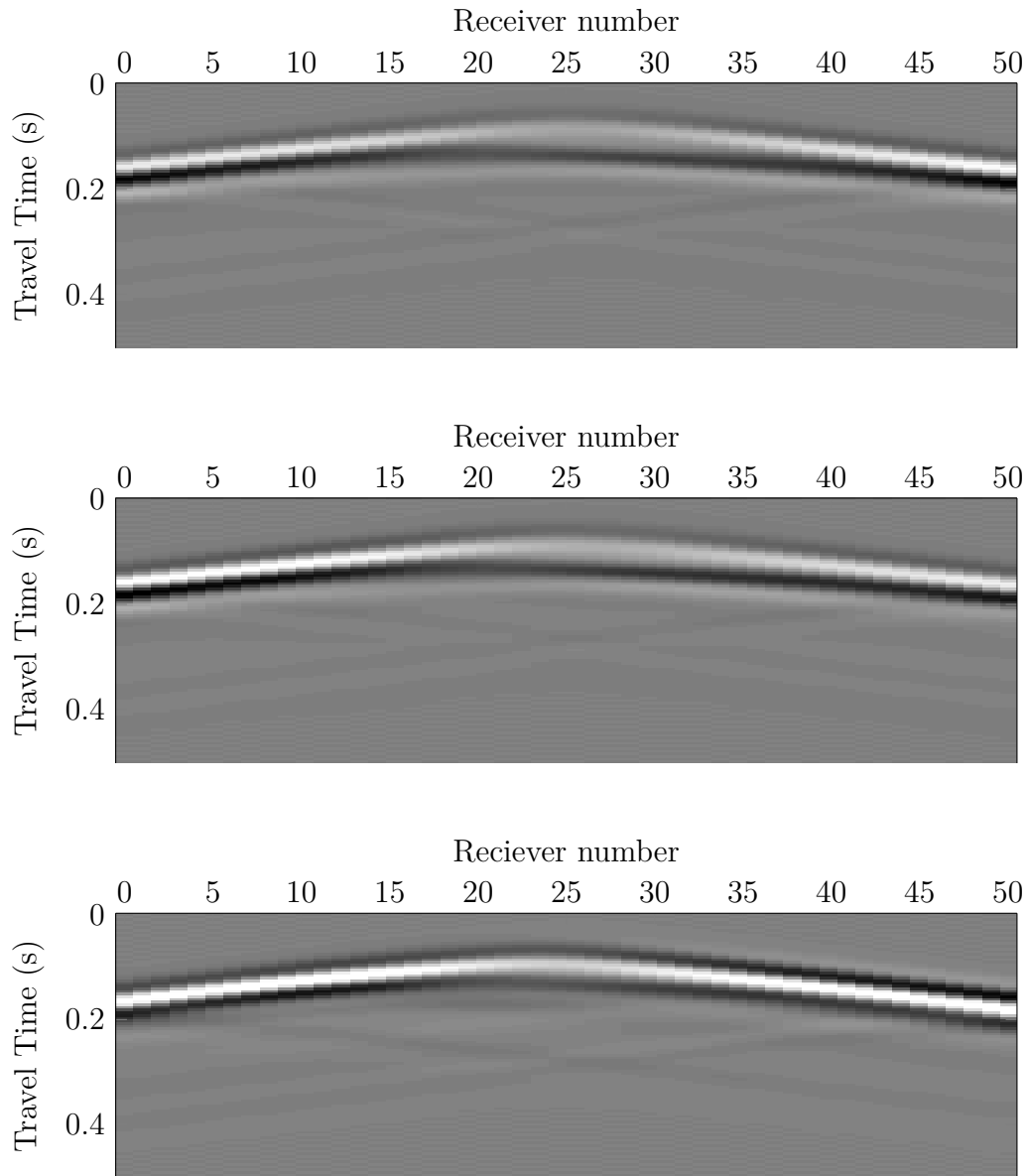
Figure 2.5: Noise-free synthetic seismograms corresponding to baseline and monitoring models in Figure 2.3 for a source located at the top center of the model. Top Panel: the noise-free seismograms of the baseline survey. Middle Panel: the noise-free seismograms of the monitor survey. Bottom Panel: the noise-free difference data between the monitor survey and baseline survey data sets. For time-lapse changes to be visible, the amplitudes of the seismograms in the bottom panel are amplified by a factor of 5.
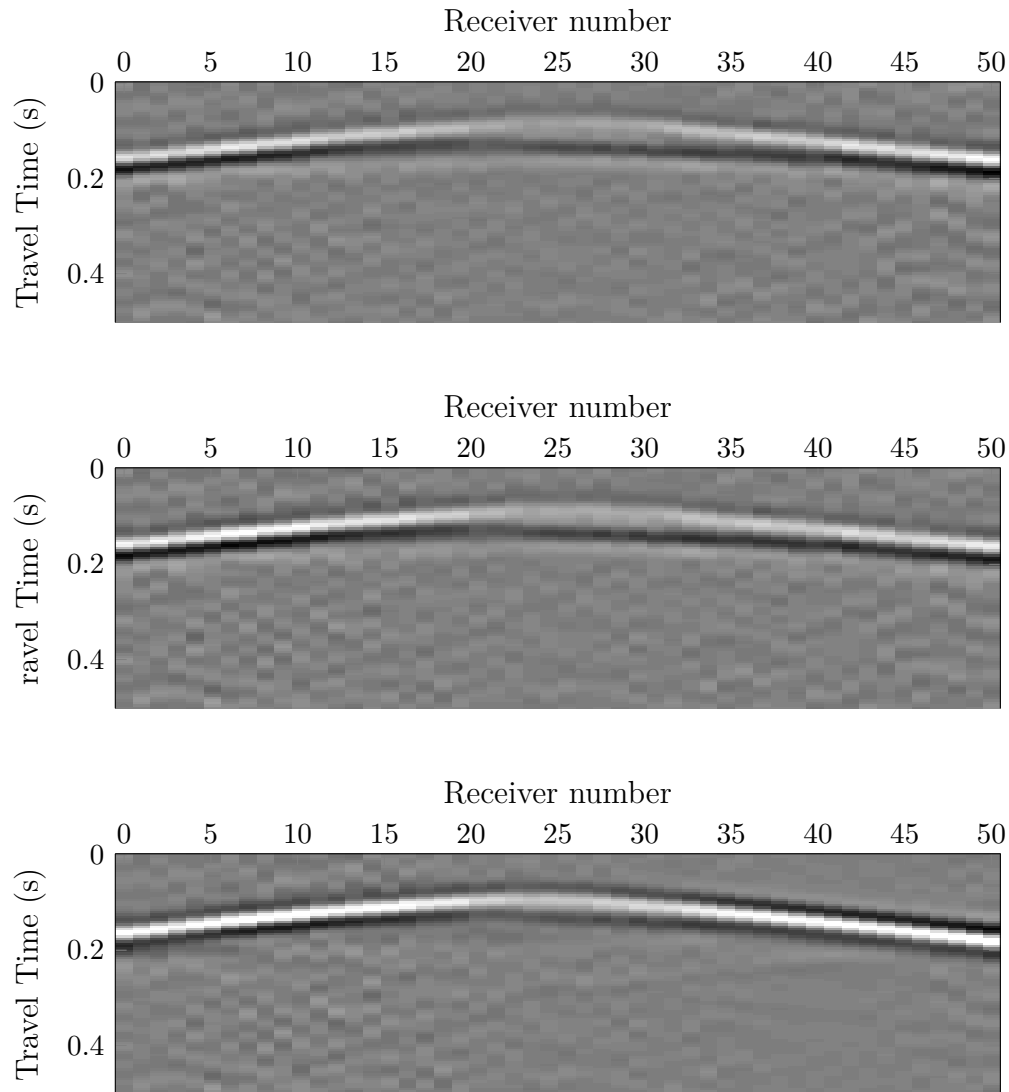
Figure 2.6: Noisy synthetic seismograms corresponding to baseline and monitoring models in Figure 2.8 for a source located at the top center of the model. The coloured Gaussian noise has been added to the noise-free data with SNR=6 dB; Top Panel: the noisy seismograms of the baseline survey. Middle Panel: the noisy seismograms of the monitor survey. Bottom Panel: the noisy difference data between the monitor survey and baseline survey data sets.It is important to note that the amplitude of the seismograms in the bottom panel are amplified by a factor 5 for visualization purposes.
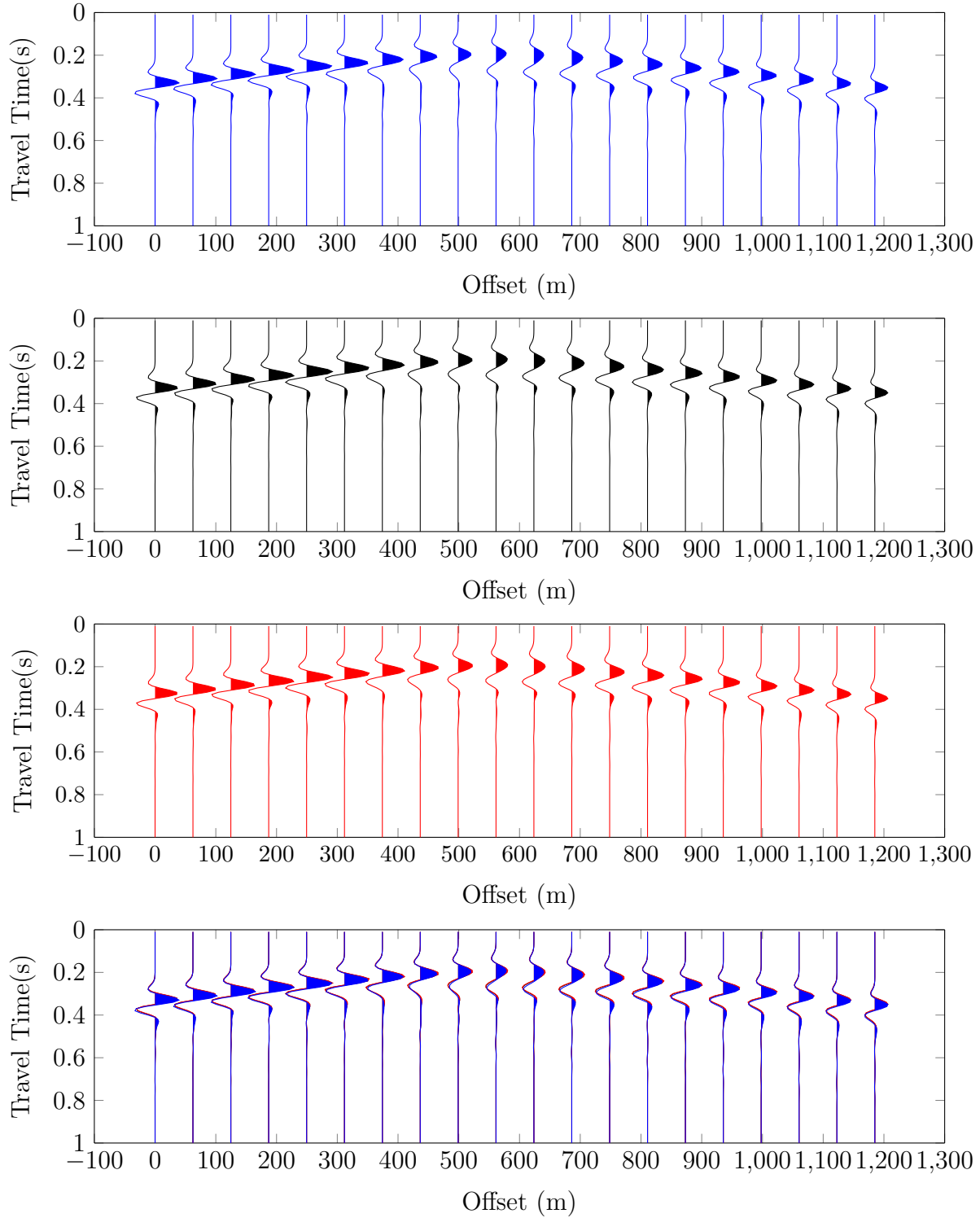
Figure 2.7: Comparison of time-lapse seismograms for model 1 in Figure 2.3(c) as predicted by the Born approximation (blue), distorted Born (black) and exact T-matrix solution (red). The lower figure shows all the three predictions superimposed. The same amplitude normalization factor is applied to the seismograms.
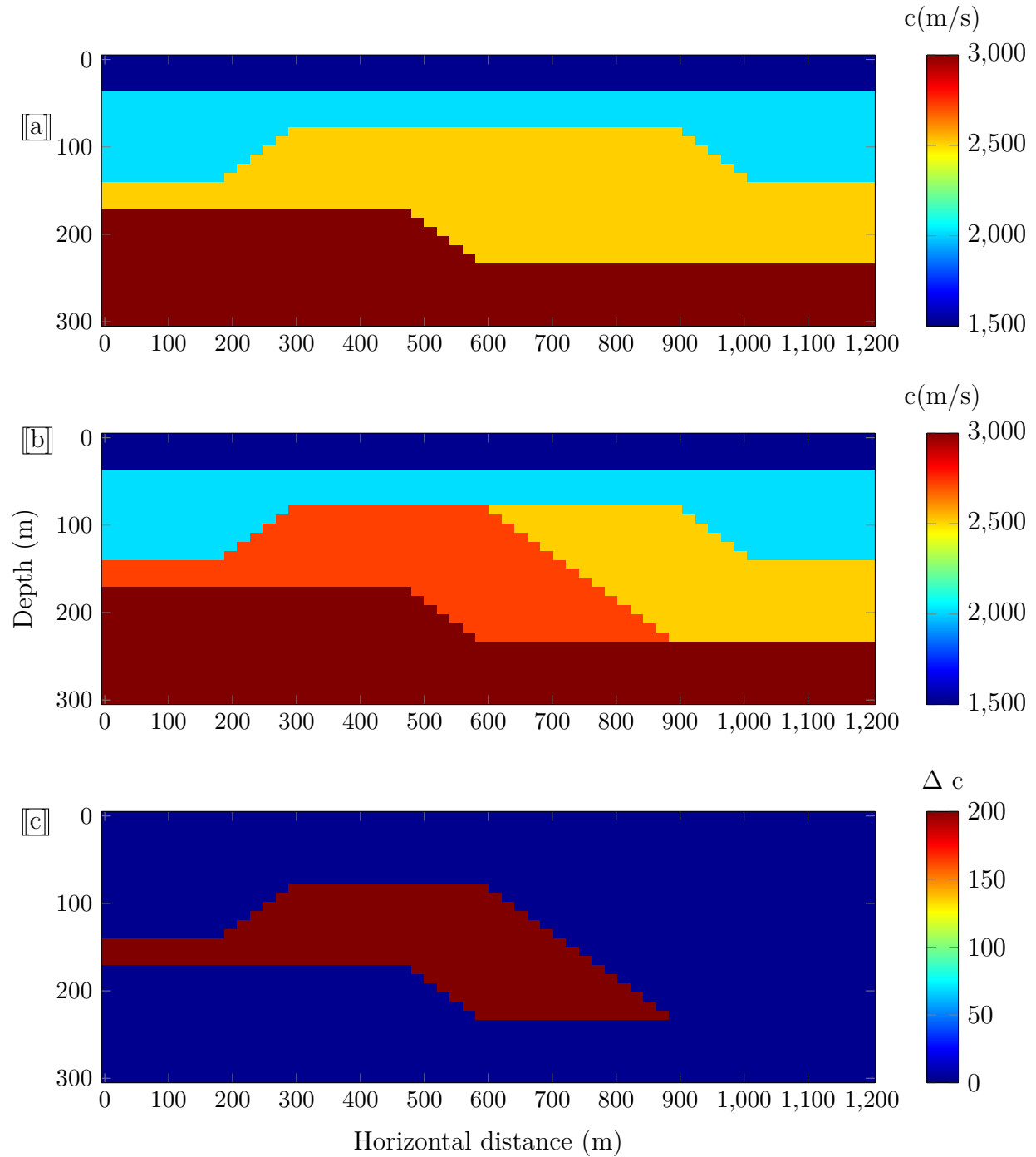
Figure 2.8: Velocity model with large contrasts used in this study, from Abubakar et al. (2003) associated with Model 2: (a) the baseline velocity model; (b) the monitor velocity model; (c) baseline-monitor model difference.
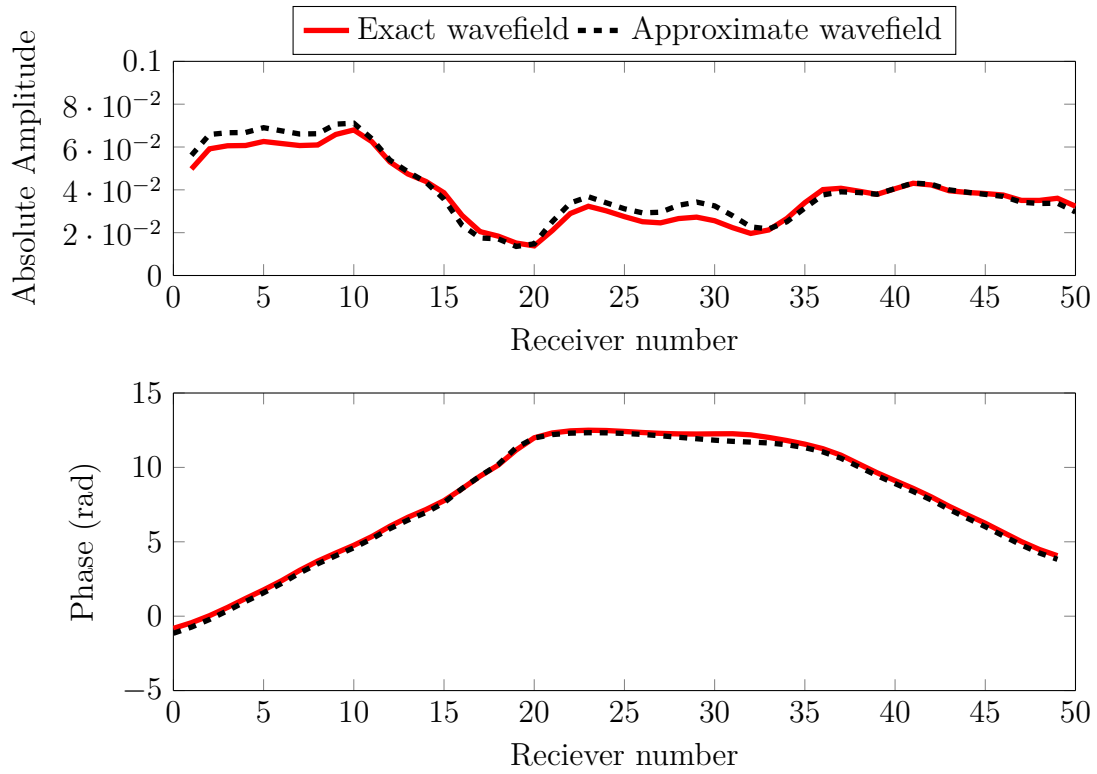
Figure 2.9: Comparing computed frequency domain wavefield amplitudes (upper panel) and phase (lower panel) for the time-lapse model in 2.8(c) using exact field Greens function (red) and an approximation based on distorted Born (black). This corresponds to one frequency (10 Hz) and a single shot in the middle of model.
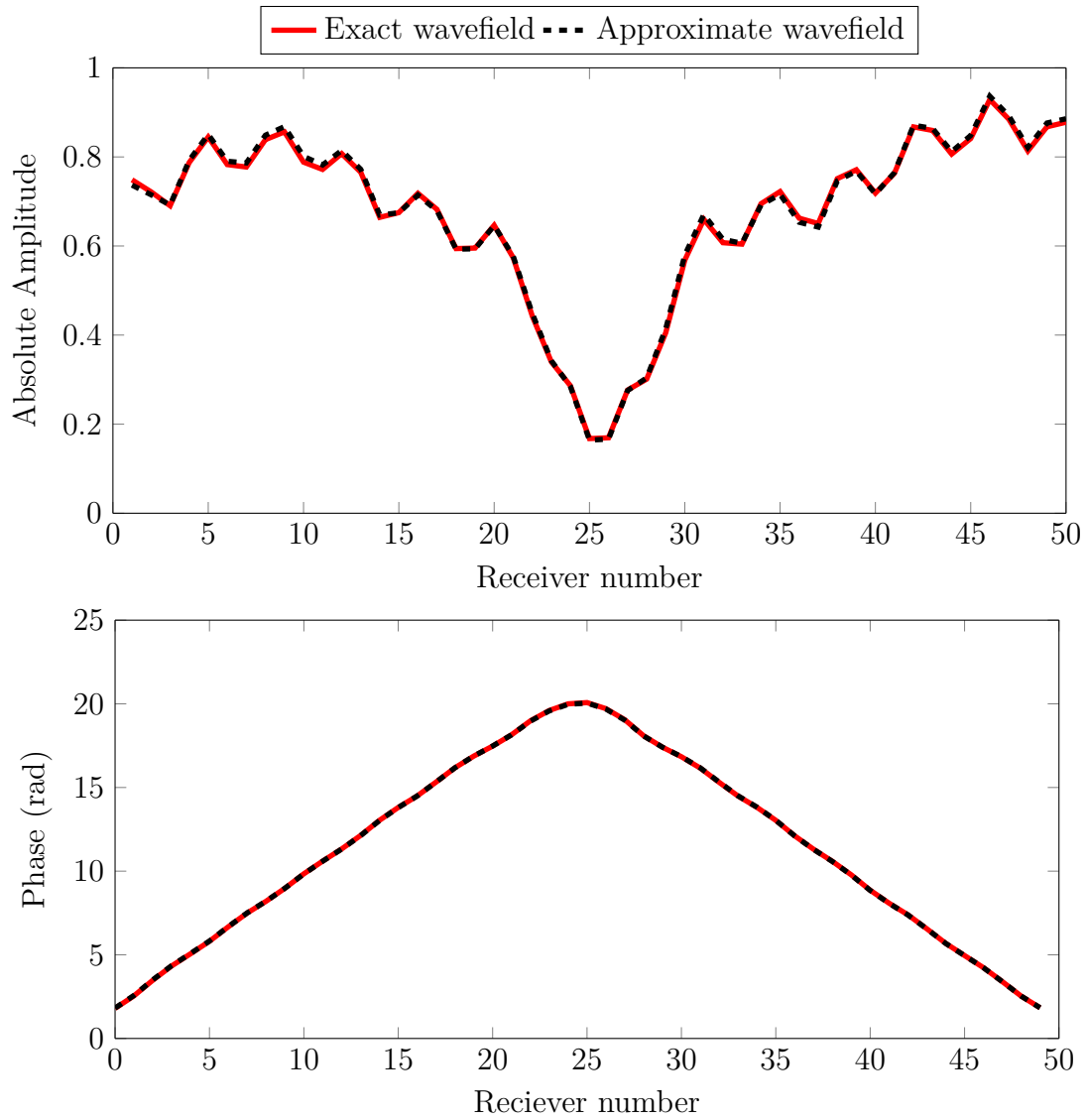
Figure 2.10: A comparison of the computed frequency domain wavefield amplitudes (upper panel) and phase (lower panel) for the monitor model in 2.8(b) using exact field Greens function (red) and an approximation based on distorted Born (black). This corresponds to one frequency (10 Hz) and a single shot in the middle of model.
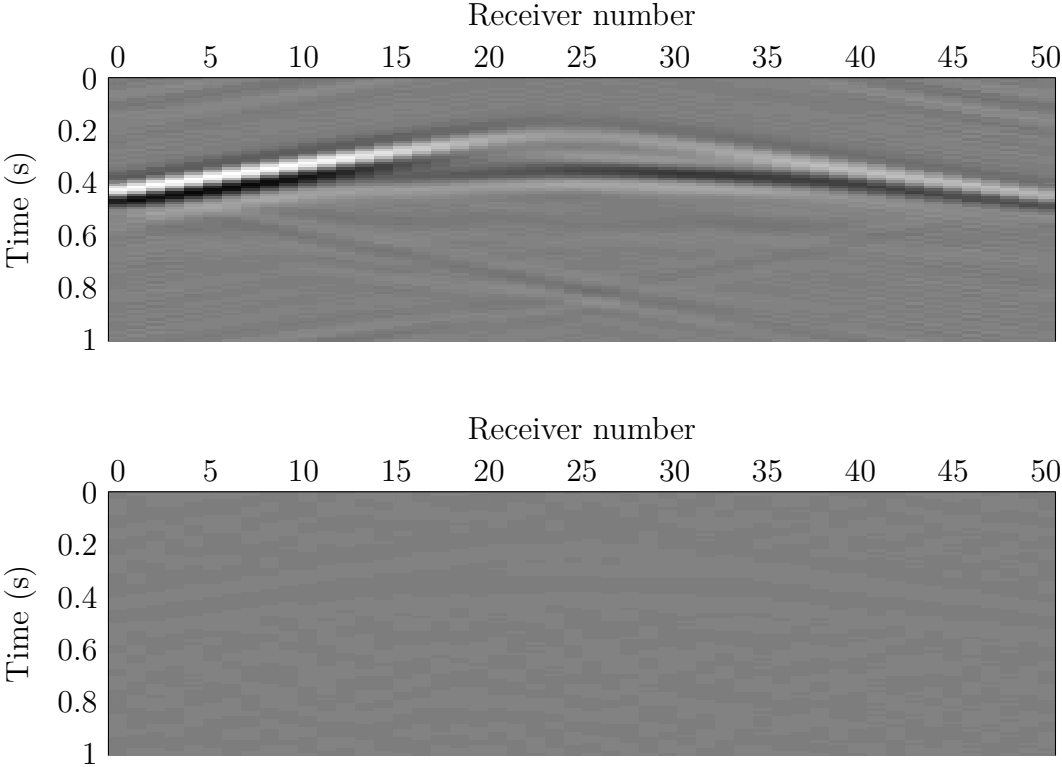
Figure 2.11: Time domain synthetic waveform data for the time-lapse velocity model in Figure 2.8(c) in the absence of noise (upper figure) and in the presence of noise (lower figure). The displayed common shot gather is for for a source located at the top center of the model. For noisy data, random white noise has been added to the noise-free data with SNR =6 dB. The time-lapse seismic events are blinded due to the noise effects.
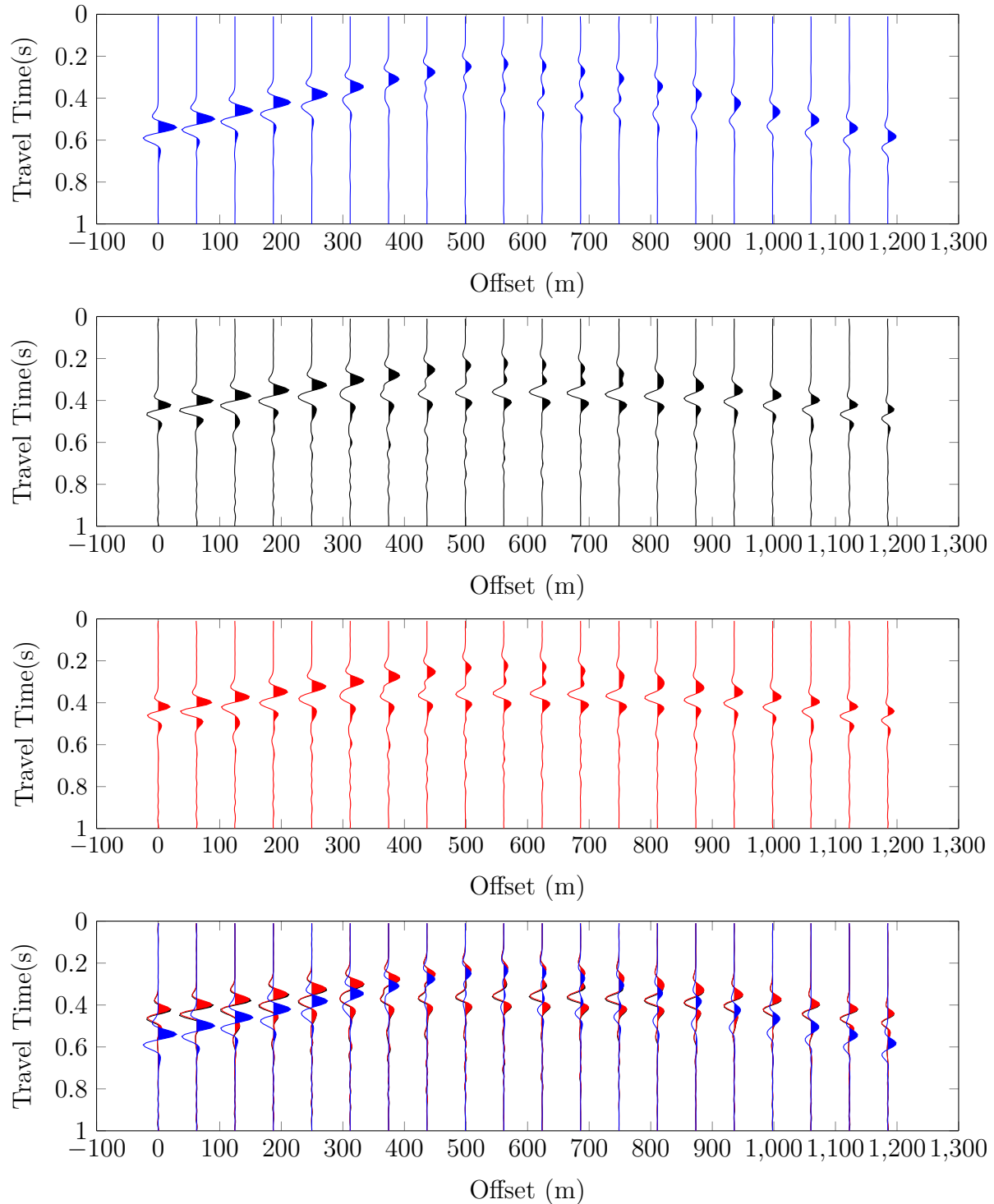
Figure 2.12: Comparison of time-lapse seismograms for model 2 in Figure 2.8(c) as predicted by the Born approximation (blue), distorted Born (black) and exact T-matrix solution (red). The lower figure shows all the three predictions superimposed. The same amplitude normalization factor is applied to the seismograms.
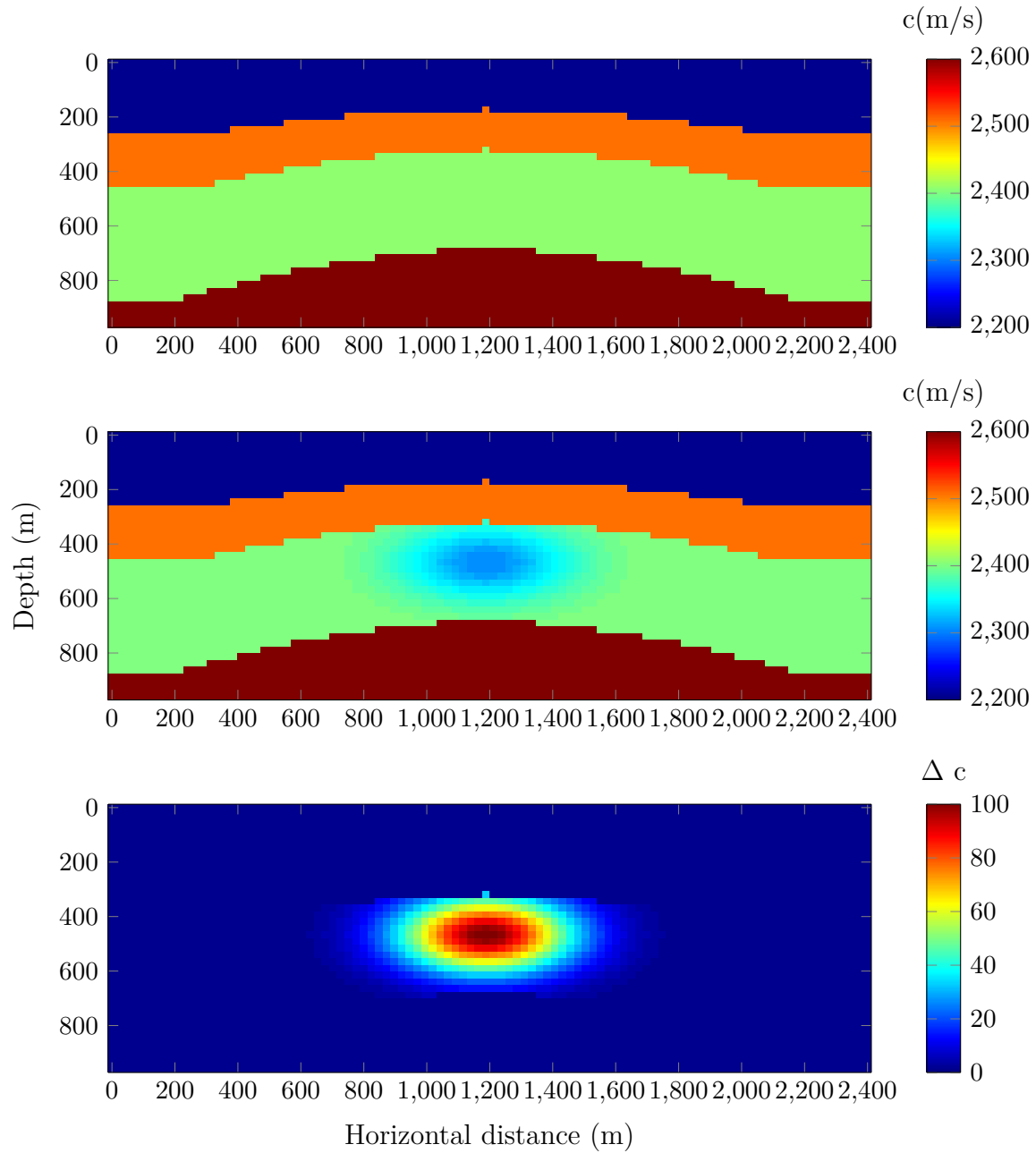
Figure 2.13: Time-lapse velocity models for $CO_2$ monitoring. Upper figure: baseline P-wave velocity model before injection. Middle figure: monitor P-wave velocity model after injection. Lower figure: time-lapse change of P-wave velocity (time-lapse model).
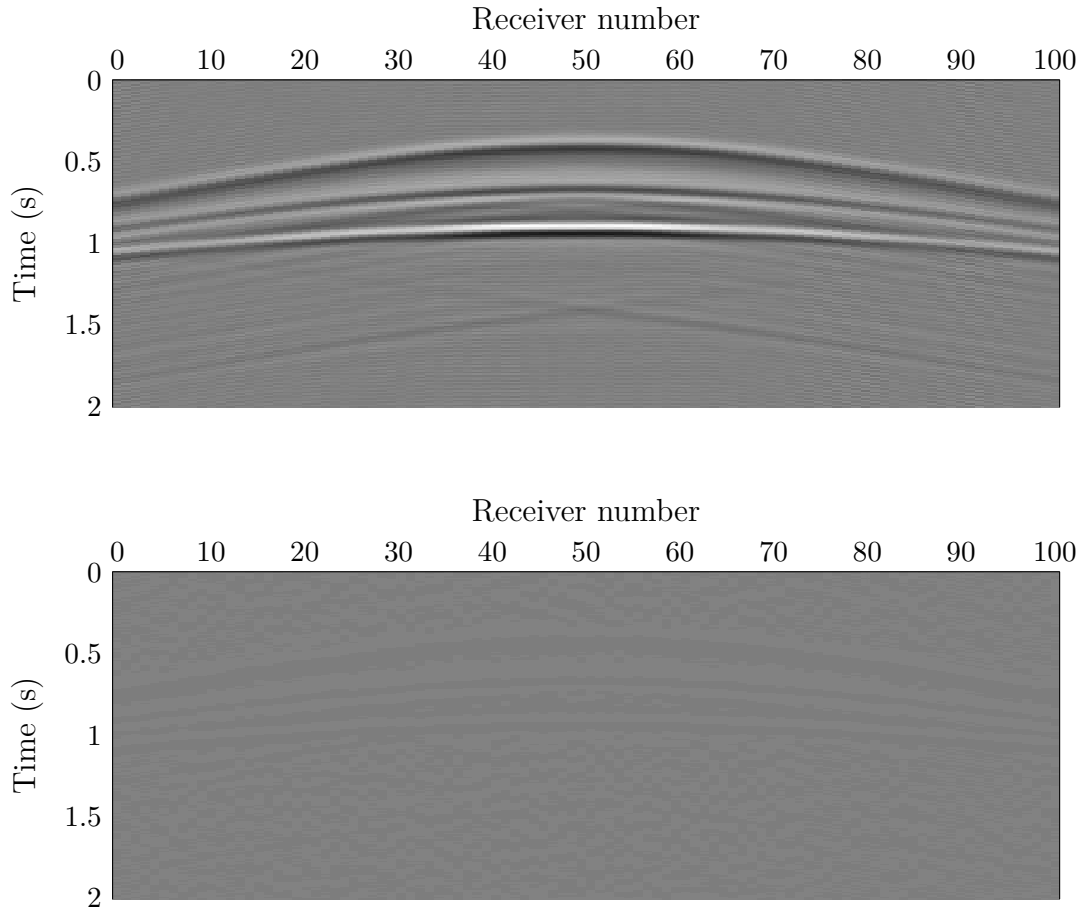
Figure 2.14: Time domain synthetic shot gathers of the scattered field corresponding to the difference data for base and monitoring models in Figure 2.13. Top panel: noise free seismograms. Bottom panel: noisy difference data (SNR = 6 dB), the time-lapse seismic events are blinded by a high level of random noise.
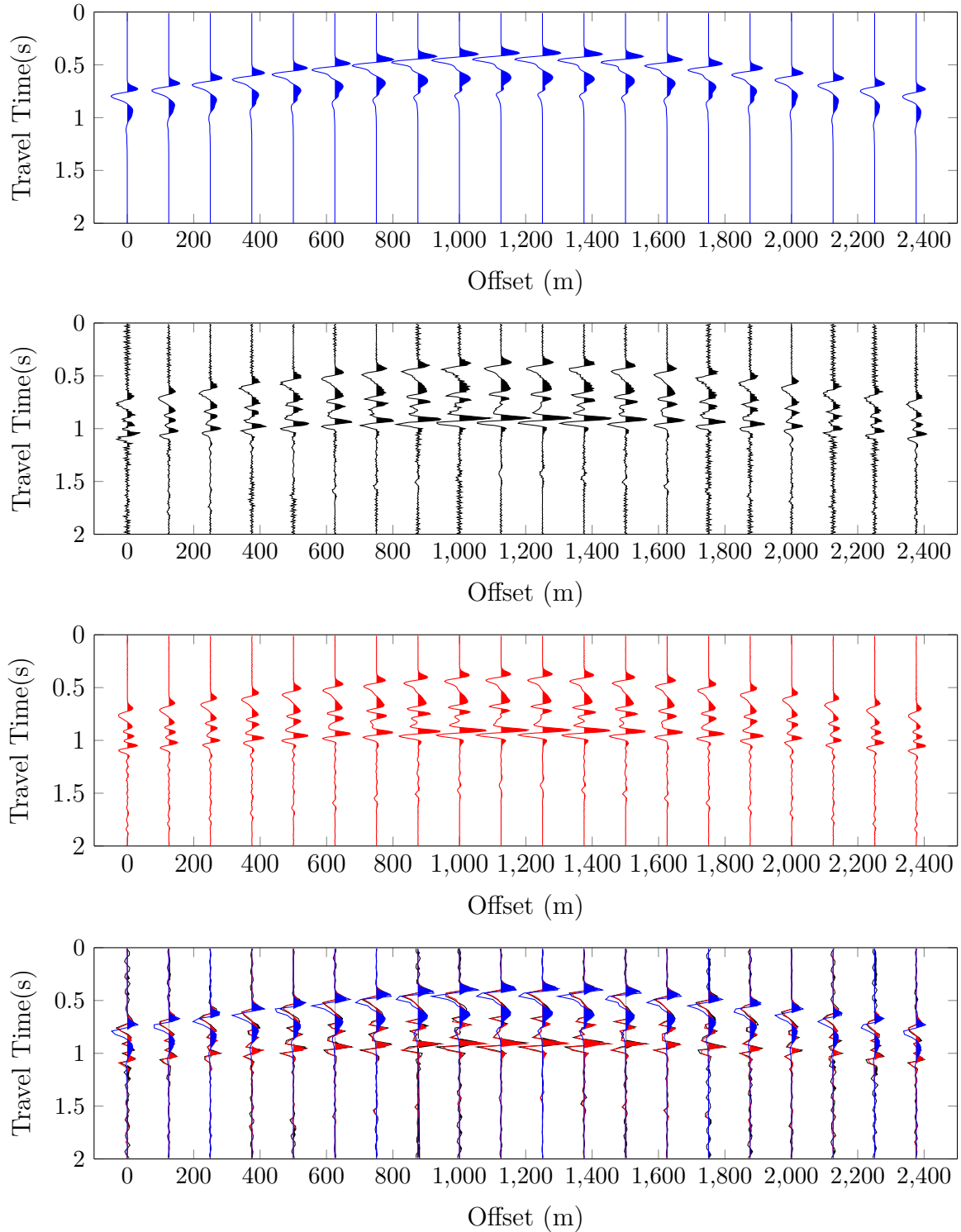
Figure 2.15: Comparison of time-lapse seismograms for model 3 in Figure 2.13(c) as predicted by the Born approximation (blue), distorted Born (black) and exact T-matrix solution (red). The lower figure shows all the three predictions superimposed. The same amplitude normalization factor is applied to the seismograms.

# Chapter 3

# Fundamentals of Inversion Theory

This chapter aims at introducing the basic concepts relevant to this subject, inversion. We discuss the details of ill-posed and well-posed problems. Our theoretical treatment from various sources in literature only focusses on the method of least squares used to solve inverse problems and Tikhonov regularization technique used to stabilise the solution. We present the fundamental equations that we will use in inversion and illustrate these points by implementing a toy example.

## 3.1 Ill-posed and well-posed problems

The notion of a well-posed problem is first presented in literature by Hadamard (1923). According to Hadamard, a problem is well-posed if it has a solution, the solution is unique, the solution depends continuously on data and parameters and is therefore stable. On the other hand, the problem is not well-posed in the sense of Hadamard (i.e., it is ill-posed) if the solution does not exist or is not unique or stable. Hadamard concluded that only problems that are motivated by real physical phenomena are well-posed. However, this conclusion is irrelevant today since the class of ill-posed problems include many classical mathematical problems and, most significantly, that such problems have important applications in science and engineering. Many methods have been developed to obtain approximate solutions to ill-posed problem and the solutions have a well-defined physical meaning.

For every field of science or engineering, it is imperative to define the forward problem characteristic of this field and then define the corresponding inverse problem. In such a case, the forward problem is well-posed while the inverse problem is ill-posed. This and the subsequent chapters will therefore investigate inverse problems equivalent to ill-posed problems. The relationship between inverse problems and forward problems which are ideally free of noise can be expressed as;

$$\mathbf{d} = \mathbf{Gm}$$
$$\mathbf{m} = \mathbf{G^{-1}d}$$

(3.1)

where $\mathbf{G}$ is the forward operator and $\mathbf{G^{-1}}$ is the corresponding inverse operator. The vectors, $\mathbf{d}$ and $\mathbf{m}$ denote the data and the solution (model parameters) to the inverse problem respectively. The inverse problem is described as linear if $\mathbf{G}$ is a linear operator or non-linear if $\mathbf{G}$ is a non-linear operator. It is often possible to linearize some non-linear inverse problems around some model by making some assumptions that involve neglecting higher order terms. From now on we treat $\mathbf{G}$ as a linear operator in order to apply simple methods involving linear inversion algorithms to solve the inverse problems.

For the sake of numerical evaluation, discretized versions of $\mathbf{m}$, $\mathbf{d}$ and $\mathbf{G}$ are used. All practical inverse scattering or imaging problems are by nature discrete since the data are measured by means of finite numbers of detectors (Bertero, 1992). The data are therefore known but model parameters are not known. The solution to the inversion problem is either even-determined, under-determined, over-determined or mixed-determined (Menke, 2012). An even-determined problem is one in which exactly enough data is available to determine the model parameters and the solution is unique. An under-determined problem is one in which insufficient data is available to determine all the model parameters, so the solution is non-unique. An over-determined problem is one in which more than enough data is available to determine the model parameters, so that there will be some inconsistency, or error, in the data. A mixed-determined problem is one in which more than enough data is available to constrain some model parameters and insufficient data is available to constrain other model parameters, so the problem has errors due to inconsistent measurements and model parameters

that cannot be determined from the data. Mixed-determined problems are common practical ill-posed problems.

The notion of stability is important in inversion. An inverse problem is said to be stable if its solution remains quantitatively the same, independent of small changes in the data. Since computational errors and noise are inherent in any inverse problem, the data is perturbed and the estimated solution will differ from the true solution. To test the stability of inverse problems, we can add noise that is sufficiently small to the data and then compute our solution. The computed solution will be far from the true solution if the problem is unstable. The sensitivity of the solution with respect to errors in the data can be studied by defining the relative magnitude of the input and output error to provide a measure of the stability. For a matrix inversion operation, the conditioned number of a kernel matrix defined by Wang (2003) as the ratio of the maximum eigenvalue to the minimum eigenvalue quantifies the sensitivity. Mathematically, if the forward modelling operator $\mathbf{G}$ is broader with a large condition number or the data kernel matrix $\mathbf{G}$ is singular, then the inverse problem is unstable (Golub and van Van Loan, 1996).

In a seismic exploration experiment, inversion starts with actual measured data and estimates the earth model properties. If the inversion is done perfectly, the earth model looks like the real earth. However, the real earth is a continuous distribution of these properties (Scales and Smith, 1994) while the data consists of finite observations hence there are no unique solutions. In addition the measured data include noise, losses and other inaccuracies and is therefore known to be unstable and usually needs to be stabilised. This stabilisation can be achieved by constraining the solution as we shall discuss in the subsequent sections.

## 3.2 Inversion of ill-posed problems

The inverse problems encountered in exploration seismic techniques are often ill-posed, because their solutions are either non-unique or unstable. The non-uniqueness in the solution of an inverse problem and the stability problem are due to the lack of sufficient information to constrain the solution (e.g., Jackson, 1979; Anger, 1990; Lai and Wilmanski, 2005). In fact, "a lack of information in the solution of a problem cannot be remedied by any mathematical

trickery" (Lanczos, 1961). The questions of the uniqueness and stability of the solution are illustrated by Zhdanov (2002) who asserts that it is impossible to distinguish two models generating the same data from the observed data.

In order to over come these problems and obtain a formal solution of the ill-posed inverse problem, a technique called regularization is employed. This present-day technique on the mathematical treatment of ill-posed problems introduced in the 1960's by Tikhonov, remarkably formalized a solution of ill-posed problems (Tikhonov et al., 1977). Tikhonov suggestion was that the challenge of finding an inverse problem to ill-posed problems can be dealt with by turning them into well-posed problems through some mathematical manipulations. Such operations would cause a solution to exist and possibly the solution be unique. The idea of regularization is defined by (Menke, 2012) as the process of stabilizing the inversion process of an ill-posed problem by imposing constraints that bias the solution. A consequence of the limitations that are put on the solution is that there is a compromise between model resolution and stability. More recently, the regularization theory found a more general and intuitive framework using the theory of probability, which assesses uncertainty about the unknowns and incorporates a priori information into the inverse problem (e.g., Jackson and Matsu'Ura, 1985; Tarantola, 2005 and Ulrych et al. (2001)). There are a number of other regularization schemes that have been developed for example singular value decomposition (SVD), iterative schemes, Marquart-Levenberg method (e.g., Aster et al., 2013; Zhdanov, 1993). In this thesis, we conduct least-square matrix inversion and we will only discuss the most common regularization scheme, known as Tikhonov regularization, which is probably the most successful.

## 3.3 Least squares solution

This approach seeks an approximate solution to a linear seismic inversion problem,

$$\mathbf{d} = \mathbf{Gm} + \boldsymbol{\eta}$$

by minimising the sum of the squares of the difference, measured by the $L_2$-norm, between the actual data and the data derived from the model to be calculated. The vector $\boldsymbol{\eta}$ denotes

the error (noise) and $\mathbf{G}$ is a linear operator mapping the model $\mathbf{m}$ to the data $\mathbf{d}$. This means the least squares solution is given by the model that minimises the squared error,

$$\|\boldsymbol{\eta}\|^2 = \|\mathbf{d} - \mathbf{Gm}\|^2 = (\mathbf{d} - \mathbf{Gm})^T(\mathbf{d} - \mathbf{Gm}) \tag{3.2}$$

As shown in a detailed derivation (Menke, 2012), the value of the model estimate, $\mathbf{m}_{est}$ that minimizes $\|\boldsymbol{\eta}\|^2$ is given by:

$$\mathbf{m}_{est} = (\mathbf{G}^T\mathbf{G})^{-1}\mathbf{G}^T\mathbf{d} \tag{3.3}$$

which is the least squares solution to the inverse problem $\mathbf{d} = \mathbf{Gm}$ where $\mathbf{G}^T$ is the transpose operator. In the least squares estimation, we assumed $(\mathbf{G}^T\mathbf{G})^{-1})$ exists and that we have sufficient information to obtain all model parameters. However, the solution is very often ill-conditioned, that is a small perturbation in the data would give a large perturbation in the estimated model. Therefore, regularization allows us to choose a systematically realistic and stable solution.

### 3.3.1   Tikhonov regularization

Tikhonov regularisation is the most commonly used technique to give preference to a particular realistic solution with the desired properties when dealing with ill-posed problems whose data contain noise. This is achieved by including a regularization term in the minimisation of (3.2) such that the unique solution becomes:

$$\mathbf{m}_{est}^{(\lambda)} = min \left\{ \frac{1}{2} \|\mathbf{Gm} - \mathbf{d}\|_2^2 - \frac{\lambda^2}{2} \|\mathbf{Lm}\|_2^2 \right\} \tag{3.4}$$

where $\mathbf{L}$ is an appropriate derivative operator and the scalar parameter $\lambda > 0$ is known as the regularization parameter. The matrix $\mathbf{L}$ acts as a filter which filters undesired model solutions and is either an identity matrix $I_n$ or a derivative operator of first-order or second-order. Typically the matrix is identity and minimizes the norm. Since $\mathbf{L}$ influences the model $\mathbf{m}$, it can be modified by adding terms to give special attention to several aspects of the solution. The regularization parameter $\lambda$ describes the balance between minimizing the residual norm $\|\mathbf{Gm} - \mathbf{d}\|_2^2$ and the solution norm $\|\mathbf{m}\|_2^2$. The accuracy of the estimated solution depends on

the selected regularization parameter. The solution of the linear least square problem (3.4) can be written as,

$$\mathbf{m}_{est}^{(\lambda)} = (\mathbf{G}^T\mathbf{G} + \lambda^2 I)^{-1}\mathbf{G}^\mathbf{T}\mathbf{d} \tag{3.5}$$

A very small $\lambda$ implies that (3.4) is equivalent to the minimization of the residual function, which can result in an unstable undesired solution. On the other hand, a very big $\lambda$ implies that (3.4) is equivalent to the minimization of the model function, which will make the solution to be closer to the a prior model. There exists an optimal regularization parameter $\lambda$ that gives the most meaningful and stable solution. A number of methods including L-curve analysis, discrepancy principle and generalised cross-validation (Aster et al., 2013) can be used to select the optimal regularization parameter. In this thesis, we find the optimal $\lambda$ by utilising the technique of L-curve analysis (Hansen, 1998).

The L-curve is basically a log-log plot of the solution norm versus the residual norm for different possible regularization parameters. The plot gives us an understanding of how the residual norm and solution norm changes as the regularization parameter $\lambda$ varies. A very small $\lambda$ decreases the residual norm and increases the solution norm. A very big $\lambda$ decreases the residual norm and increases the solution norm. The optimal value of the regularisation parameter $\lambda$, as suggested by many references is the one that corresponds to the corner of the curve as shown in Figure 3.1.
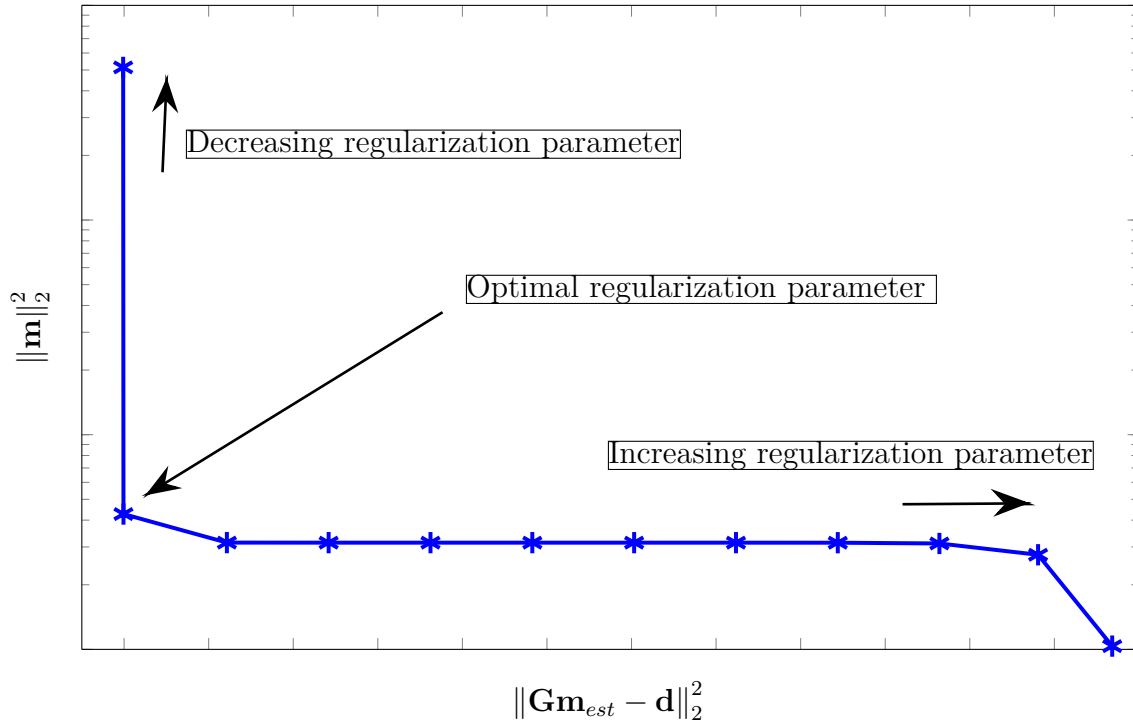
Figure 3.1: Typical example of a plot of L-curve: The L-curve has the characteristic L-shape appearance that justifies its name (Hansen, 1998). The L-corner gives a good approximation of the optimal regularization parameter.

## 3.4   Numerical example

In this section, we demonstrate the important features of the inverse problem and the concept of regularization using a toy example similar to the one considered by (Zhang, 2006b) but with a different model. A number of seismic scattering problems can be described by using boundary integral equations. We therefore generate a set of synthetic data **d** from a model **m**:

$$d_g = d(r_g) = \int_0^Y e^{-2\beta(r_g - x)^2} m(x) dx, \tag{3.6}$$

We assume $d_g$ are $N$ observations distributed along the interval $[0, Y]$ such that;

$$d_g = j.Y(N-1), \ g = 0, 1...N-1. \tag{3.7}$$

where $d_g$ is the recorded data and $r_g$ represents the position of the receivers recording the observations. The integral equation above must be solved numerically by discretizing it using

the trapezoidal rule in order to generate the synthetic data and to set up the inverse problem:

$$d(r_g) = \sum_{j=0}^{M-1} \Delta x e^{-2\beta(r_g-x_j)^2} m(x_j), \ j = 0, 1, 2...N - 1 \tag{3.8}$$

The integral equation (3.6) can then be written as a linear system in the form $\mathbf{d} = \mathbf{Gm}$ after constructing the kernel matrix $\mathbf{G}$. We choose the following values for the parameters: $N = 25$, $Y = 2$, $\beta = 80$, $M = 10$

Since we are interested in studying the effect of noise, we add ten percent Gaussian noise level to clean data to obtain an observation data vector containing noise. Our objective is to attempt to recover estimates of the model parameters given by the profile illustrated in Figure 3.2(a) from the noisy observational data. Figure 3.2(c) shows the least squares solution. The solution attempts to exactly fit the noisy data as seen in Figure 3.2(d). However, this is not a good suggestion since our interest is not to fit the noise and estimate the noisy observations as accurate data.

A very useful approach to this problem is to consider regularization. We therefore apply Tikhonov regularization approach by plotting a trade-off diagram also known as the L-curve. Figure 3.3 shows the L-curve for the toy example inverse problem. The result in 3.3(a) is as a result of plotting a wide range of values of $\lambda$ while 3.3(b) shows a zoomed in bend of the L-curve using a small range of regularization parameter values around the corner. The bend in the L-curve gives an optimal solution.

Figure 3.4 shows the effect of regularization. The estimated data obtained after regularization do not fit the noisy data which is a good idea since our interest is to fit the data with a certain degree of tolerance. The regularization parameter selected is along the corner of the L-curve. However, the extent to which regularization controls the solution is determined by the value of the parameter $\lambda$ selected. As shown in Figure 3.5(d), we see that in a case where $\lambda$ is selected to be too small, the influence of the regularization term is very small. The solution is almost a good fit to the noisy data. This is similar to having no regularization and results in an unstable incorrect solution. On the other hand, the selection of a very large regularization parameter $\lambda$ largely influences the solution norm stabilizing function compared

to the residual norm. Figure 3.6(d) clearly shows that the estimated data does not fit the noisy observations at all. The noisy observed data is therefore totally ignored in the inversion.

The above examples give us an insight into the critical question in the regularized solution of the inverse problem regarding the selection of the optimal regularization parameter. The accuracy of the true solution approximated by the regularised one ultimately depends on the regularization parameter $\lambda$ selected. It is therefore important to choose the most meaningful and stable solution from a set of solutions.

## 3.5   Summary

In this chapter, we reviewed the fundamentals of inversion theory in general and in particular discussed the notion of ill-posed and well-posed problems, inversion of ill-posed problem, least squares solution and the concept of regularisation. We reviewed the most common method of Tikhonov regularization and the L-curve technique. We finally demonstrated some of the important features of the least squares inverse problems and the idea of regularization using a toy example.
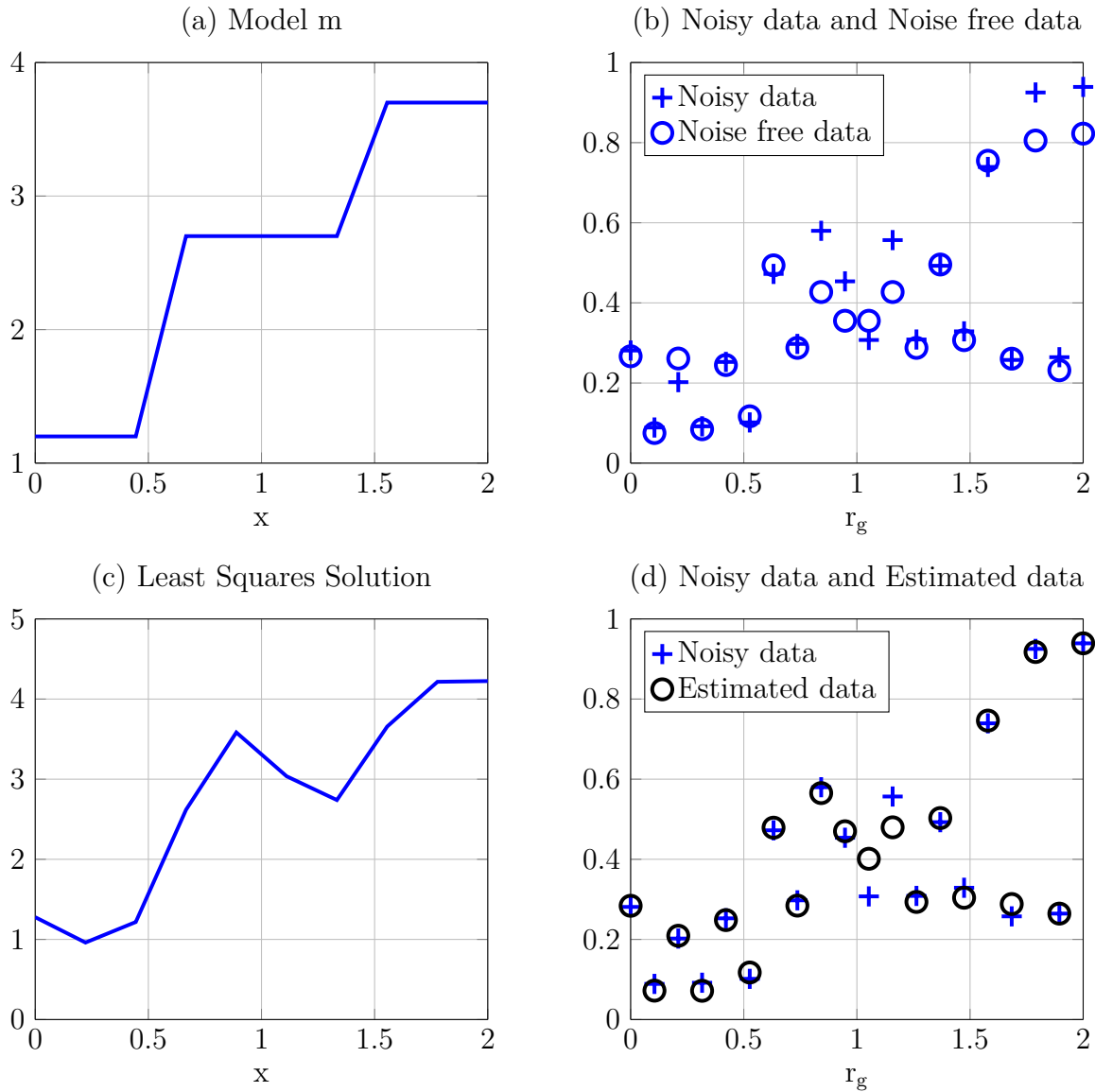
Figure 3.2: (a) Model profile. (b) Noisy observed data and noise free data. (c) Least squares solution. (d) Estimated data and noisy observations. In both (b) and (d), $r_g$ is the position of the observation and $x$ indicates the position of model parameter.
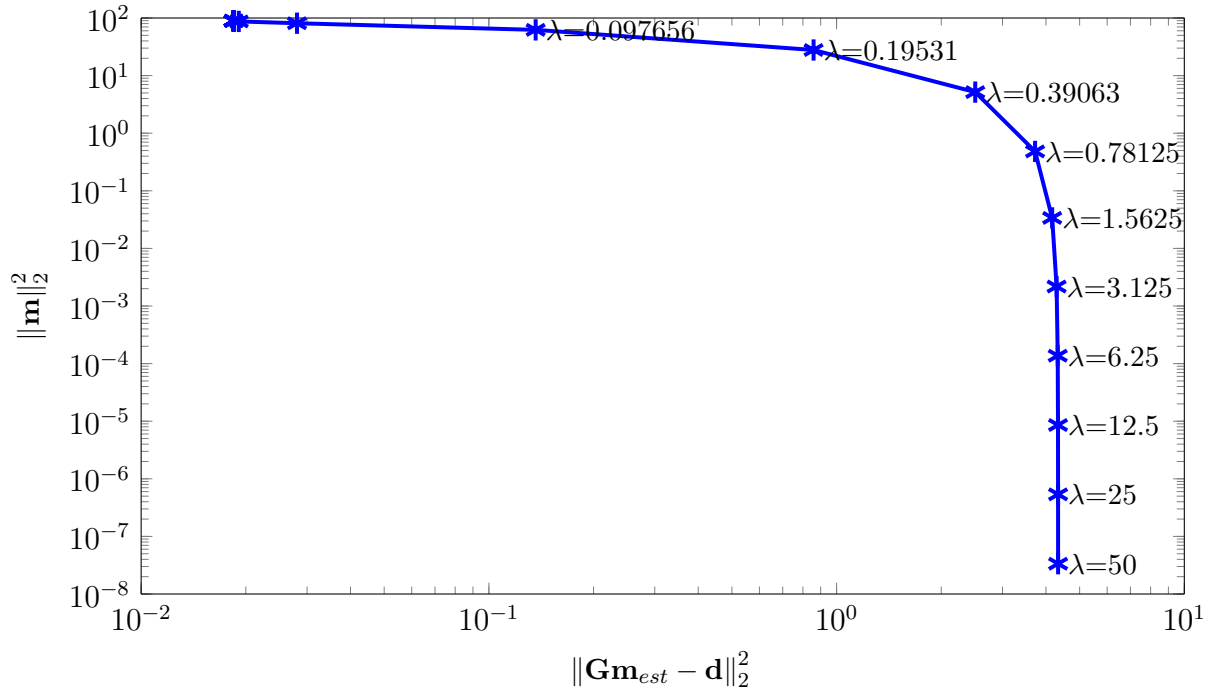
(a) Overview of the L-curve result for the toy example.
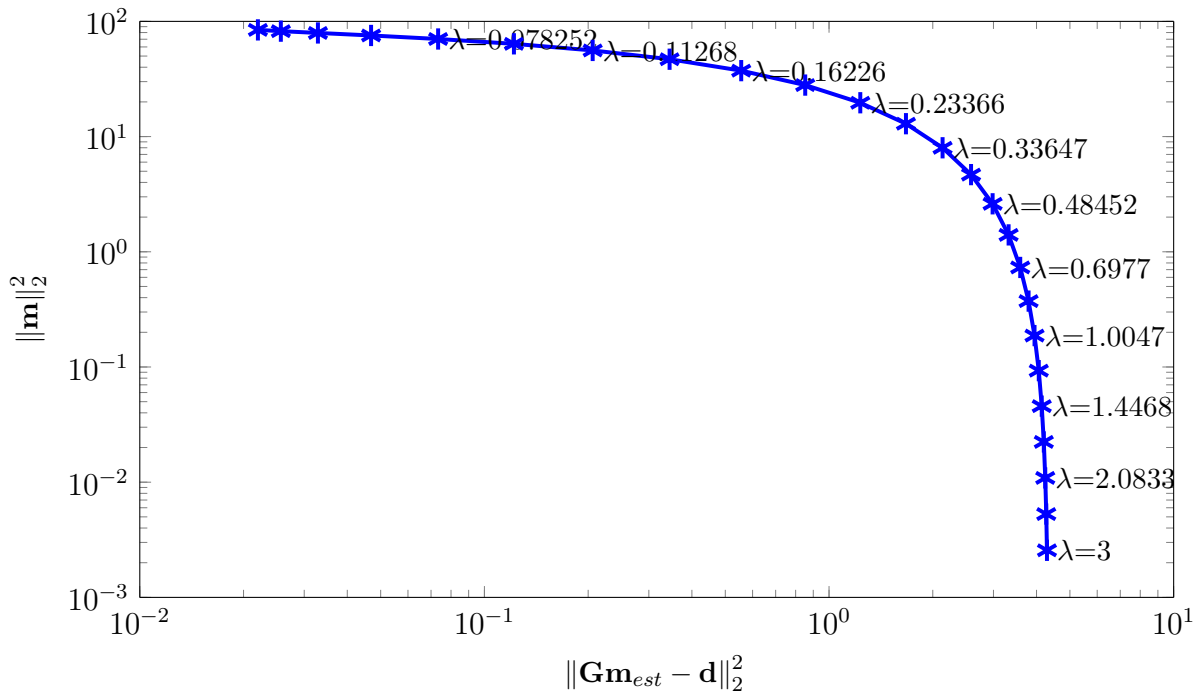


(b) A view of the L-curve corner examined in detail

Figure 3.3: L-curve plot of the two terms in equation(3.4) for a range of different values of the regularisation parameter $\lambda$ used to chose the best parameter value.
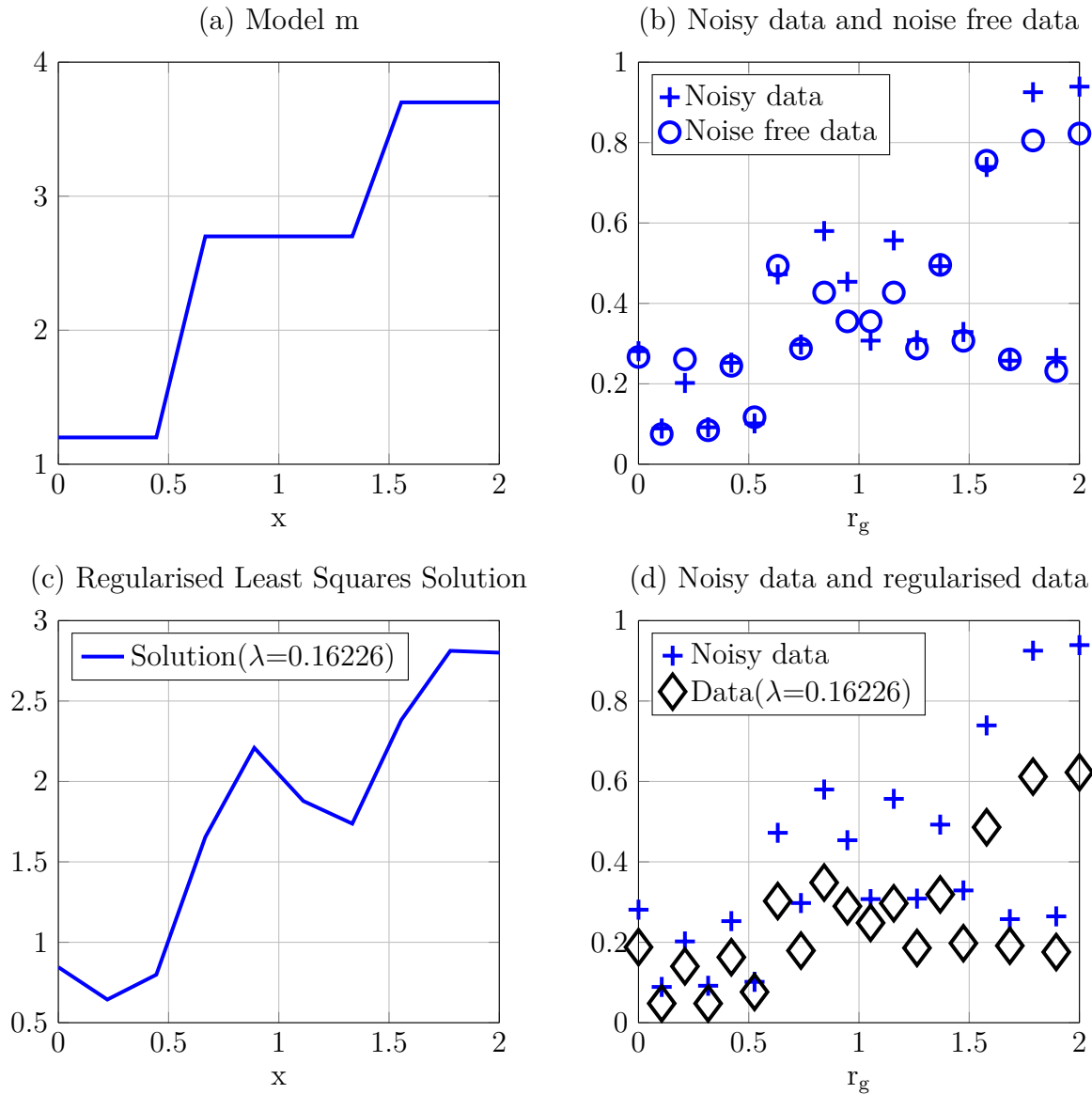
Figure 3.4: (a) Model profile. (b) Noisy observed data and noise free data. (c) Regularized least squares solution. (d) Estimated data after regularization and noisy observations. In both (b) and (d), $r_g$ is the position of the observation and $x$ indicates the position of model parameter.
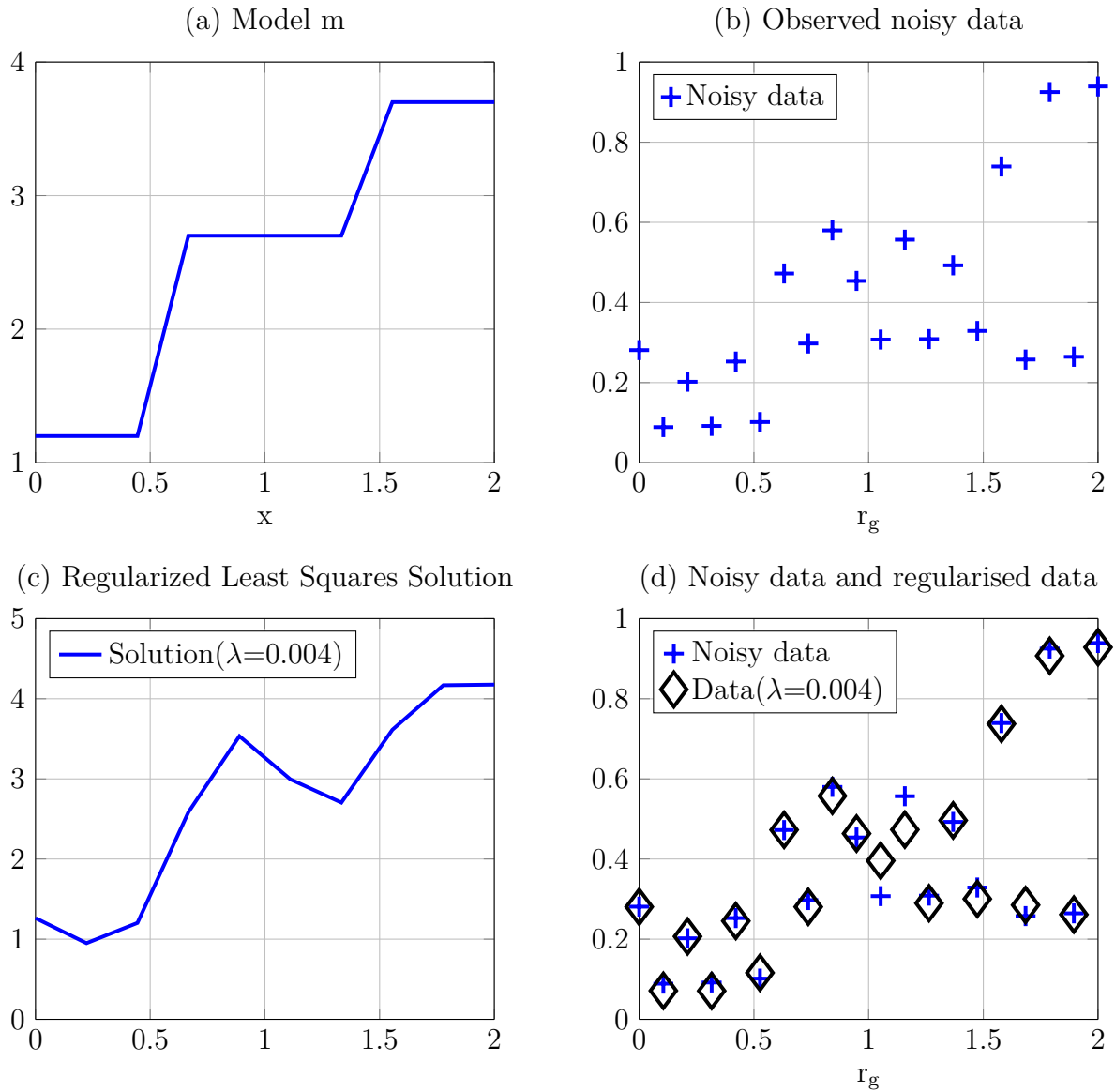
Figure 3.5: (a) Model profile. (b) Noisy observed data. (c) Regularized least squares solution for a very small regularization parameter value. (d) Estimated data after regularization and noisy observations.In both (b) and (d), $r_g$ is the position of the observation and $x$ indicates the position of model parameter.
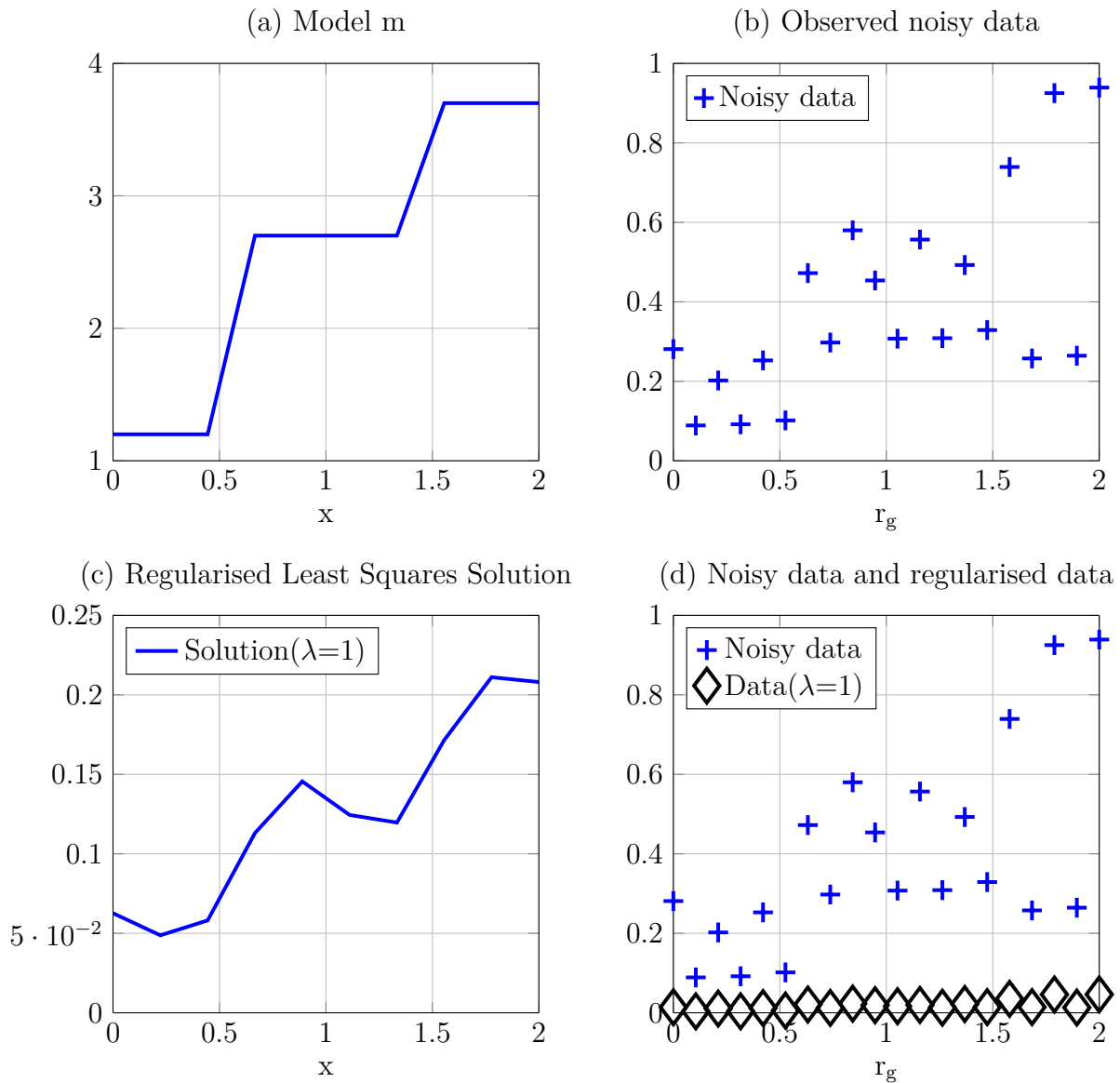
Figure 3.6: (a) Model profile. (b) Noisy observed data. (c) Regularized least squares solution for a very large regularization parameter value. (d) Estimated data after regularization and noisy observations.In both (b) and (d), $r_g$ is the position of the observation and $x$ indicates the position of model parameter.

# Chapter 4

# Frequency-Domain Acoustic Waveform Inversion

## 4.1 Introduction

Waveform inversion methods can be used to obtain high-resolution images of the elastic parameters of petroleum reservoirs under production from time-lapse seismic data. The recent proven success of waveform inversion applications in time-lapse problems has led to the development of different time-lapse data inversion strategies that have been applied to both synthetic and real data. These strategies that include parallel difference, sequential difference and double-difference have been discussed for example in relation to full waveform inversion (FWI)(e.g., Maharramov and Biondi, 2014; Asnaashari et al., 2015; Raknes and Arntsen, 2014; Zhang and Huang, 2013) and linearized waveform inversion (Ayeni et al., 2011).

The major concern in many FWI methods especially for 3D full elastic media is the computational cost of the forward problem which dictates the scope of inversions. Computational costs may be greatly reduced by developing the forward problem using alternative methods such as first-order scattering and testing the settings in which they are valid. Indeed, Innanen et al. (2011) was convinced that inversion for a small time-lapse variation corresponding to difference data can be achieved using standard inverse scattering algorithms without the need for new imaging algorithms. Due to its simplicity, inverse acoustic modelling makes it possible

to estimate the basic time-lapse parameter changes such as P-wave velocity ($V_P$) from the information in seismic data measurement (e.g., amplitudes, travel times, diffractions) and to investigate many different scenarios. From this point of view, we can consider linear waveform inversion of synthetic data generated using acoustic Born approximation (within its limits of validity) and reconstruct time-lapse velocity model changes of the subsurface.

However, the problem that makes linearised waveform inversion methods often unappealing, is that the forward problem is almost always described by a non-linear relationship between data spaces and model. This therefore suggests the use of more robust non-linear methods that consider the full information contained in the seismic wavefield. Several non-linear inversion methods that are relatively computationally less expensive compared to the traditional FWI have been developed for solving non-linear inverse problems. These methods, among others, include; the use of simultaneous coded sources (Ben-Hadj-Ali et al., 2011), sparse model representation (Ma et al., 2012), Hybrid Ray-born and Finite difference (Tengesdal et al., 2014) and using direct iterative T-matrix method (Jakobsen and Ursin, 2015). In order to improve the characterisation of time-lapse changes, we also apply the non-linear direct iterative T-matrix method based on the Distorted-Born approximation (Jakobsen and Ursin, 2015). The waveform inversion approaches presented do not require to preserve seismic amplitudes and identify seismic phases as in AVO analysis (Tura and Lumey, 1999; Vesnaver et al., 2001; Landrø, 2001) and may be more robust compared to the conventional time-lapse AVO inversion. This is due to the use of the waveforms resulting from scattered wavefield related to time lapse changes as opposed to just the use of amplitudes in AVO analysis.

In this chapter, we demonstrate the potential of linear waveform (Born) inversion based on the least squares solution for simple time-lapse velocity models. We also apply non-linear waveform inversion based on Distorted Born iterative T-matrix method to the time-lapse problems in our numerical examples. We invert for $V_P$ using two different strategies (subsequent section) to investigate which approach would improve the image of reservoir velocity changes, maintain relatively low levels of image artefacts and provide accurate quantitative estimates of time-lapse velocity changes in the absence and presence of noise effects. We choose to use Tikhonov regularization for this particular ill-posed inverse problem. In all numerical

examples, our data model is acoustic but the use of Born approximation in elastic media can easily be adopted.

## 4.2   Born inversion method

Born inversion which is a linear inversion approach based on Born approximation is still popular and applicable in cases where the Born approximation is valid. The inversion is linearized in a least-square sense. This involves solving the inverse problem by minimizing a cost function consisting of the data residual (differences between the actual data and the modelled data) and the data misfit as shown in Equation (3.2).

In our Born formulation, the data consists of velocity (slowness) fields. Our goal is to perform inversion and reconstruct the 2D velocity model $\mathbf{c}(x)$ of the subsurface using the seismic data $\mathbf{d}(\mathbf{x}_r, \mathbf{x}_s, \omega)$ recorded by receivers located at $\mathbf{x}_r$ due to sources located at $\mathbf{x}_s$. Following the discussion presented in Section 2.4.1, the seismic data is generated with the discretized Born approximation formulation in Equation (2.30) which is a linear relation between the model parameter $\mathbf{m}$ and the synthetic seismic data $\mathbf{d}$. The data vector $\mathbf{d}$ contains all the different frequency components of the scattered wavefield at all receivers for all sources and $\mathbf{m}$ is a vector of model parameters containing the contrasts between the background and true velocity model of all the different scattering objects or reservoir grid cells.

The inverse problem represented by Equation (2.30) is linear but may be mixed determined and thus, the equation is solved as a least-squares problem with Tikhonov regularization by applying Equation (3.4). The inversion process retrieves the model function $\mathbf{m}(x)$. By using the definition for $m(\mathbf{x}) = \frac{c_0^2}{c^2(\mathbf{x})} - 1$ (Equation (2.21), the inverted velocity model $c_{est}$ can be obtained using the relation

$$c_{est} = \sqrt{\frac{c_0^2}{1 + m(x)}}. \tag{4.1}$$

Although Born seismic inversion (linear form) is characterised by simple and fast optimization schemes, it may fail to give accurate results even when Born approximation is valid (Ramm, 2005). In addition, it cannot be used in cases where the validity limits of Born approximation are exceeded. To overcome such challenges a non-linear approach may be suitable.

## 4.3 Iterative non-linear inversion

Iterative inversion approaches have for long been used to perform non-linear seismic inversion in order to overcome the assumptions implicit in linear inversion. This is achieved by reducing a non-linear inverse problem into a sequence of linear inverse problems. Within the inverse scattering approach, it requires that the wavefield within the scattering domain is updated after each iteration. Inspired by the work of Jakobsen and Ursin (2015) on the non-linear inverse scattering problem using direct iterative T-matrix methods, we particularly apply the Distorted Born iterative T-matrix method (DBIT) developed to solve seismic time-lapse problems.

### 4.3.1    Distorted Born iterative T-matrix method

The DBIT method like any other method based on distorted Born iterative (DBI) is motivated by expressing the field scattered by a medium relative to a heterogeneous assumed background. The underlying difference between DBIT and DBI is the use of a variational T-matrix method for a dynamic background medium in the DBIT. This follows from combining the T-matrix approach (Jakobsen, 2012) with the distorted-Born formulation discussed in Section 2.5.1. In DBIT, the Green's functions in the background medium are updated after each iteration using the T-matrix approach. The independence of the T-matrix on the source-receiver geometry suggests that, DBIT may be useful in time-lapse seismics and therefore testing its robustness in such applications is of critical importance. We follow the treatment given in (Jakobsen and Ursin, 2015) to deduce the formulas inherent in the DBIT inversion approach.

We begin by introducing the T-matrix perspective into the Distorted Born approximation. The source-independent Dyson equations (2.45) and (2.46) can be re-written exactly by considering the fundamental definition of the T-matrix derived in Appendix A as

$$\bar{\mathbf{G}}_{RV} = \bar{\mathbf{G}}_{RV}^{(0)} + \bar{\mathbf{G}}_{RV}^{(0)} \mathbf{T} \bar{\mathbf{G}}_{VV}^{(0)}, \tag{4.2}$$

$$\bar{\mathbf{G}}_{VV} = \bar{\mathbf{G}}_{VV}^{(0)} + \bar{\mathbf{G}}_{RV}^{(0)} \mathbf{T} \bar{\mathbf{G}}_{VV}^{(0)}. \tag{4.3}$$

A similar treatment can be given to the source-independent Dyson equations (2.47) and (2.48) such that they can be rewritten exactly as

$$\mathbf{G}_{RS} = \mathbf{G}_{RS}^{(0)} + \bar{\mathbf{G}}_{RV}^{(0)} \mathbf{T} \mathbf{G}_{VS}^{(0)}, \tag{4.4}$$

$$\mathbf{G}_{VS} = \mathbf{G}_{VS}^{(0)} + \bar{\mathbf{G}}_{VV}^{(0)} \mathbf{T} \mathbf{G}_{VS}^{(0)}. \tag{4.5}$$

The formulation above allows us to use the T-matrix to compute and update Green's functions in the background medium.

Introducing a variation in the T-matrix $\delta\mathbf{T}$, a variation in the scattering potential $\delta\mathbf{V}$ and setting the background model to be equal to the model from the previous iteration, we can obtain a linear relation between the dynamic data residual for two iterations and the related variation in the scattering potential. This makes it possible to avoid the inversion of a huge matrix at each iteration while introducing some approximations into the model updating procedure (Jakobsen and Ursin, 2015) and greatly reduces the computational cost. The waveform inversion is implemented in the frequency domain. Figure 4.1 shows the work flow for the waveform inversion with the relevant formulas.
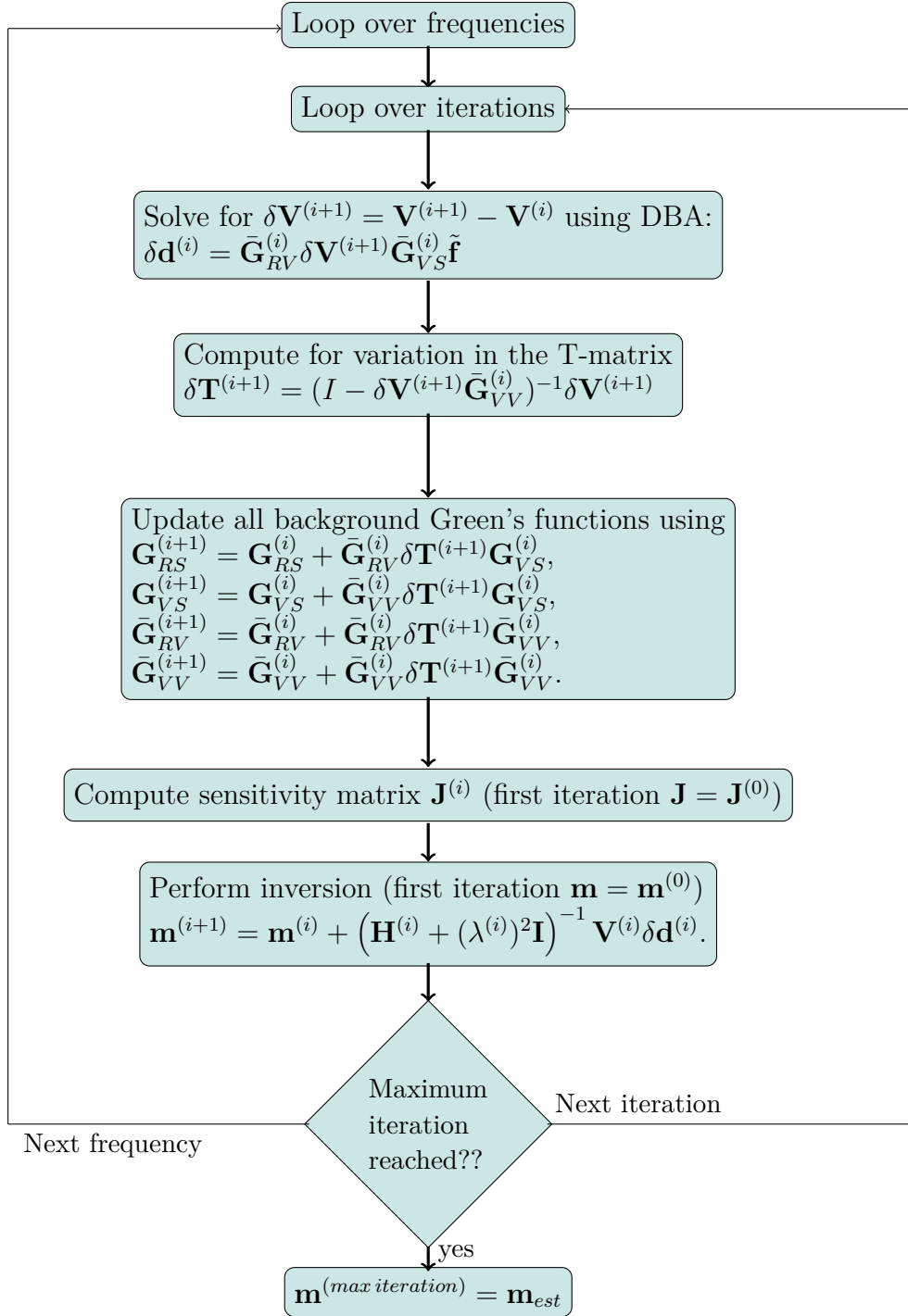
Figure 4.1: The DBIT method work flow for waveform inversion.

The implementation for multiple sources and frequencies is discussed in Section 2.5.1 and the computation of the sensitivity matrix $\mathbf{J}^{(i)}$ and data residual vector $\delta\mathbf{d}^{(i)}$ at iteration $i$

follow as in Equations (2.52) and (2.59) respectively such that

$$\delta\mathbf{d}^{(i)} = \mathbf{J}^{(i)}\delta\mathbf{m}^{(i+1)}. \tag{4.6}$$

In the flow chart shown in Figure 4.1, the parameters $\mathbf{V}^{(i)}$ and $\mathbf{H}^{(i)}$ represent the gradient vector and Hessian matrix at the $i$-th iteration defined as (Jakobsen and Ursin, 2015)

$$\mathbf{V}^{(i)} = \Re\left[\left(\mathbf{J}^{(i)}\right)^{\dagger}\delta\mathbf{d}^{(i)}\right], \tag{4.7}$$

$$\mathbf{H}^{(i)} = \Re\left[\left(\mathbf{J}^{(i)}\right)^{\dagger}\mathbf{J}^{(i)}\right]. \tag{4.8}$$

The data residual $\delta\mathbf{d}^{(i)}$ at the $i$-th iteration is obtained by subtracting the quantity $\mathbf{J}^{(0)}\mathbf{m}^{(i)}$ from the observed scattered wavefield relative to the initial model $\delta\mathbf{d}_{obs}^{(0)}$ given as

$$\delta\mathbf{d}^{(i)} = \delta\mathbf{d}_{obs}^{(0)} - \mathbf{J}^{(0)}\mathbf{m}^{(i)}. \tag{4.9}$$

The regularization parameter $\lambda^{(i)}$ stabilises the solution at each iteration $i$ since the inversion problem is ill-posed. In this particular inversion scheme, $\lambda^{(i)}$ at the $i$-th iteration is chosen using (Farquharson and Oldenburg, 2004)

$$\lambda^{(i)} = max(\lambda a^{(i-1)}, \lambda^{*}), \tag{4.10}$$

where $\lambda^{*}$ is the optimal value of the regularization obtained using the L-curve method and $0.1 < a < 0.9$ (Jakobsen and Ursin, 2015).

## 4.4   Inversion strategies to time lapse data

We consider two inversion strategies hereinafter called sequential and differential approach (Figure 4.2). In the sequential approach to time-lapse seismics, different seismic waveform data corresponding to different times and stages of production may be inverted separately for the corresponding elastic properties. Let us assume two different data sets (baseline $\mathbf{d}_b$ and monitor $\mathbf{d}_m$) corresponding to different times and stages of production. The sequential

approach involves performing baseline model $\mathbf{m}_b$ inversion and monitor model $\mathbf{m}_m$ inversion separately by solving the following least squares optimization problems:

$$
\begin{aligned}
\mathbf{m}_b^{est} &= min\left\{ \frac{1}{2}\left\|\mathbf{G}_b\mathbf{m}_b - \mathbf{d}_b\right\|_2^2 - \frac{\lambda_1^2}{2}\left\|\mathbf{L}\mathbf{m}_b\right\|_2^2 \right\} \\
\mathbf{m}_m^{est} &= min\left\{ \frac{1}{2}\left\|\mathbf{G}_m\mathbf{m}_m - \mathbf{d}_m\right\|_2^2 - \frac{\lambda_2^2}{2}\left\|\mathbf{L}\mathbf{m}_m\right\|_2^2 \right\}
\end{aligned}
\tag{4.11}
$$

where $\mathbf{G}$ is the linearised modelling operator, $\mathbf{m}^{est}$ is the inverted model, $\mathbf{L}$ is an appropriate derivative operator ( identity matrix in our case), $\lambda_1$ and $\lambda_2$ correspond to baseline and monitor inversion regularization parameters and the subscripts $b$, $m$ denote the baseline and monitor survey respectively. After inversion, the difference between the inverted baseline and inverted monitor models ($\mathbf{m}_m^{est} - \mathbf{m}_b^{est}$) correspond to the time-lapse variation $\Delta\mathbf{m}_{est}$.

Within the context of sequential inversion approach, we can also supply the baseline as the starting model for the monitor inversion known as the sequential difference (e.g., see Asnaashari et al., 2015). This approach may be advantageous in that it is not affected too much by repeatability issues of the two acquisition surveys (baseline and monitor). However, it still does not focus only on the time-lapse changes. From the implementation point of view, the sequential difference approach should reduce the number of iterations needed to reconstruct the monitor model since we are starting from the baseline model. We expect that if the baseline model is close to the monitor model (as in most time-lapse problems), the reconstruction of time-lapse changes should be improved greatly.

In the differential approach, however, changes in the seismic waveform data between two surveys may also be inverted for changes in the corresponding elastic parameters. In this case, we can directly invert for the time-lapse variation, $\Delta\mathbf{m}_{est}$ (Ayeni and Biondi, 2010). The inversion of the data difference requires that $\mathbf{G}_b$ and $\mathbf{G}_m$ are the same, such that if $\mathbf{G}_b = \mathbf{G}_m = \mathbf{G}$, the optimization problem for the least inversion becomes:

$$
\Delta\mathbf{m}_{est} = min\left\{ \frac{1}{2}\left\|(\mathbf{d}_b - \mathbf{d}_m) - \mathbf{G}(\mathbf{m}_b - \mathbf{m}_m)\right\|_2^2 + \frac{\lambda^2}{2}\left\|\mathbf{L}(\mathbf{m}_b - \mathbf{m}_m)\right\|_2^2 \right\}
\tag{4.12}
$$

This minimization problem is similar to the optimization problem for one data set in equation (4.11) with the baseline and monitor data replaced by the data difference and the model

replaced by the model difference. One obvious assumption with this approach is that the same size of data vectors is required to be able to make data difference implying same acquisition geometry for both baseline and monitor surveys as a favourable condition. The differential approach is more common, and provides useful qualitative information. However, it is possible that the sequential approach is more stable and robust with respect to effects of random noise and repeatability issues. We compare the two approaches to establish their robustness in reconstruction of time-lapse changes. Time-lapse changes at a reservoir scale are considered as high-frequency details (Asnaashari et al., 2015). This implies that efforts must be made to recover the high frequency content of the seismic data so as to improve the resolution of the reconstructed subsurface image.
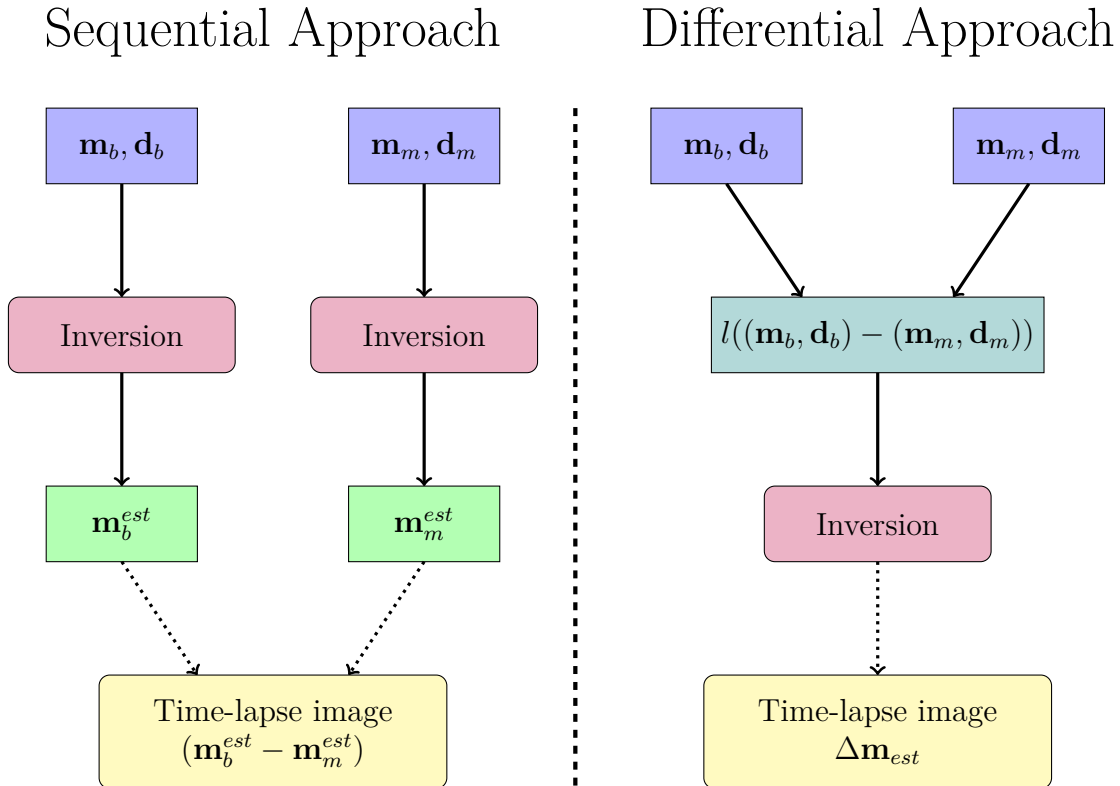
Figure 4.2: An illustration of the general work flow of the sequential and differential approach .

## 4.5   Numerical examples and results

We use three synthetic models to demonstrate the potential of linearized seismic waveform inversion based on Born approximation and DBIT non-linear approach to investigate the

robustness of the two inversion approaches discussed above to image reservoir velocity changes. We study the effects of noise to test which approach may maintain relatively low levels of image artefacts and provide accurate quantitative estimates of time-lapse velocity changes in the absence and presence of noise effects. This is achieved by adding up to approximately 50% random white noise corresponding with a SNR equal to 6 dB. Adding noise not only validates the stability but also makes the numerical experiments more realistic. In our study, the noise is added to the generated clean synthetic data $\mathbf{d}$ using the formula (Jakobsen and Ursin, 2015):

$$\mathbf{d}^{noisy} = \mathbf{d} + \frac{|\mathbf{d}|}{\sqrt{SNR}} \cdot \frac{\boldsymbol{\eta}}{|\boldsymbol{\eta}|}, \qquad (4.13)$$

where $\boldsymbol{\eta}$ is a vector with random numbers taken from the Gaussian distribution.

The inversion results are created using the least squares inversion method explained in section 3.3 and Tikhonov regularization whereby the regularization parameter corresponding to a good estimate is obtained using the L-curve method. Figure 4.3 shows the L-curve used to choose the optimum regularization parameter for inversion of noise free data associated with Model 1.

### 4.5.1 Model 1: Time-lapse models with small velocity contrasts

We apply the two inversion approaches, the conventional sequential approach and differential approach to synthetic data for the simple 2D time-lapse velocity model shown in Figure 4.4. The example is based on the time-lapse velocity model used by Abubakar et al. (2003). The P-wave velocity values are varying from 2950 m/s to 3150 m/s. The $V_P$ values in the reservoir of the monitor model are 2% more than those of the baseline model. The models are 1200 m wide and 300 m in depth and is discretized into $80 \times 20$ grid blocks that are 15 m by 15 m in size. The synthetic data were generated using the traditional Born approximation (frequency domain) with a homogeneous background velocity model ($V_P = 3000$ m/s) for all frequencies from 1 to the Nyquist. The Ricker wavelet with central frequency 7.5 Hz for source excitation is used for both baseline and monitor surveys. There are 30 source positions at equidistant horizontal distances with 50 receivers also at equidistant horizontal distance positions. The sources and receivers are placed at the top of the model and cover the entire survey line.

Since good inversion results can be obtained even without the use of the whole frequency spectrum (Bansal and Sen, 2010), we avoid the simultaneous inversion of all frequencies and run the inversion procedure for seventeen multiple frequencies simultaneously. The frequencies are distributed uniformly from 1 Hz up to the Nyquist (50 Hz) in the intervals of 3 Hz. We expect the results for simultaneous inversion to be comparable if the frequency samples beyond 25 Hz are discarded since the amplitude spectrum of the 7.5 Hz is zero beyond 25 Hz ( right panel of Figure 2.2).

The multi-frequency simultaneous inversion method may require considering many frequencies and including higher frequencies to obtain good resolution at the expense of higher computational costs. We therefore challenge this method and employ the frequency-hopping method normally called sequential frequency inversion strategy (e.g., see Sirgue and Pratt, 2004) whereby one frequency data is inverted at a time from the lowest to the highest frequency. For this method, we use only eight frequencies (1, 3, 5, 7, 10, 13, 15, 20). This may be suitable since Born approximation is a low-frequency approximation and the use of fewer frequency samples in the inversion renders the process less computationally expensive.

Figure 4.5(c) shows the time-lapse velocity inversion result obtained by using the sequential approach when the multi-frequency simultaneous inversion method is used . The result in Figure 4.5(c) is obtained by simple subtraction of the inversion results obtained by inverting the baseline and monitor models separately. The top panel (a) and middle panel (b) of Figure 4.5 shows the baseline model inversion result and monitor model inversion result respectively for noise free data. The same inversion results when the frequency-hopping method is used are shown in Figure 4.9. The estimated models resemble the true velocity models in Figure 4.4 and the time-lapse velocity change is recovered quite well in both cases, in spite of the fact that the velocity distributions in the layers are almost identical. The boundary layers are also well resolved. However, the step edges where there is high contrast in the model are not well recovered but well resolved. The frequency-hopping method performs well in regions without complexity but recovers the step-wise edges in the model with higher errors. This is because these interfaces and time-lapse variations require higher frequencies. This illustrates that the low frequencies may not be sensitive to small details. The absolute

values of the differences between the estimated models and true models show that most areas of the baseline and monitor models are reconstructed within less than +/-10 $m/s$ while the time-lapse velocity model recovered within less than +/-5 $m/s$.

The lower panel of Figure 4.6 and Figure 4.10(a) show the time-lapse squared slowness inversion result obtained using differential approach by employing the multi-frequency simultaneous and frequency-hopping inversion methods respectively. In these cases, the difference data between the baseline and monitor survey are inverted using the scheme given in Equation (4.12) to get the estimate of the model difference which is a time-lapse square of slowness change:

$$\frac{1}{\Delta c_{est}^2} = \frac{1}{c_b^2} - \frac{1}{c_m^2}. \tag{4.14}$$

where $c_b$ and $c_m$ denote the baseline survey velocity model and monitor survey velocity model respectively. The absolute values of the differences between the estimated models and true models show that most areas of the time-lapse difference are reconstructed with less than 5% error bound. We notice that both inversion approaches employed recover the time-lapse velocity changes equally well for noise free data and it is difficult to make a conclusion on which approach is the best though Figure 4.13 suggests that the differential approach has slight advantage. Some image artefacts caused by inadequate data coverage appear as seen in Figure 4.13.

Figures 4.7 and 4.11 show the results obtained when inverting the noisy data using the sequential approach by employing multi-frequency simultaneous inversion method and frequency-hopping inversion method respectively. Figures 4.8 and 4.12 show the inversion results for the same noisy data using differential approach. The time-lapse model recovered in both approaches is quite similar to the true model but with less accuracy compared to the results in the absence of noise. This is indeed expected as the inverse problem becomes more ill-posed.

Comparing the multi-frequency simultaneous method results and the frequency-hopping method results using both the sequential and differential approaches, we can observe that they are comparable, although the inverted values obtained using the frequency-hopping method are slightly deteriorated at the step-wise structures in the model when compared

to those values inverted from the multi-frequency simultaneous method. However, noise effects and artefacts are not much pronounced outside the monitoring region in the case of frequency-hopping method. These artefacts which are more noticeable especially when inverting for noisy data using multi-frequency simultaneous method are either due to high frequency components that create false events or an indication of possible divergence from the global minimum in the inversion process. With regard to computational time, the multi-frequency simultaneous method was twice the frequency-hopping method. The results suggest that the frequency-hopping approach (sequential frequency inversion strategy) gives robust results especially in the presence of noise for the time-lapse problem studied.

The differences between the reconstruction capacities of time-lapse changes by the sequential and differential approach in noise-free environments seem to be unnoticeable for linearized inversion but in noisy environments differences exists. Although we may say that both approaches demonstrate robustness with respect to noise in relation to model recovery, the results are improved with the differential approach as seen in Figure 4.13 since the magnitudes of the velocity changes are better reconstructed. Comparing the sequential approach result in Figure 4.11 and the differential approach result in Figure 4.12, we see that the time-lapse model reconstructed by sequential approach shows significant errors outside the areas of time-lapse (target zone). The differential approach is more robust than the sequential one, especially in the presence of noise since the differential inversion approach only focuses on the difference (time-lapse) data. However, we expect a more noticeable difference between the two approaches in the absence and presence of noise with non-linear inversion.

### 4.5.2    Model 2: Time-lapse models with large velocity contrasts

We apply the non-linear inversion approach of the DBIT method to study the robustness and behaviour of this method in reconstructing the time-lapse structural changes for the velocity models shown in Figure 4.19. This model simulates a scenario of large velocity contrasts between the layers as considered by Abubakar et al. (2003). The values of $V_P$ vary from 1500 m/s to 3000 m/s, so the contrasts are extremely large and a simple homogeneous background model combined with Born inversion cannot be efficient for the forward modelling and the

corresponding linear inverse problem. So we use the non-linear scattering approach based on the DBIT method. The $V_P$ values in the reservoir of the monitor model are 8% more than those of the baseline model. The model is also $1200m \times 300m$ and discretized into $80 \times 20$ grid blocks that are 15 m by 15 m in size. The synthetic data is generated using the T-matrix solution (Jakobsen, 2012) in the frequency domain for a selection of frequencies used in the inversion and a Ricker wavelet with central frequency 7.5 Hz for source excitation for both baseline and monitor surveys as in the previous example. There are 30 source positions at equidistant horizontal distances with 50 receivers also at equidistant horizontal distance positions. The sources and receivers are placed at the top of the model and cover the entire survey line.

We attack the inverse problem using both the sequential approach and differential approach. The distorted-Born approximation provides a framework for imaging of regions of time-lapse variation using the baseline survey as a reference and the monitor survey as perturbed to directly estimate the perturbation. In this case, the differential approach involves supplying the baseline as the reference model and reconstructing the time-lapse parameter variations taken as the difference between the inverted monitor and baseline model. For both approaches, the inversion was run for nine frequencies distributed uniformly over the frequency spectrum of the source signature (2.5, 5, 7.5, 10, 12.5, 15, 17.5, 20, 22.5 Hz) and the inversion is performed by inverting one frequency data at a time from the lowest to the highest frequency. We also add 5% random noise (26 dB) as in Abubakar et al. (2003) in order to have a chance of comparing our results. The regularization is achieved using Tikhonov method in conjunction with the scheme in Equation (4.10).

Figures 4.15(b) and 4.15(c) are the baseline and monitor inversion results respectively by independent inversion for noise-free data. Figure 4.16(b) shows the reservoir changes obtained with this sequential approach by simple subtraction of the results from the independent inversion of the baseline and monitor datasets. It is important to note that the same reference (starting) velocity model in Figure 4.15(a) was used for both baseline and monitored inversions. We clearly observe that the location of the time-lapse change (reservoir) is reconstructed, but the magnitude of the seismic velocity change within the reservoir is incorrect in many

areas. The numerical results obtained with the sequential approach after adding noise are shown in Figure 4.17 and Figure 4.18. The baseline and monitor inversion results are obtained by considering the same reference (starting) model. Figure 4.18(b) shows the effects of noise on the time-lapse difference results when sequential approach is applied. Comparing Figures 4.18(a) and 4.18(b), we observe that the location of the time-lapse changes are totally affected and the magnitudes of time-lapse velocity incorrectly reconstructed. This arises because in the sequential approach, the inversions need to reconstruct the entire time-lapse models separately implying that each grid point is updated differently during the independent inversions. This explains why there are so many artefacts within and outside the monitoring area. The sequential inversion approach thus performs poorly especially in the presence of noise effects.

Figure 4.20(b) shows the reservoir changes obtained with the differential inversion approach for noise-free data. The baseline model is used as the dynamic background in the DBIT method. The image of the reservoir in Figure 4.20(b) is improved compared with that in Figure 4.16(b) because the inversion approach focuses on the time-lapse data variation (perturbation) only. Figure 4.19(c) shows the reconstructed monitor model. The true monitor model and the prior model (baseline) are shown in Figures 4.19(b) and 4.19(a) respectively. It can be seen from these numerical results that the retrieved magnitudes of the time-lapse velocity changes using the differential approach are better than those obtained using the sequential approach, but still the magnitude of the seismic velocity change at the step edges of the reservoir is incorrect. Some artefacts outside the reservoir region are also evident but reduced compared to sequential inversion approach. The reconstructed images using differential approach when 26 dB of noise is added are shown in Figures 4.21 and 4.22. As with the noise-free data, the reconstructed images are again much better compared to the ones obtained using the sequential approach. The images are still greatly affected at the step edges of the reservoir.

In general, the differential inversion approach to the time-lapse problem gives improved results compared to the sequential approach. In additional the differential approach perform much better in the inversion of time-lapse data in noisy environments since it attenuates the

artefacts outside the reservoir. However, its worthwhile to note that the DBIT method does not perform impressively well in this case. This could be as a result of very large velocity contrasts within the baseline model and monitor model. Still, the results obtained using DBIT are more convincing than in Abubakar et al. (2003) for reconstructing the velocity changes within the reservoir. In the next section, we investigate whether the results will be greatly improved when we have relatively large contrasts.

### 4.5.3 Model 3: Time-lapse models for monitoring $CO_2$ injection

We construct a 2D model to simulate a $CO_2$ injection scenario with a single injector (Figure 4.27) to monitor the distribution of $CO_2$ after 2 years of injection . This model may not be especially realistic, at least in terms of the depth of the reservoir; but just as an example of the $CO_2$ sequestration aspect. A reduction in $V_P$ values in the reservoir model as a result of injection is simulated using a Gaussian model that simulates the injection of a fluid into a permeable reservoir layer. The true velocity difference between the monitor and baseline (time-lapse model) are shown in the upper panel of Figure 4.28. The model is discretized into $100 \times 40$ grid blocks with a square grid size of 24 m. Each grid block represents the squared slowness at a particular location. We generate synthetic seismic reflection data using 30 sources and 100 receivers evenly spaced along the top boundary of the model. The T-matrix solution is used for forward modelling and the central frequency of the source wavelet is 7.5 Hz, the same as that for the previous examples.

Time-lapse inversion of the difference data is applied using the sequential and differential approaches. The objective is to estimate the change in the velocity values after the injection period of 2 years. The DBIT method is used in inversion by considering six frequencies (1, 3, 7.5, 10, 15 and 18 Hz). To investigate the possibility of using this non-linear approach to noisy data, we add 10% noise corresponding to a SNR of 20 dB and perform the inversion by sequentially inverting one frequency data at a time from the lowest to the highest frequency. In this synthetic inversion example, the same reference velocity model shown in Figure 4.23(a), which is a linearly increasing velocity model, is used for the independent inversion of the baseline and monitor in the sequential approach.

The true monitor model and the reference model (baseline) are shown in Figures 4.27(b) and 4.27(a) respectively. Figures 4.23 and 4.25 show the result obtained using the sequential approach with two independent waveform inversions for noise-free and noisy data respectively. Figures 4.23(b) and 4.23(c) are the baseline and monitor inversion results for the noise-free case. Figures 4.25(b) and 4.25(c) are the baseline and monitored inversion results when noise is added. The time-lapse difference results by sequential and differential inversion approaches are shown in Figures 4.24(b) and 4.28(b) respectively for noise free data . The inversion results using the sequential approach contain some artefacts outside the monitoring area of the reservoir as shown in Figure 4.28 even in the case of noise free data and the time-lapse velocity changes are not accurately recovered.

Comparing Figure 4.30 with 4.26, we observe that addition of noise distorts the time-lapse inversion results tremendously when the sequential approach is used. We, however, obtain a good image of the velocity changes using the differential approach as seen in Figure 4.30. From these numerical results, it is evident that the differential approach to waveform inversion greatly improves the image of the time-lapse changes and the magnitudes of velocity changes within the reservoir are better reconstructed than in the sequential approach. The differential approach also attenuates artefacts in the time-lapse velocity difference and proves to be very efficient since the computational time is even lesser.

Clearly, DBIT performs impressively well in this particular model, reconstructing the noise free data with no artefacts outside the monitoring region and few artefacts for noisy data. The distribution of $CO_2$ is therefore well imaged after injection and the quantitative characterization can be perfectly done. This demonstrates that, DBIT is accurate at least in this model, because the contrasts within the model are relatively large. As with the previous model, we can see that the inversion results obtained using the sequential approach can only give the location of the time-lapse variations, and cannot reconstruct the magnitudes of its velocity changes correctly. In the differential approach to inversion using DBIT method, the location of the reservoir is reconstructed very well and the magnitude of the seismic velocity change within the reservoir and outside the reservoir region is correctly retrieved in the time-lapse (difference) model.

## 4.6 Concluding remarks

This chapter, focussed on the implementation of both linear and non-linear inversion methods based on scattering approaches for different time-lapse inversion strategies. We discussed and implemented Born inversion for an inverse scattering problem where Born approximation may be valid. We formulated the problem as an optimization problem and solved it in the least squares sense. Born inversion performs well and recovers the time-lapse velocity changes both in shape and amplitude for both the sequential and differential approaches considered. However, the differential approach gives improved results because the magnitudes of the velocity changes are better reconstructed and image artefacts outside the monitoring region are greatly reduced since the inversion focuses on inverting time-lapse changes only. Regarding the inversion method, it is showed that the frequency-hopping method (sequential frequency inversion gives more robust results especially in the presence of noise that the multi-frequency simultaneous method.

We also discussed and implemented the non-linear DBIT inversion method that utilises the T-matrix approach from quantum scattering theory. The performance of the method was demonstrated using two numerical examples based on 2D models. The method performs impressively well especially for the $CO_2$ injection model and we are able to obtain good inversion results at a lower computational cost. We at least expect DBIT method to be very useful in seismic monitoring of $CO_2$ sequestration and in modelling time-lapse models with relative large velocity contrasts. We found out that the method may not give very good results for models with extremely large contrasts, at least for time-lapse cases. The resolution of the reconstructed images seems to depend directly on the ability to recover the high frequency content of the seismic data. FWI methods are normally limited to low frequencies but time-lapse variations are normally characterised as high-frequency details in the model. This may be affecting our results but still, we are able to obtain high resolution images with the frequencies we used in our inversion. In addition, it would be interesting to assess the method against the absence of low frequency data and to assess the computation time cost in details.
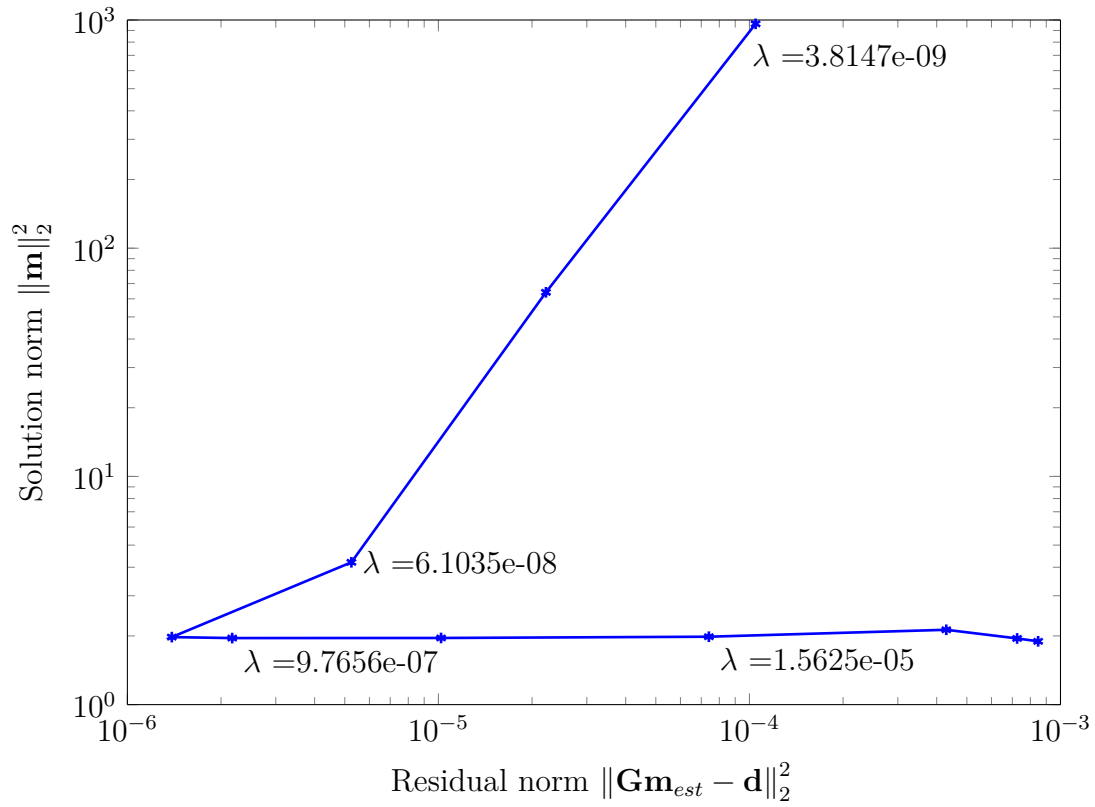
Figure 4.3: L-curve for the regularization parameter corresponding to inversion of model 1 noise free data.
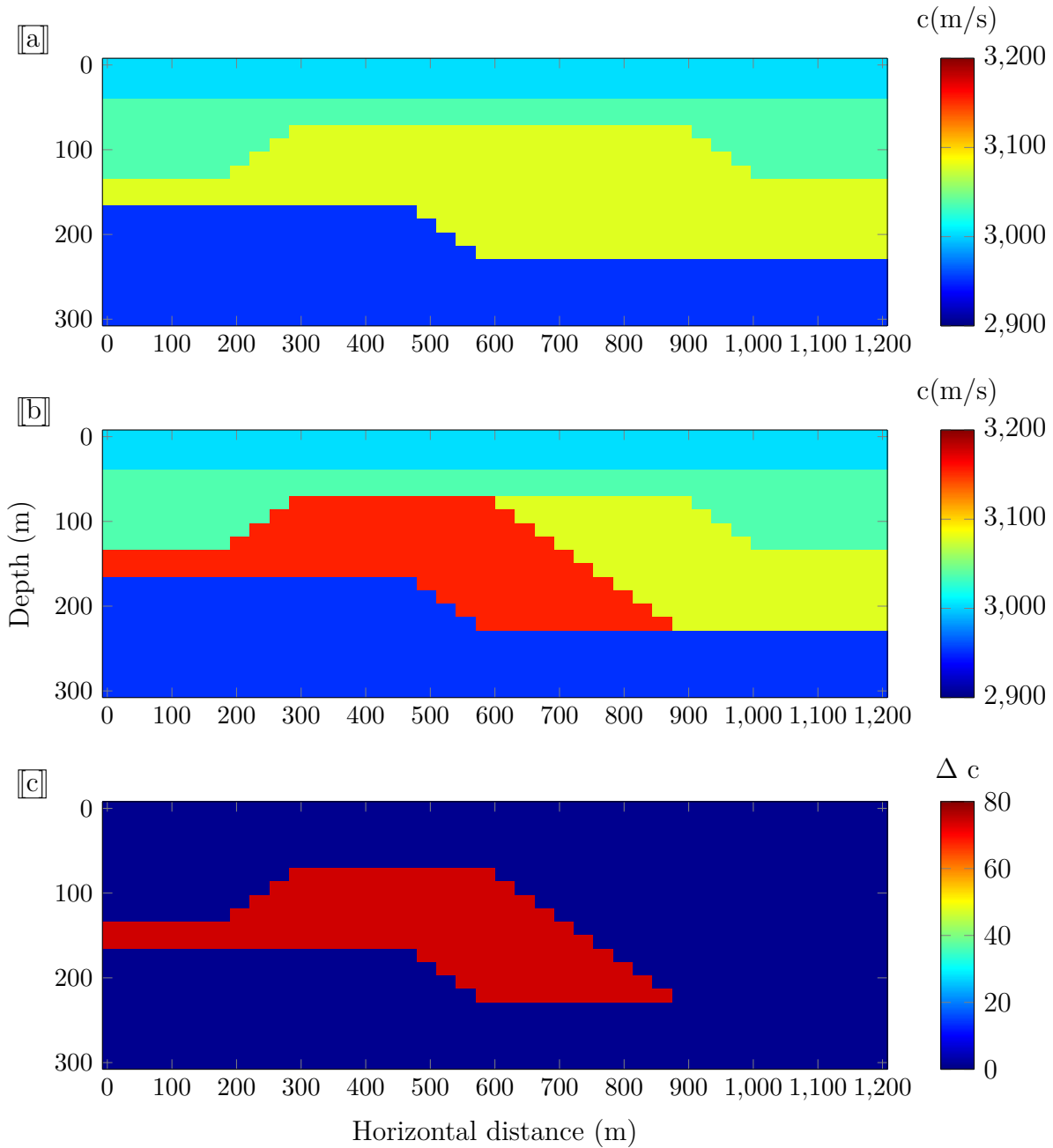
Figure 4.4: The true 2D time-lapse velocity models associated with Model 1: (a) the baseline velocity model; (b) the monitor velocity model; (c) baseline-monitor model difference.

Figure 4.5: Born inversion results of the noise-free data for model 1 in Figure 4.4: (a) the baseline inversion result; (b) the monitoring inversion result; (c) time-lapse difference obtained by the sequential approach (subtracting the recovered baseline model from the recovered monitor model). The results were obtained using a scheme that inverts seventeen frequencies simultaneously from 1-49 Hz with 3 Hz frequency intervals.

Figure 4.6: Born inversion results of the noise-free data for model 1 in Figure 4.4: Upper panel: True time-lapse model showing the square of slowness change. Lower panel: Inverted time lapse difference using the differential approach (inverting directly for monitor-baseline difference data). The results were obtained using a scheme that inverts seventeen frequencies simultaneously from 1-49 Hz with 3 Hz frequency intervals.

Figure 4.7: Born inversion results of the noisy data for model 1 in Figure 4.4: (a) the baseline inversion result; (b) the monitoring inversion result; (c) time-lapse difference obtained by the differential approach (subtracting the recovered baseline model from the recovered monitor model). The results were obtained using a scheme that inverts seventeen frequencies simultaneously from 1-49 Hz with 3 Hz frequency intervals. The signal to noise ratio is 6 dB.

Figure 4.8: Born inversion results of the noise-free data for model 1 in Figure 4.4: Upper panel: True time-lapse model showing the square of slowness change. Lower panel: Inverted time-lapse difference using the differential approach (inverting directly for monitor-baseline difference data). The results were obtained using a scheme that inverts seventeen frequencies simultaneously from 1-49 Hz with 3 Hz frequency intervals. The signal to noise ratio is 6 dB.
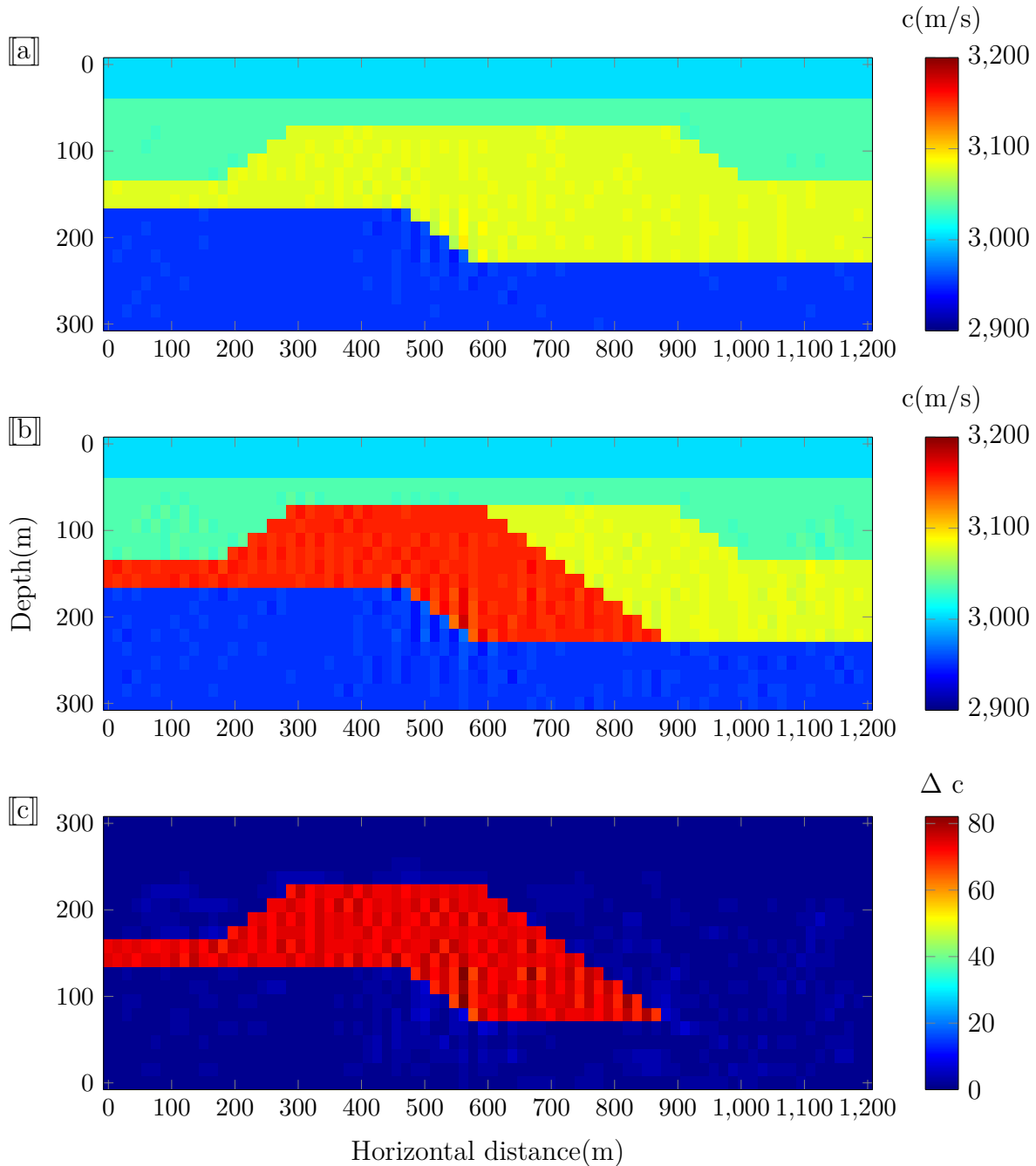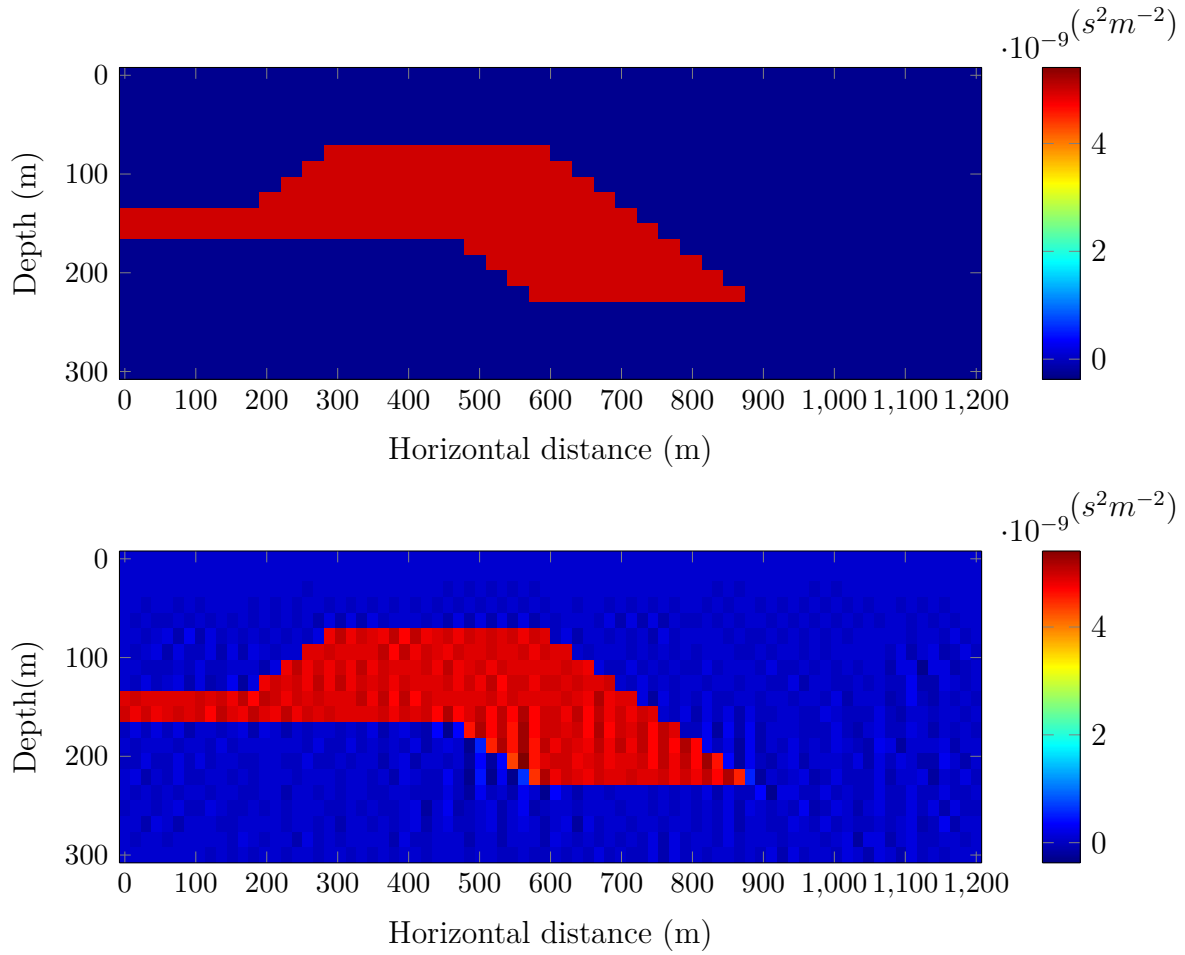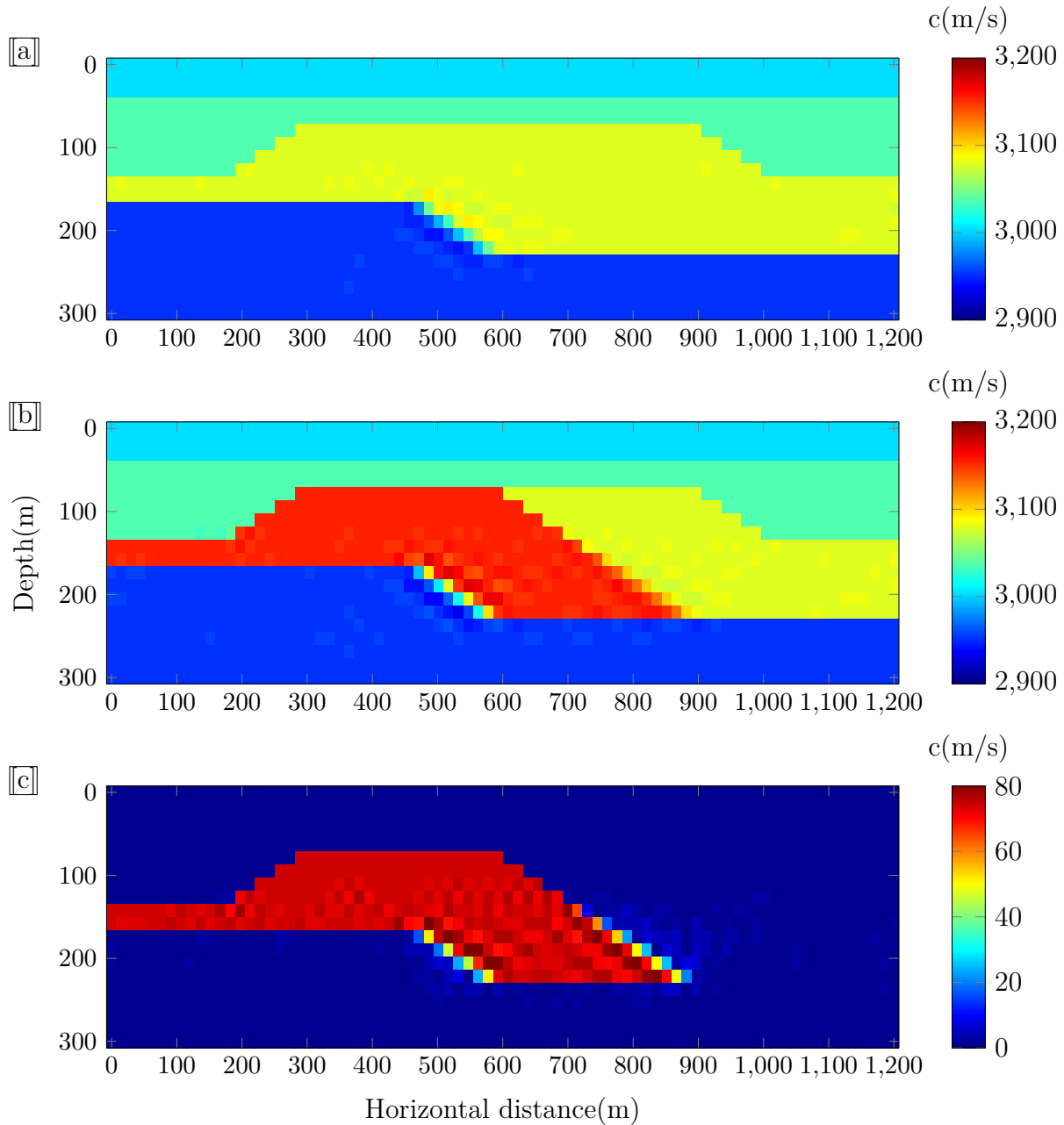
Figure 4.9: Born inversion results of the noise-free data for model 1 in Figure 4.4: (a) the baseline inversion result; (b) the monitoring inversion result; (c) time-lapse difference obtained by the sequential approach (subtracting the recovered baseline model from the recovered monitor model). The results were obtained using a scheme that inverts eight frequencies sequentially referred to, in the text, as the frequency-hopping method.
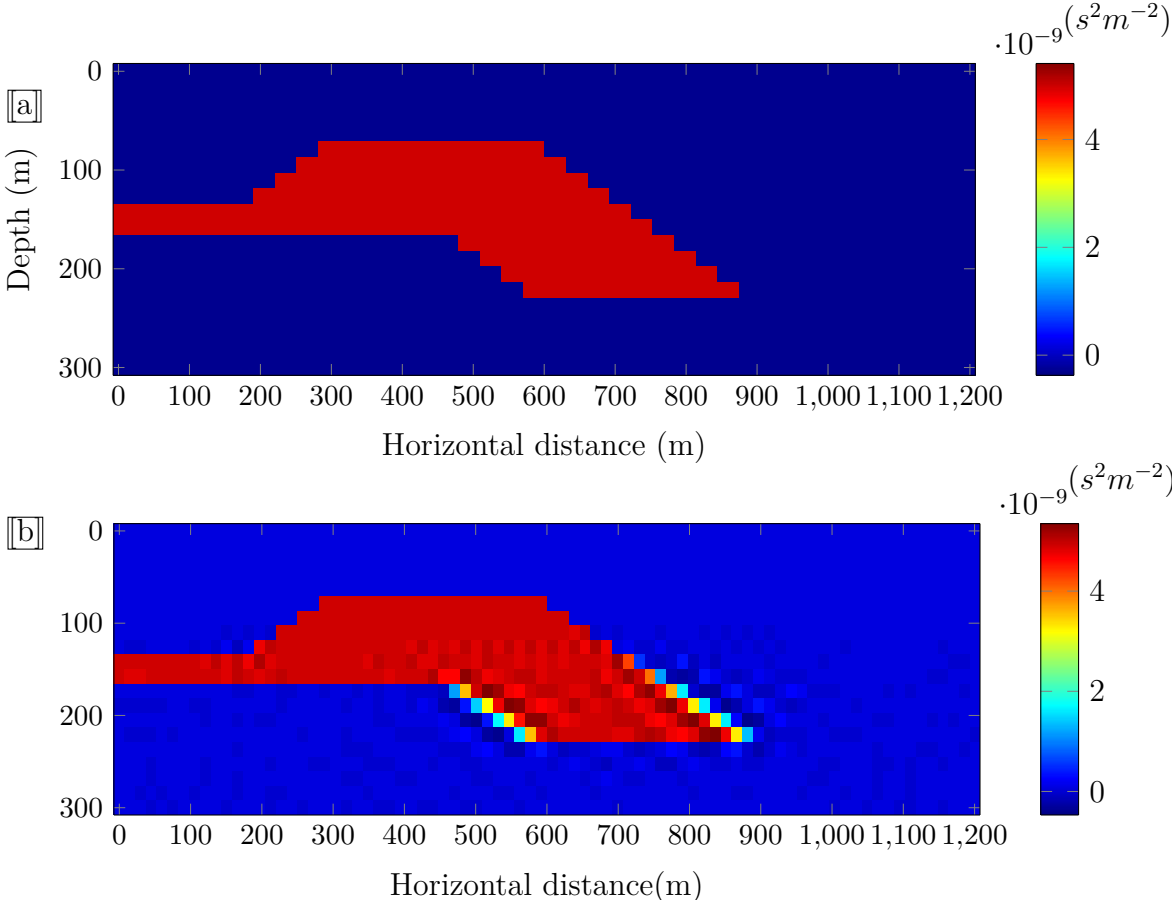
Figure 4.10: Born inversion results of the noise-free data for model 1 in Figure 4.4: (a) True time-lapse model showing the square of slowness change. (b) Inverted time-lapse difference using the differential approach. The results were obtained using a scheme that inverts eight frequencies sequentially referred to, in the text, as the frequency-hopping method.
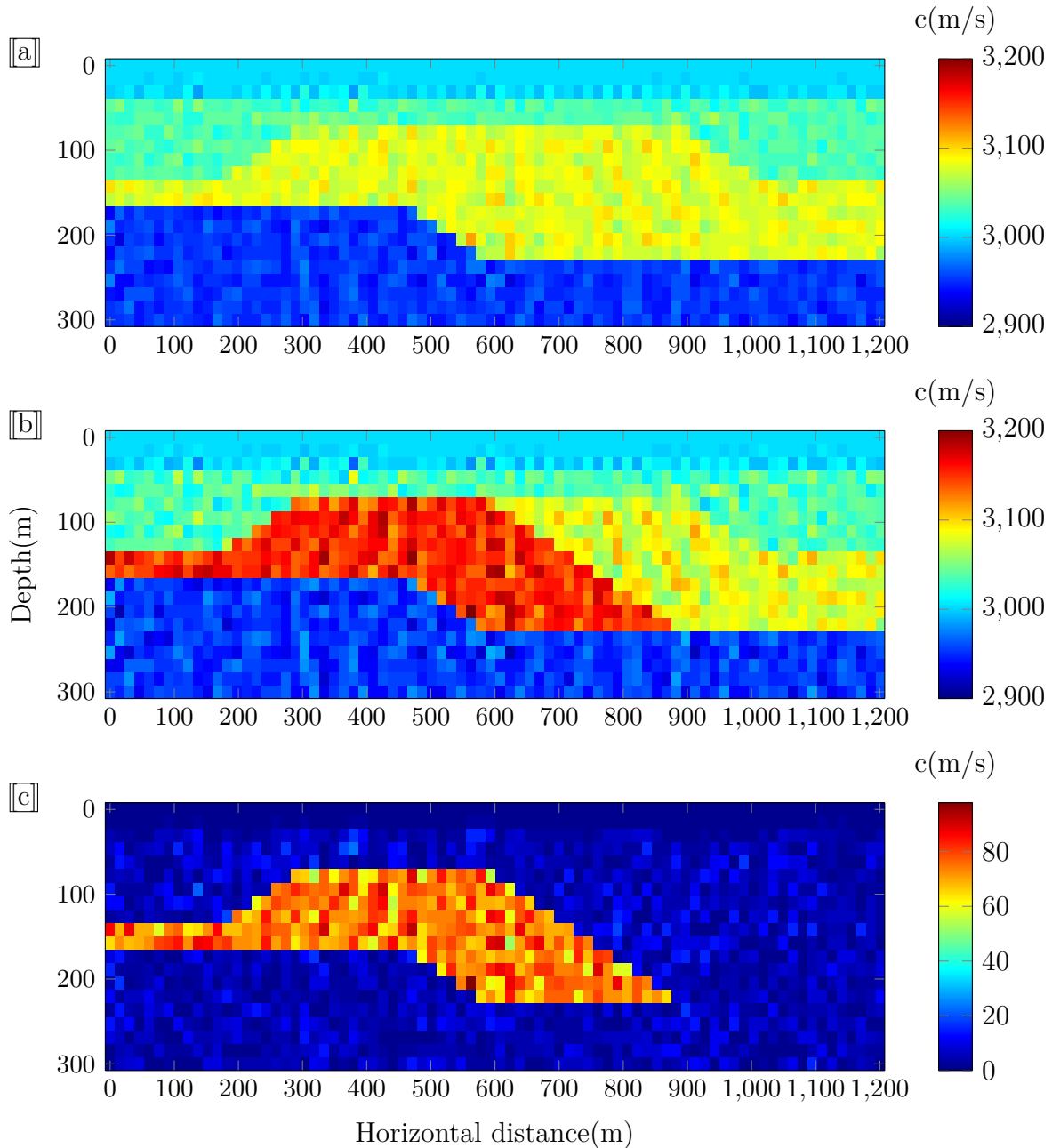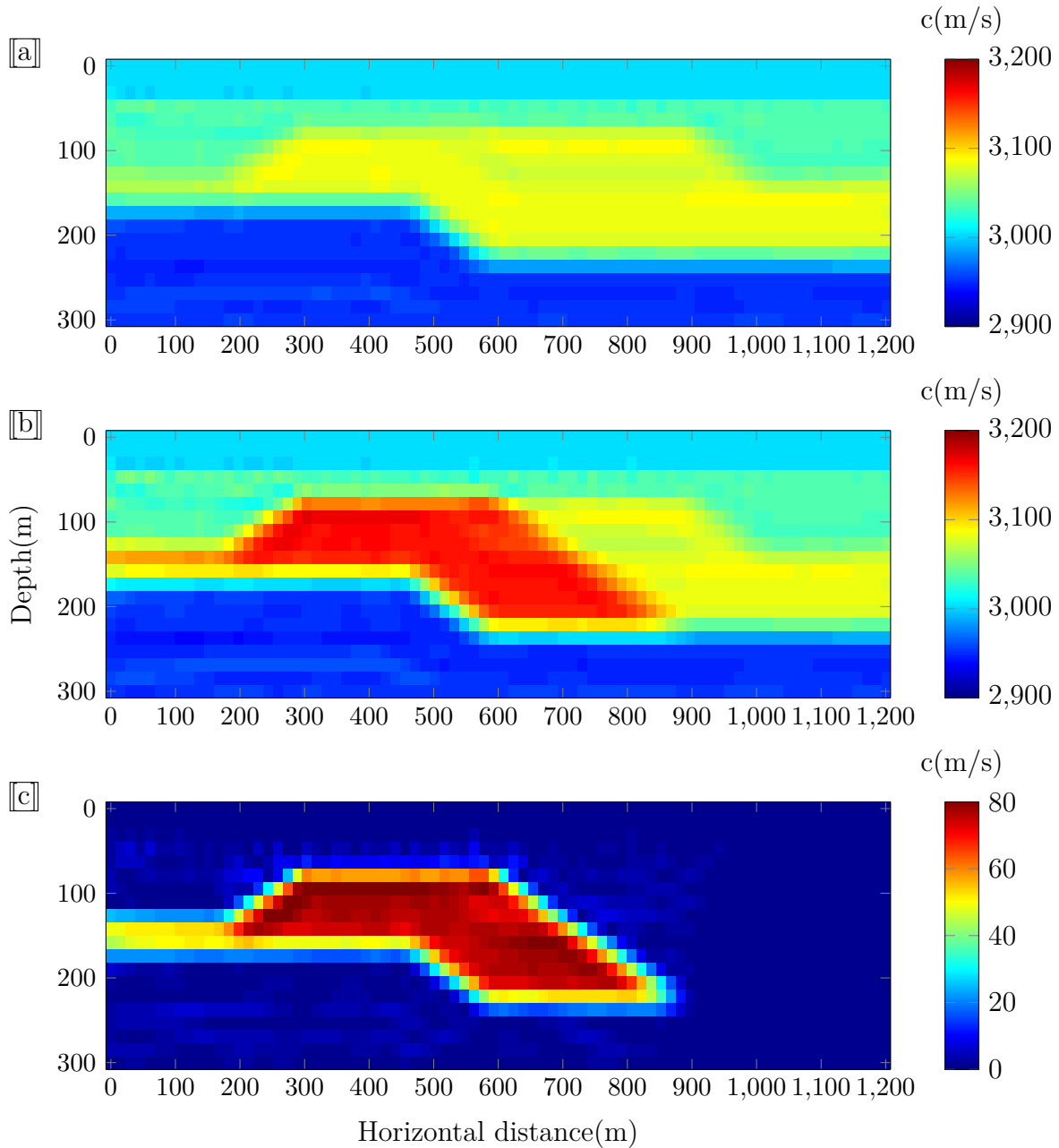
Figure 4.11: Born inversion results of the noise-free data for model 1 in Figure 4.4: (a) the baseline inversion result; (b) the monitoring inversion result; (c) time-lapse difference obtained by the sequential approach (subtracting the recovered baseline model from the recovered monitor model). The results were obtained using a scheme that inverts eight frequencies sequentially referred to, in the text,as the frequency-hopping method. The signal to noise ratio is 6 dB.
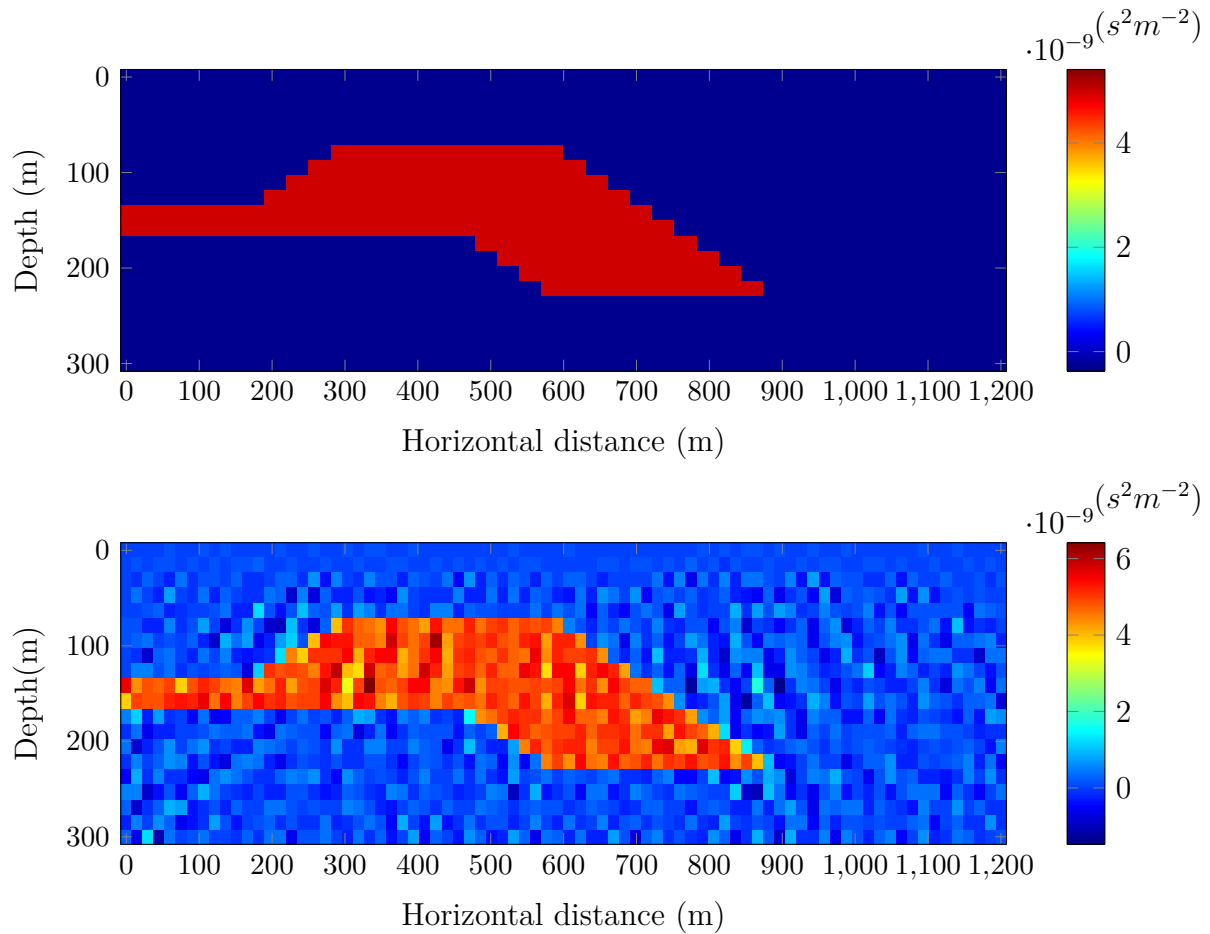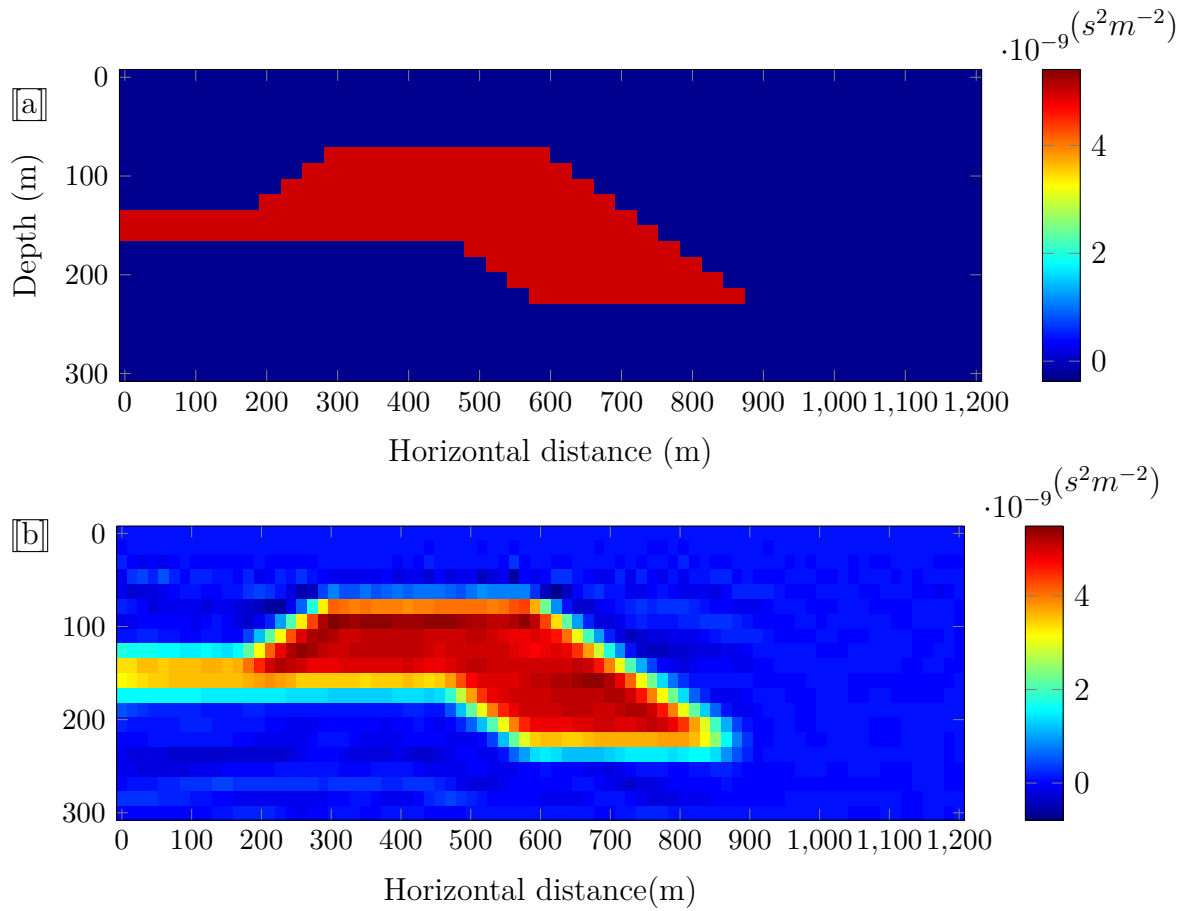
Figure 4.12: Born inversion results of the noise-free data for model 1 in Figure 4.4: (a) True time-lapse model showing the square of slowness change. (b) Inverted time-lapse difference using the differential approach. The results were obtained using a scheme that inverts eight frequencies sequentially referred to, in the text, as the frequency-hopping method. The signal to noise ratio is 6 dB.
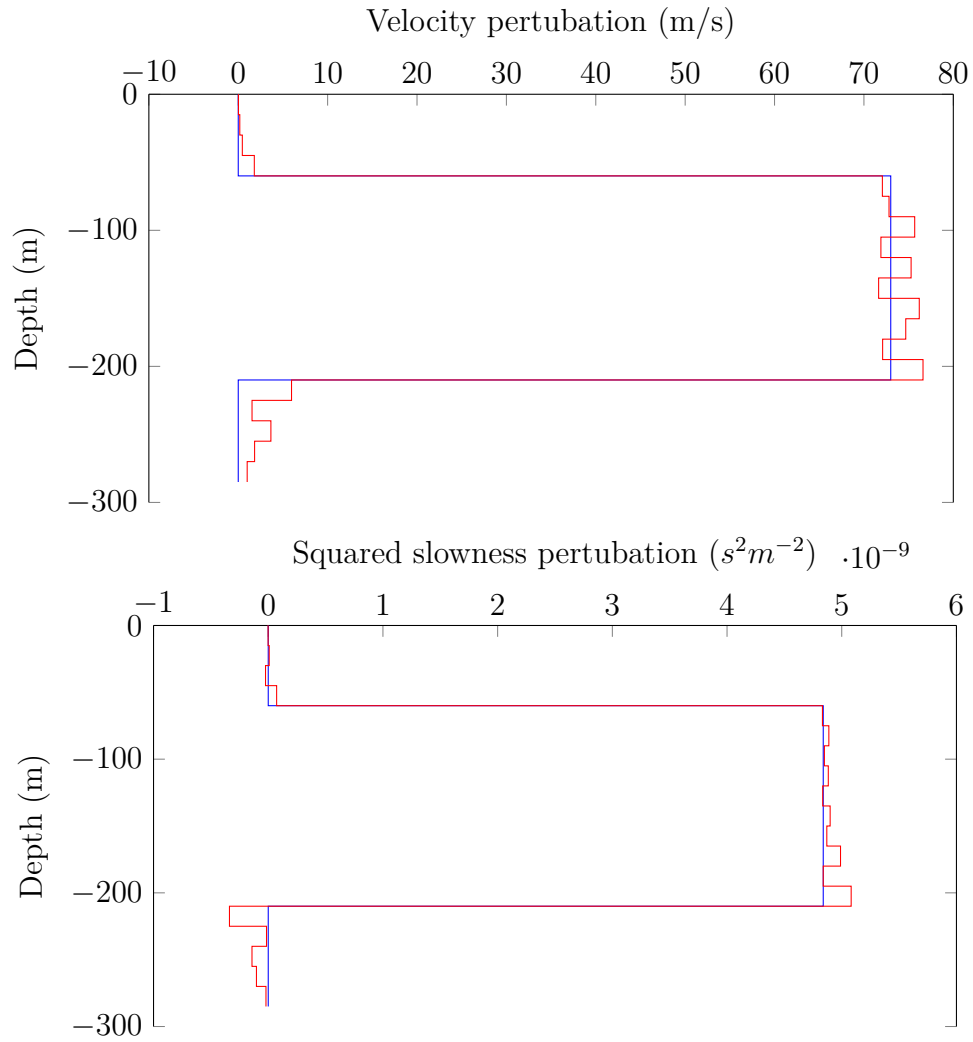
Figure 4.13: A vertical profile of Figure 4.4(c) at the horizontal position of 600 m. The blue solid lines are the true velocity and squared slowness changes and the red solid lines are the inversion results of noise free data using sequential approach (upper figure) and differential approach (lower figure).
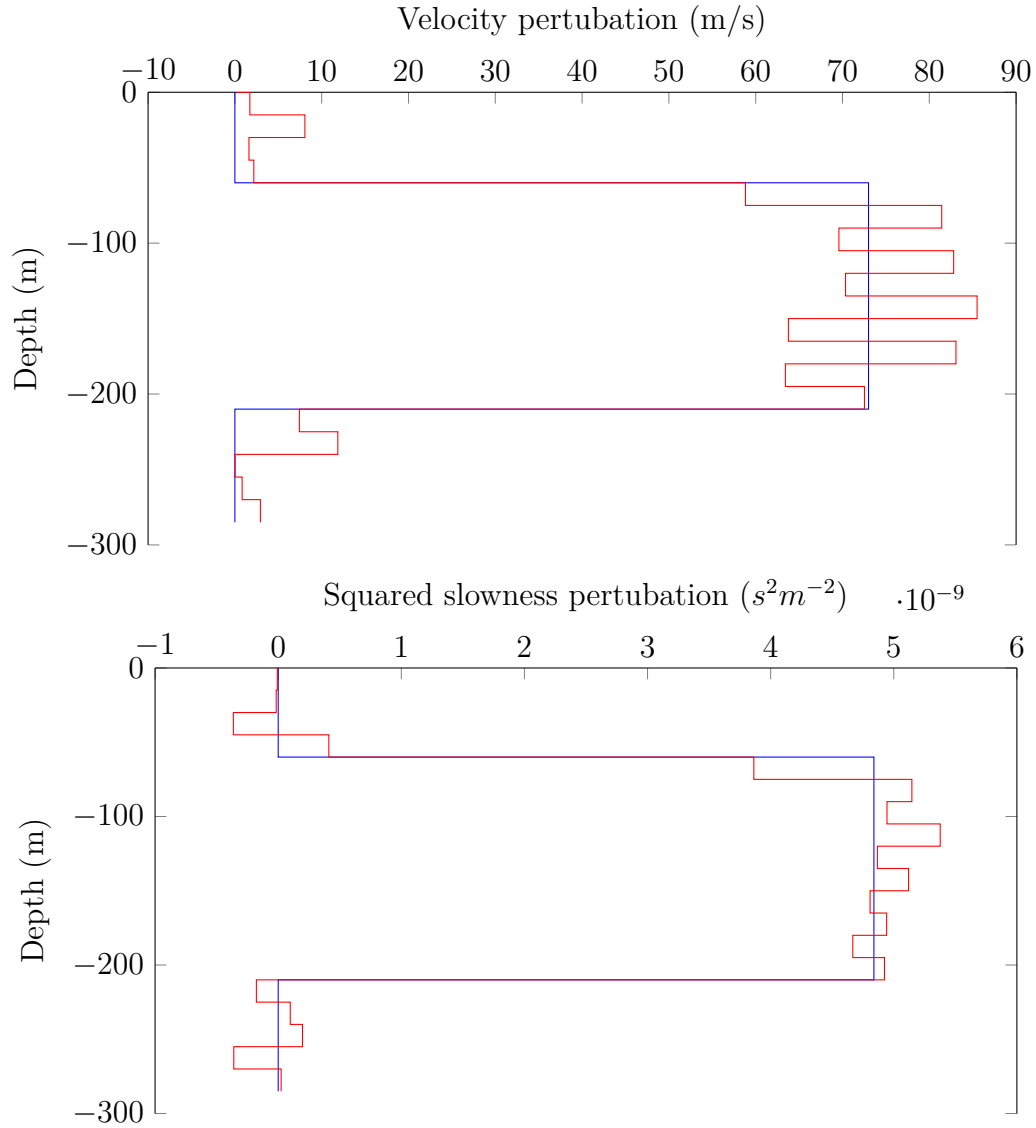
Figure 4.14: A vertical profile of Figure 4.4(c) at the horizontal position of 600 m. The blue solid lines are the true velocity and squared slowness changes and the red solid lines are the inversion results of noisy data using sequential approach (upper figure) and differential approach (lower figure).

Figure 4.15: Inversion of noise-free data using DBIT method for Model 2 in Figure 2.8 by sequential approach: (a) The reference model used as starting velocity model; (b) inversion result of the baseline model; (c) inversion result of the monitor model.

Figure 4.16: Inversion of noise-free data using DBIT method for Model 2 in Figure 2.8: (a) the true time-lapse model; (b) inversion result of change in P-wave velocity using sequential approach (simple subtraction of the independent inversion results of baseline and monitor surveys).

Figure 4.17: Inversion of noisy data using DBIT method for Model 2 in Figure 2.8 by sequential approach: (a) The reference model used as starting velocity model; (b) inversion result of the baseline model; (c) inversion result of the monitor model. The signal to noise ratio is 26 dB.

Figure 4.18: Inversion of noisy data using DBIT method for Model 2 in Figure 2.8: (a) the true time-lapse model; (b) inversion result of change in P-wave velocity using sequential approach (simple subtraction of the independent inversion results of baseline and monitor surveys). The signal to noise ratio is 20 dB.
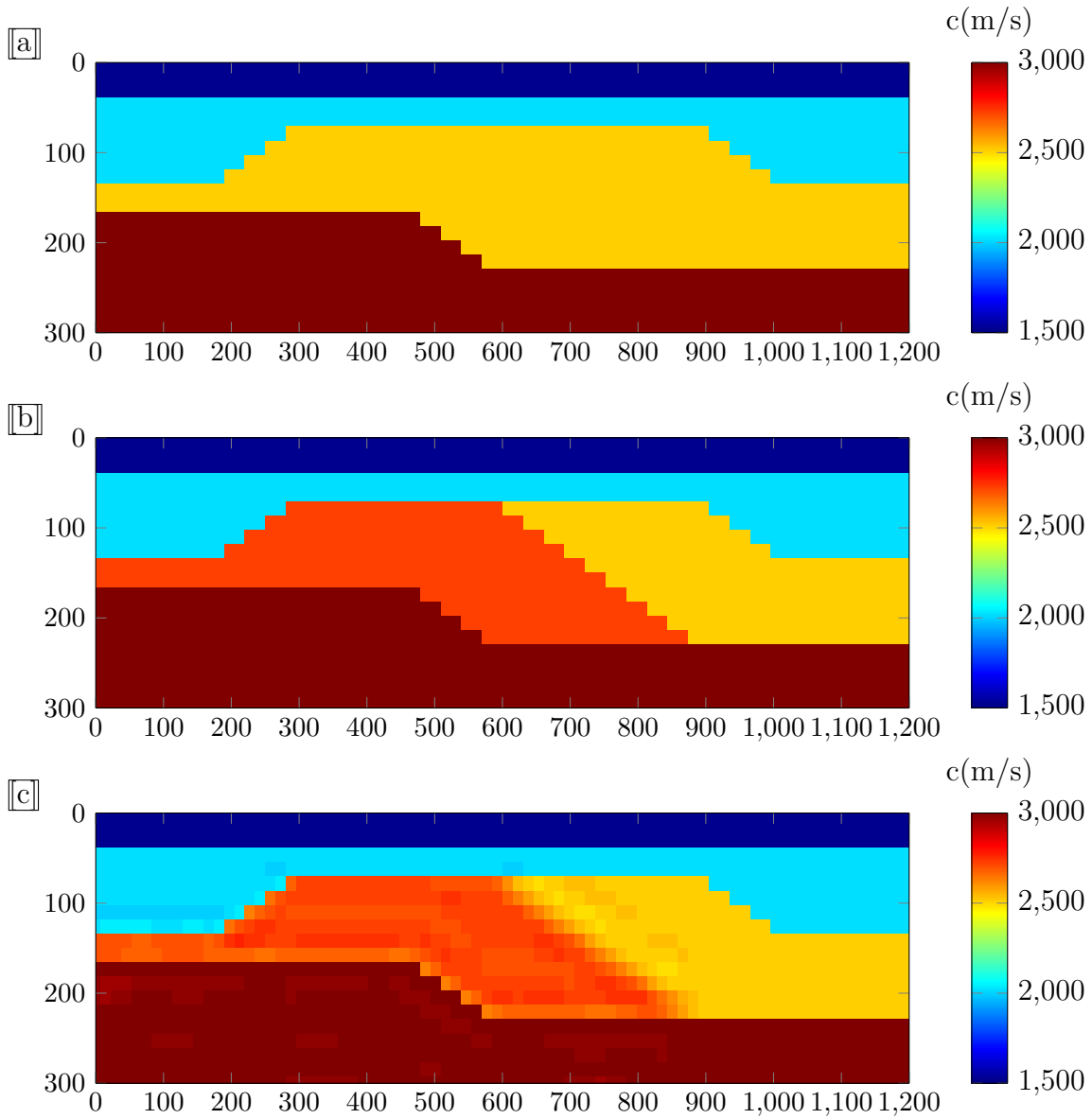
Figure 4.19: Inversion of noise-free data using DBIT method for Model 2 by differential approach: (a) The true baseline model used as reference (starting) velocity model; (b) The true monitor model; (c) The recovered monitor velocity model.
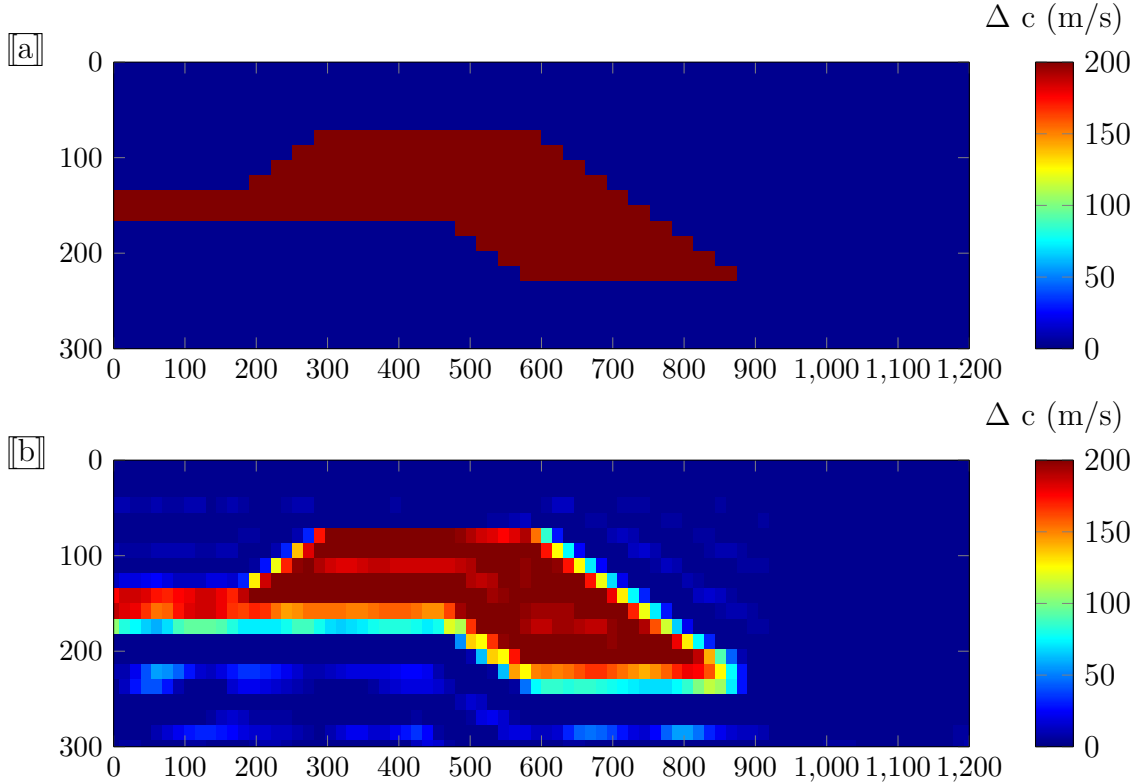
Figure 4.20: Inversion of noise-free data using DBIT method for Model 2: (a) the true time-lapse model; (b) inversion result of change in P-wave velocity by differential approach.
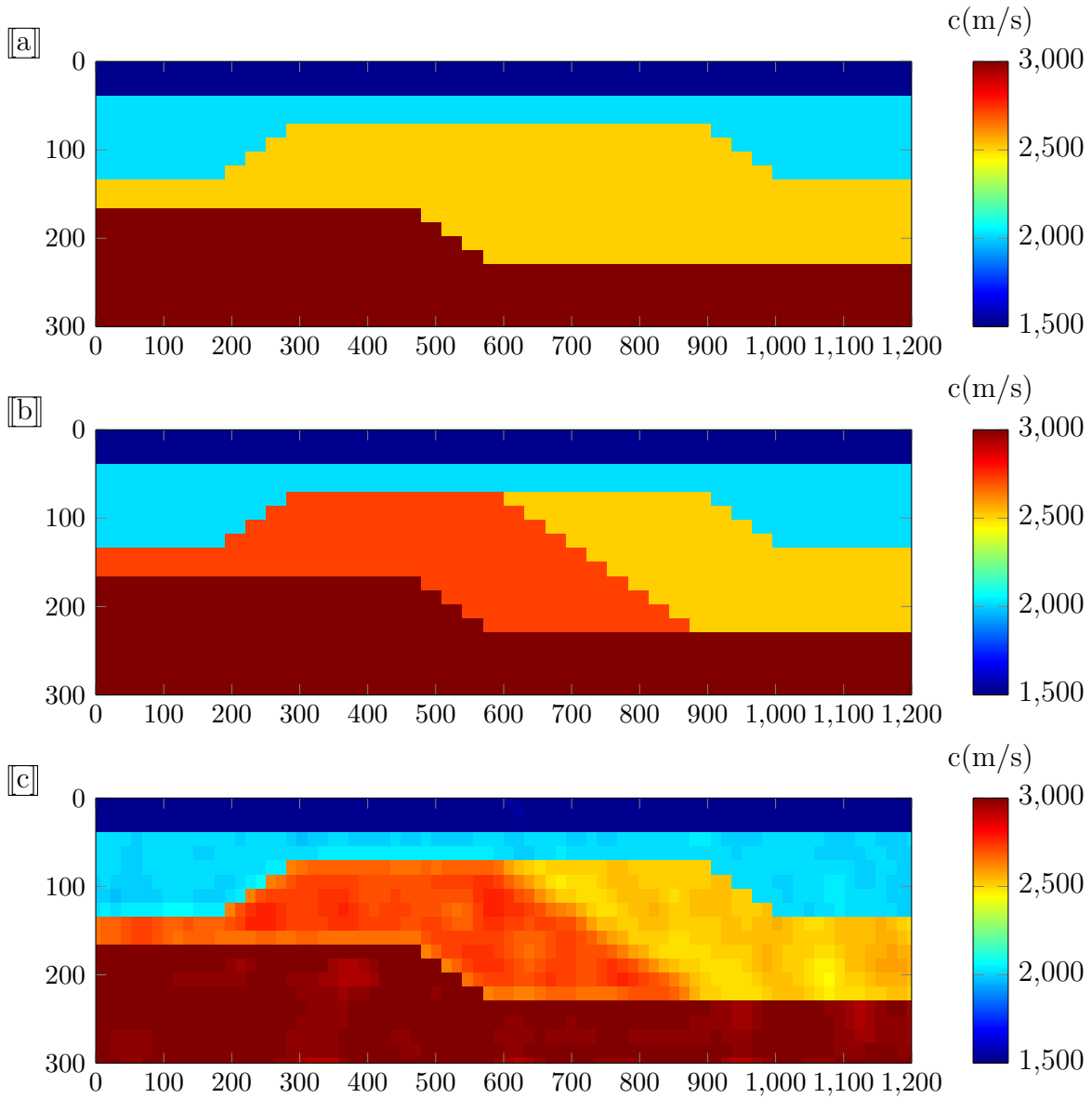
Figure 4.21: Inversion of noisy data using DBIT method for Model 2 by differential approach: (a) The true baseline model used as prior velocity model for inversion of noisy data; (b) The true monitor model; (c) The recovered monitor model. The signal to noise ratio is 26 dB.
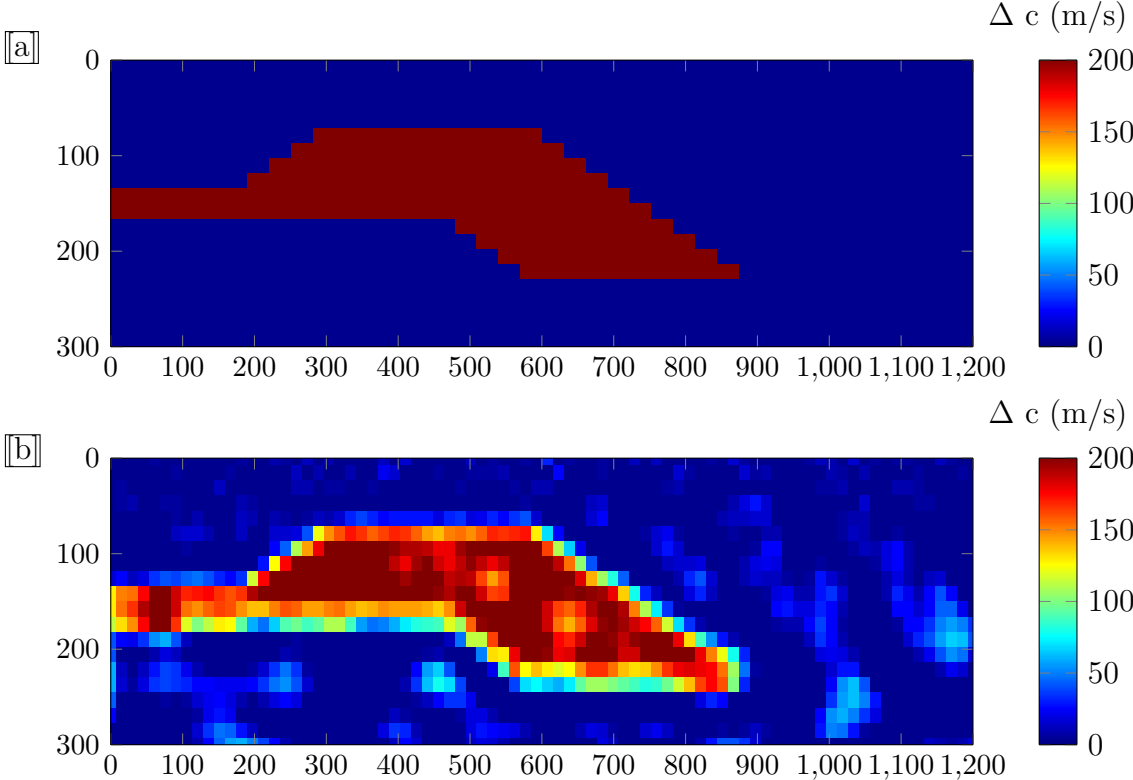
Figure 4.22: Inversion of noisy data using DBIT method for Model 2: (a) The true time-lapse change of P-wave velocity (time-lapse model). (b) inversion result of change in P-wave velocity by differential approach. The signal to noise ratio is 26 dB.
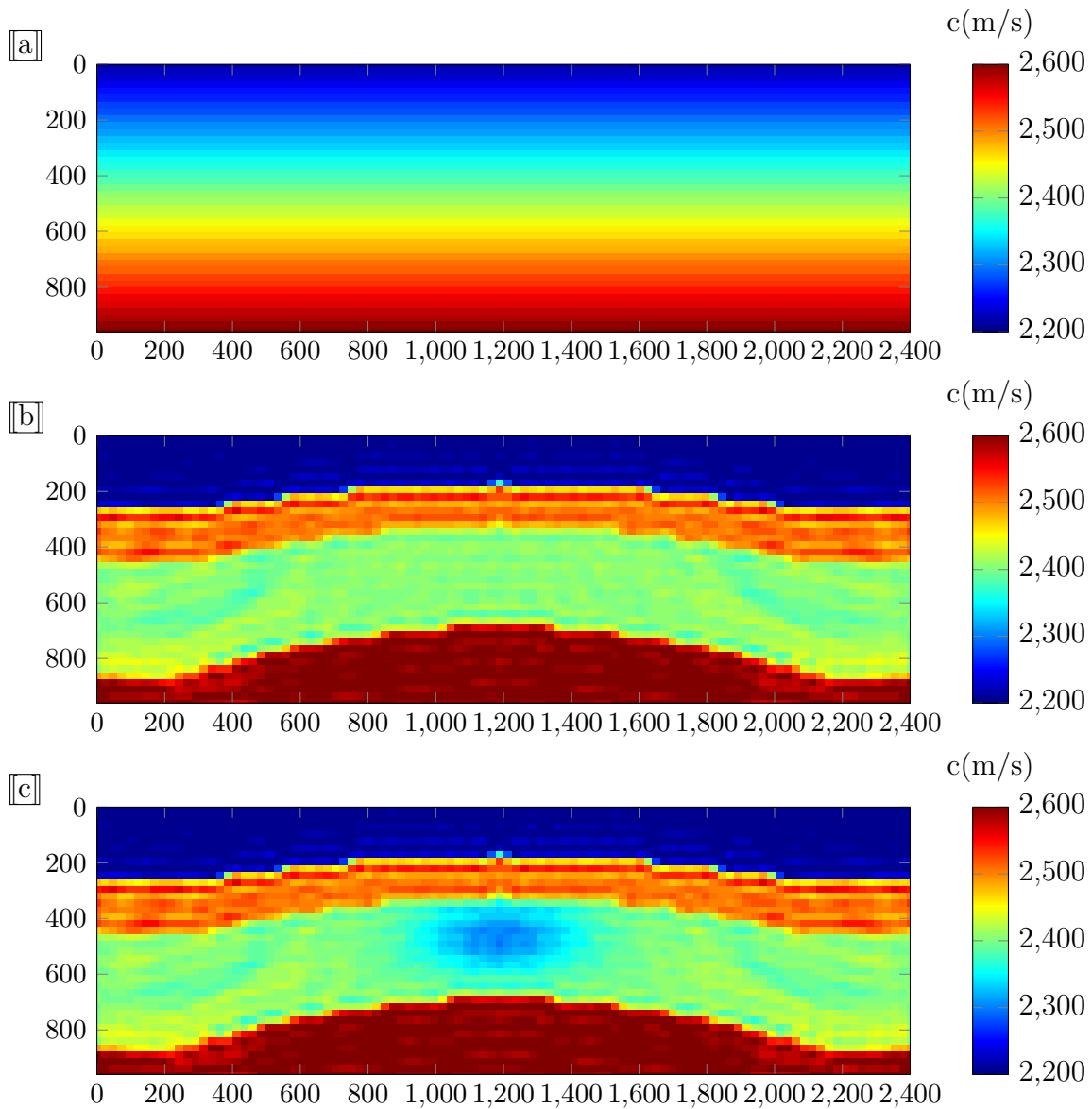
Figure 4.23: Inversion of noise-free data using DBIT method for Model 3 in Figure 2.13 by sequential approach: (a) The reference model used as starting velocity model; (b) inversion result of the baseline model; (c) inversion result of the monitor model.
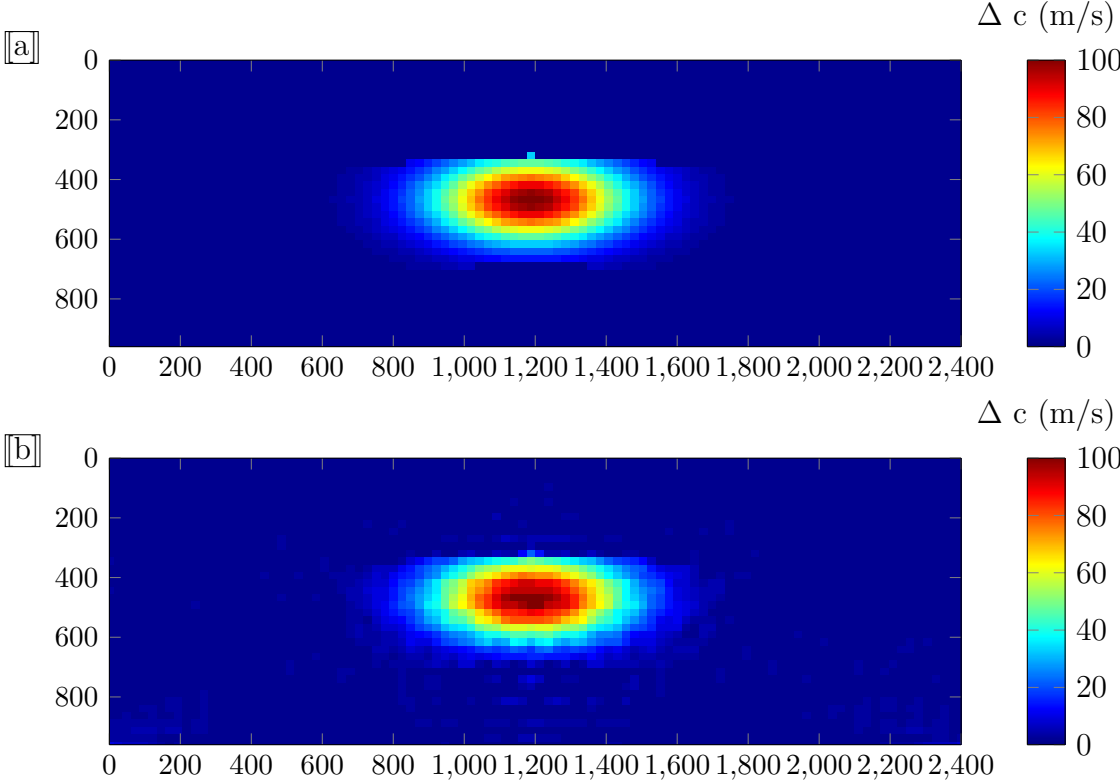
Figure 4.24: Inversion of noise-free data using DBIT method for Model 3 in Figure 2.13: (a) the true time-lapse model; (b) inversion result of change in P-wave velocity using sequential approach (simple subtraction of the independent inversion results of baseline and monitor surveys).
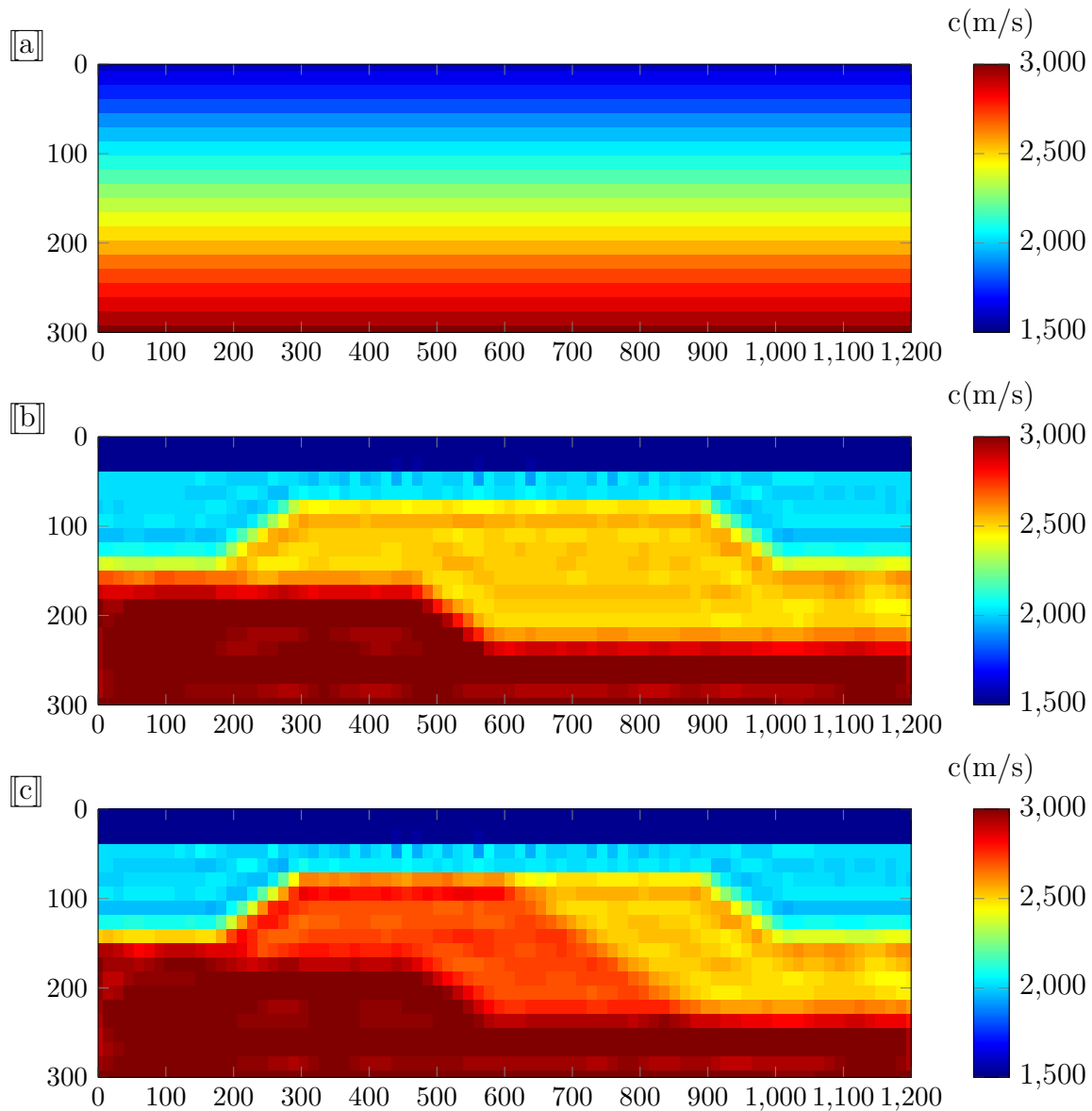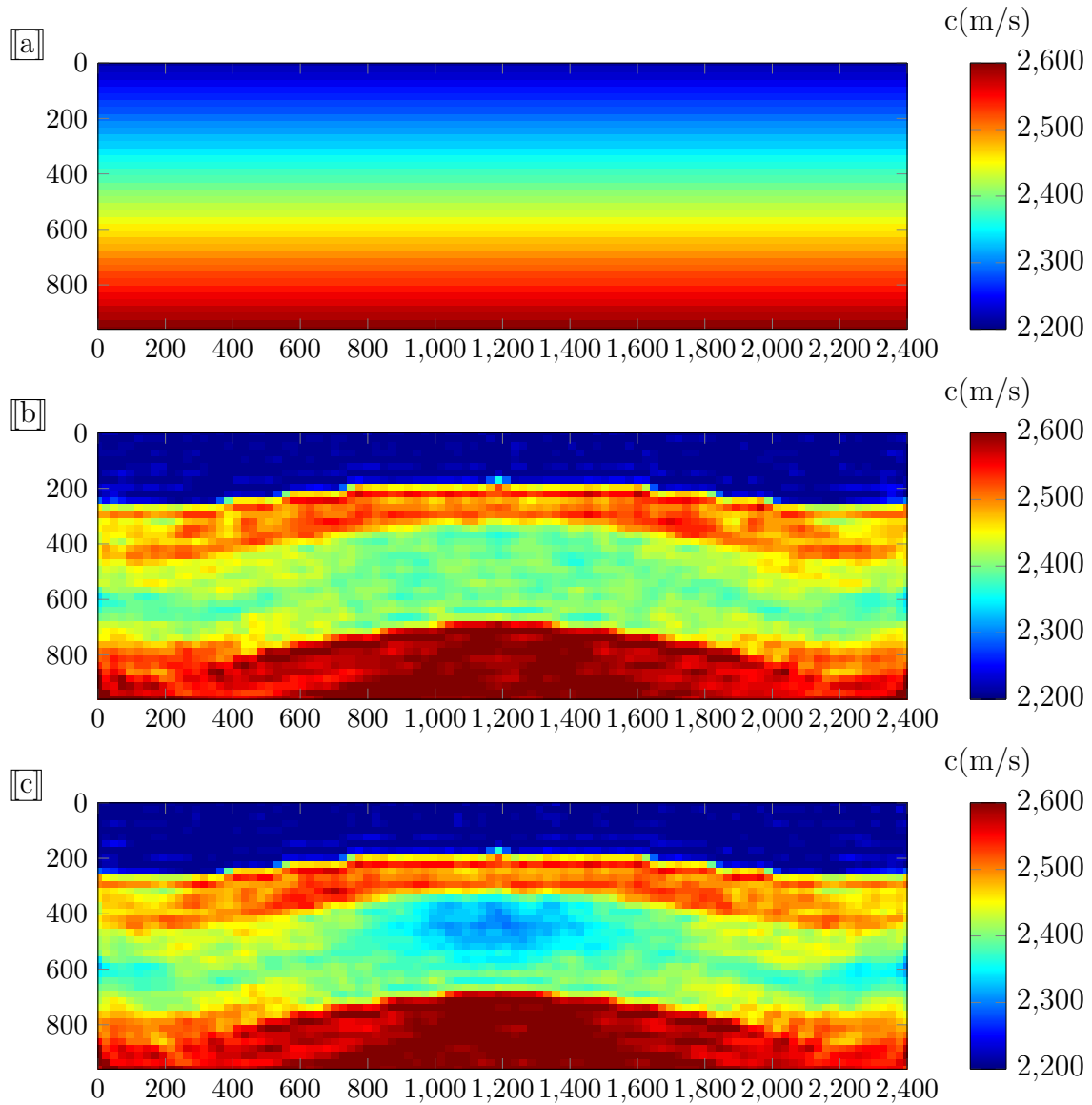
Figure 4.25: Inversion of noisy data using DBIT method for Model 3 in Figure 2.13 by sequential approach: (a) The reference model used as starting velocity model; (b) inversion result of the baseline model; (c) inversion result of the monitor model. The signal to noise ratio is 26 dB.
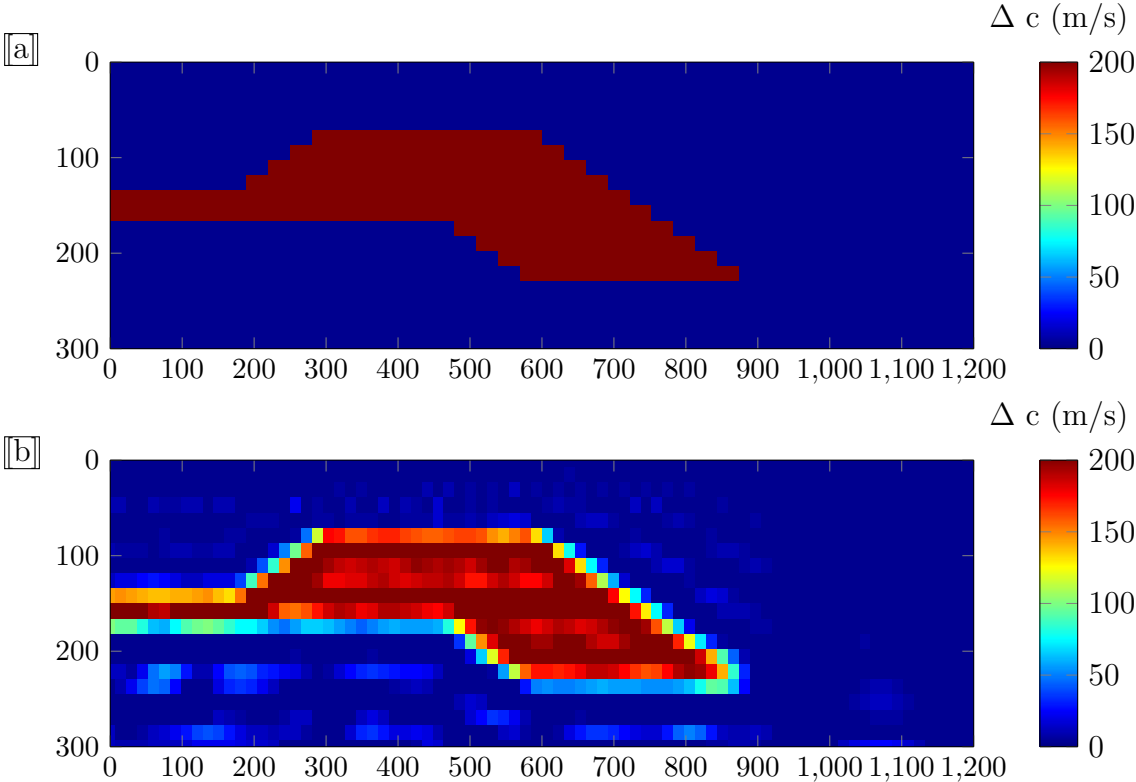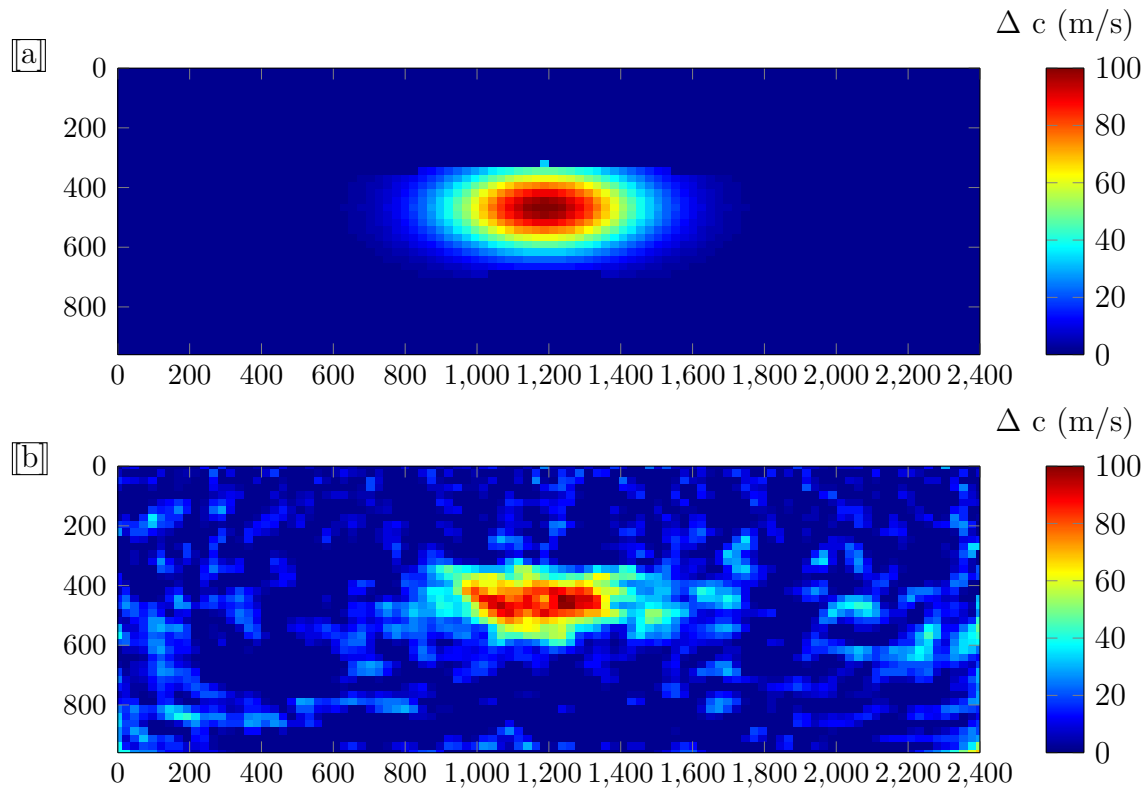
Figure 4.26: Inversion of noisy data using DBIT method for Model 3 in Figure 2.13: (a) the true time-lapse model; (b) inversion result of change in P-wave velocity using sequential approach (simple subtraction of the independent inversion results of baseline and monitor surveys. The signal to noise ratio is 20 dB.
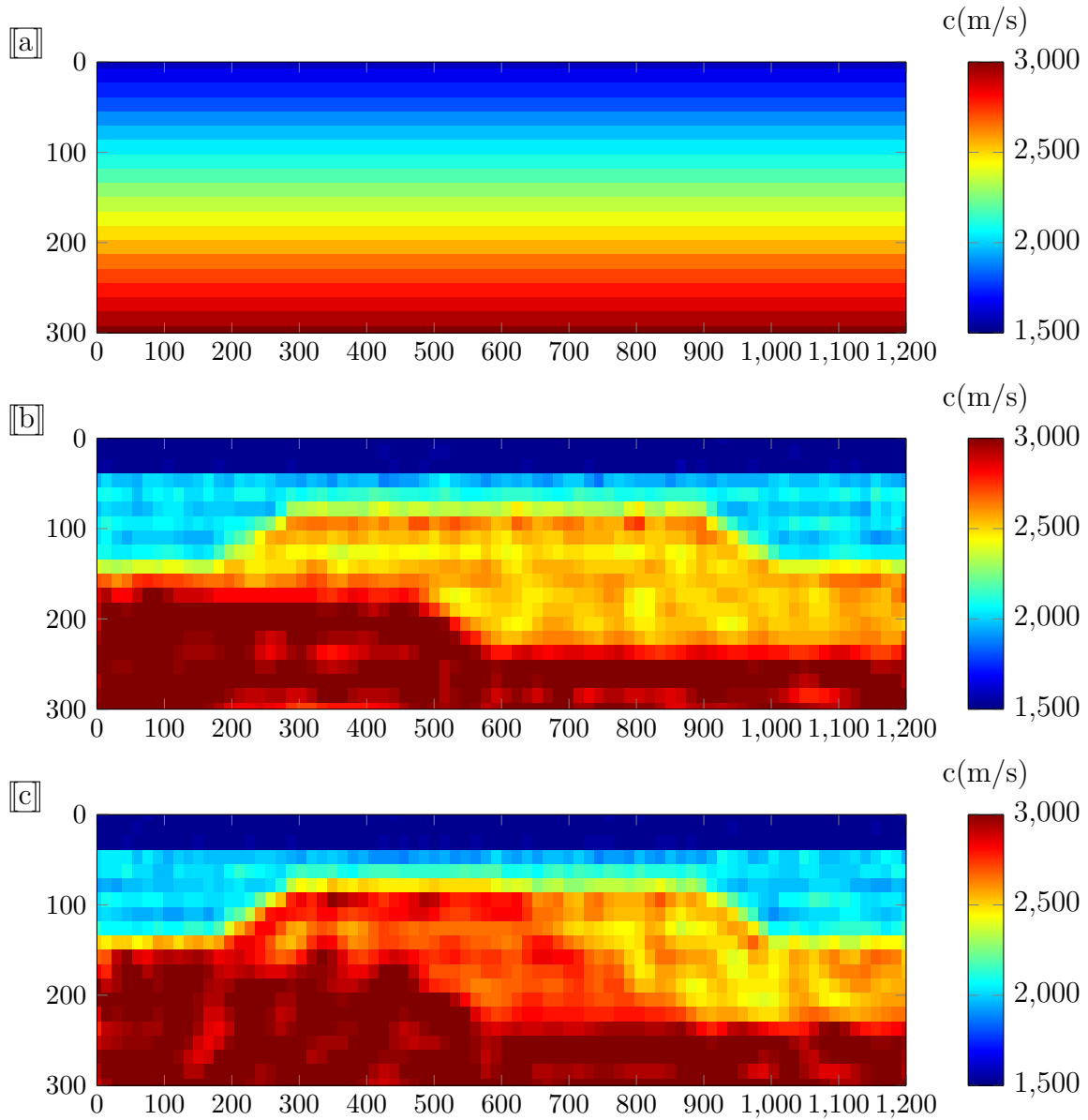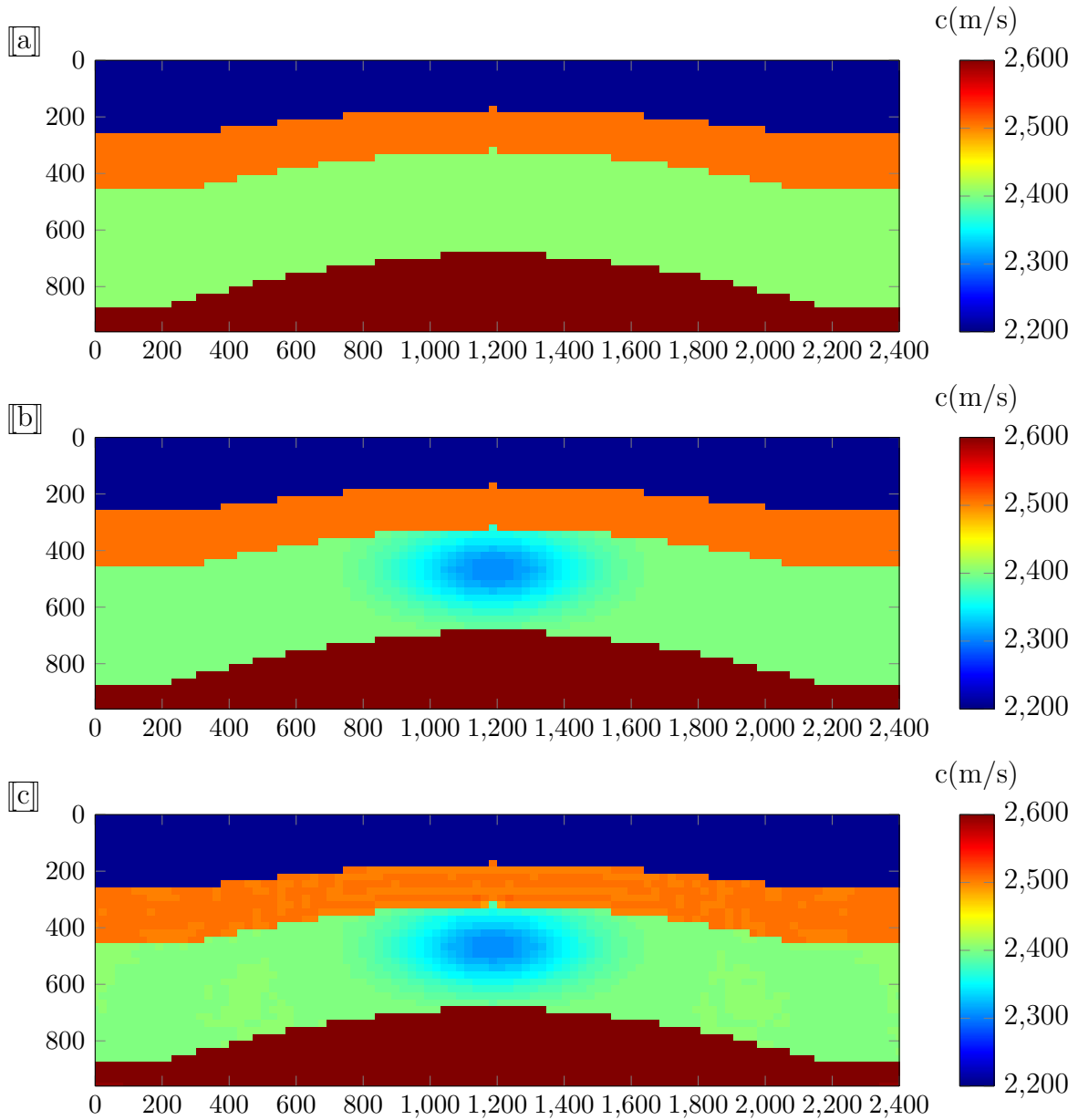
Figure 4.27: Inversion of noise-free data using DBIT method for Model 3: (a) The true baseline model used as prior velocity model; (b) The true monitor model after injection; (c) The recovered monitor velocity model in the differential approach.
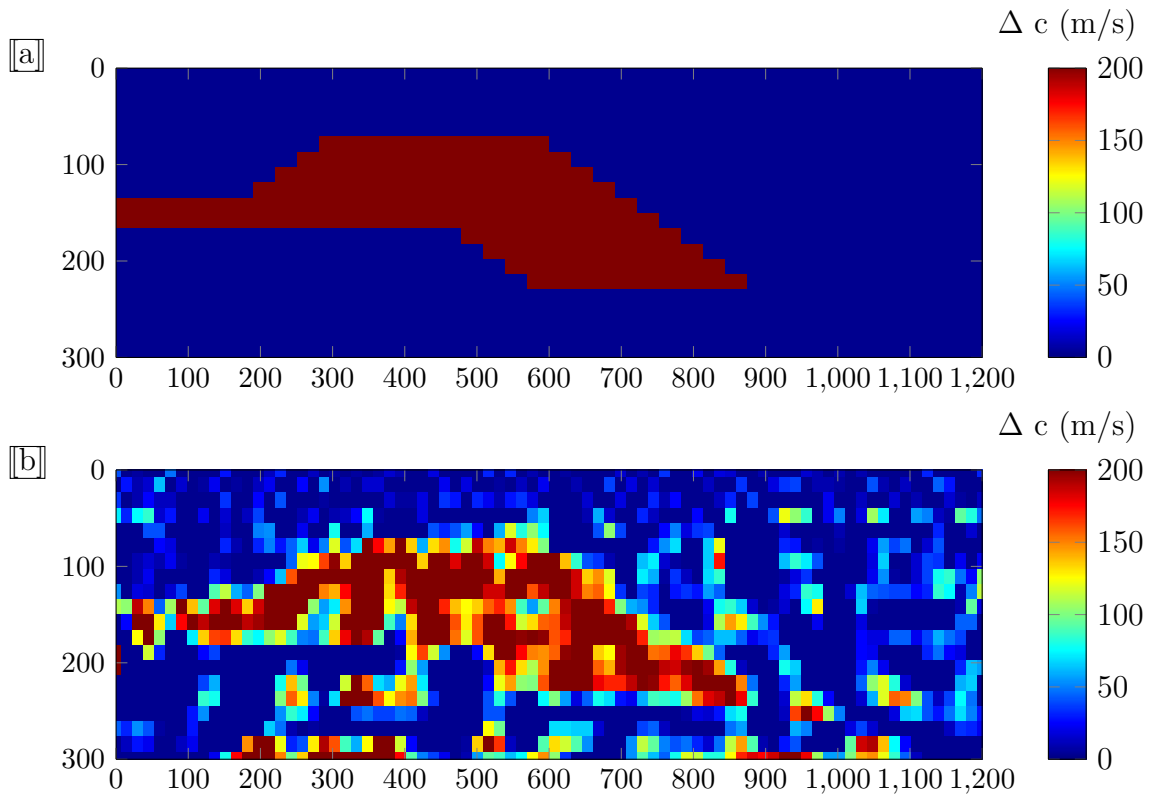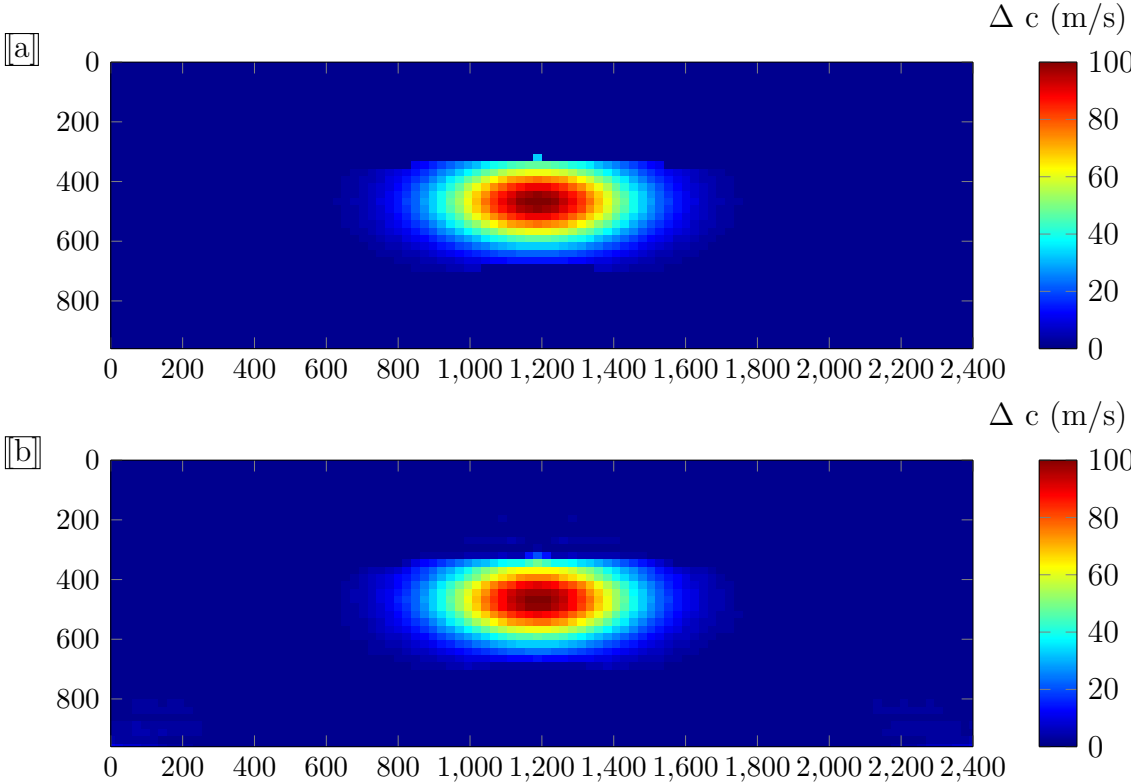
Figure 4.28: Inversion of noise-free data using DBIT method for Model 3: (a) the true time-lapse model; (b) inversion result of change in P-wave velocity using differential approach.
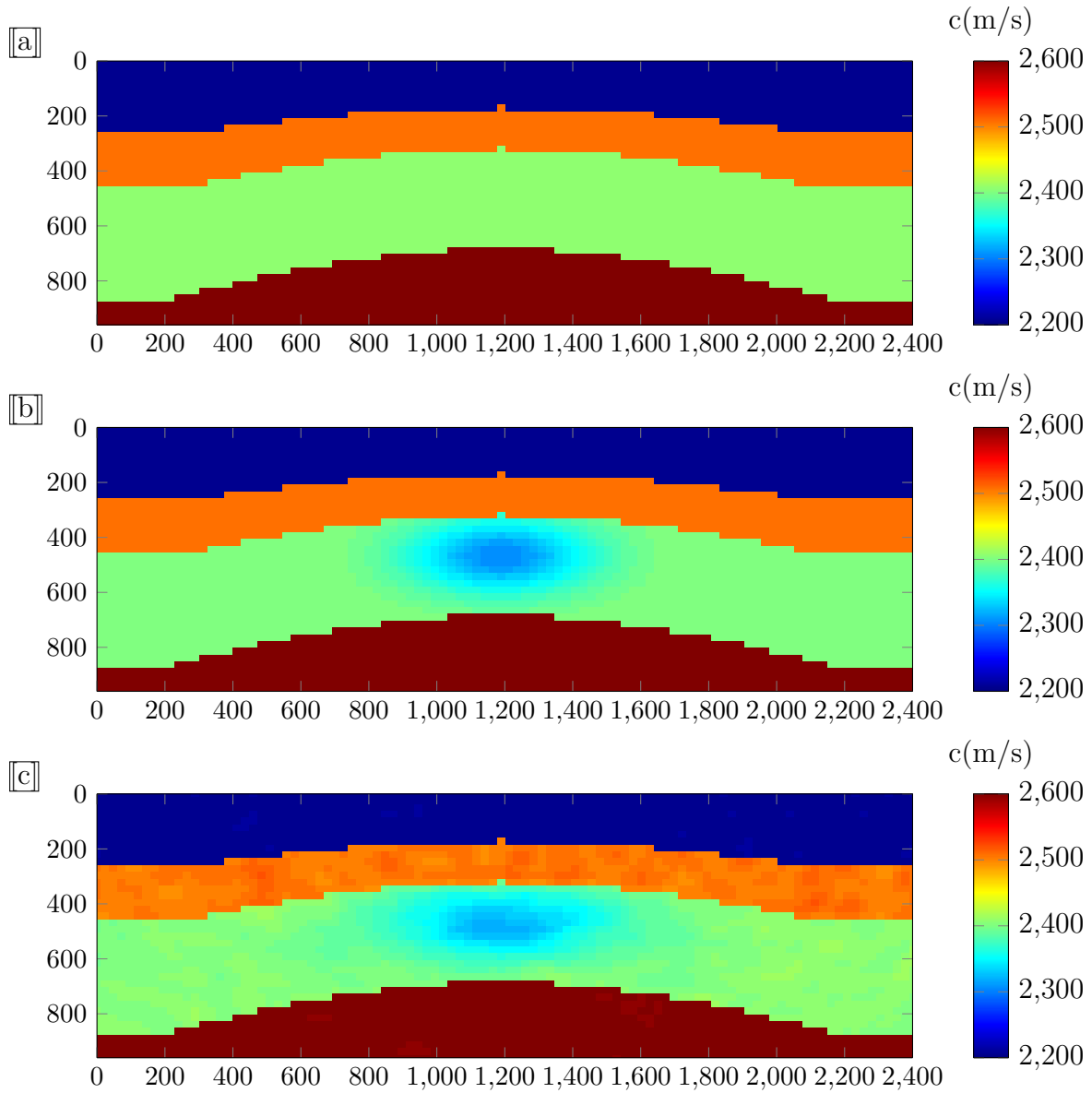
Figure 4.29: Inversion of noisy data using DBIT method for Model 3: (a) The true baseline model used as prior velocity model for inversion of noisy data; (b)The true monitor model after injection; (c) recovered monitor model in the differential approach. The signal to noise ratio is 20 dB.
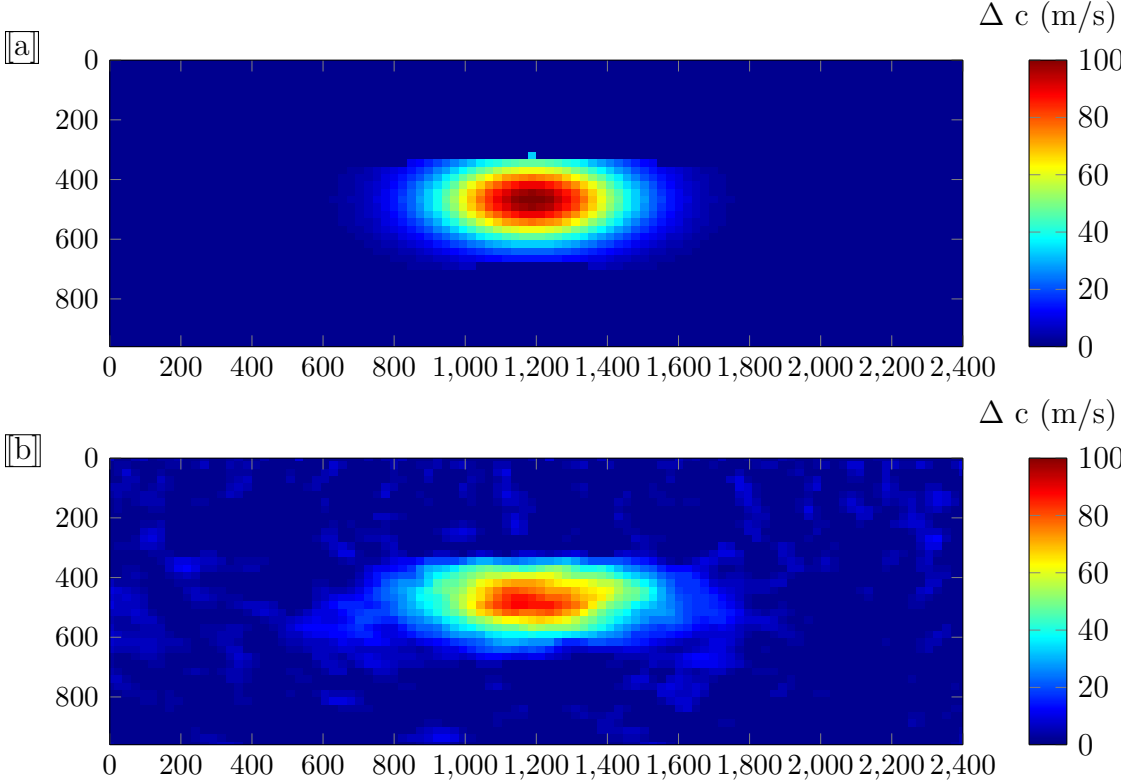
Figure 4.30: Inversion of noisy data using DBIT method for Model 3: (a) The true time-lapse change of P-wave velocity (time-lapse model). (b) inversion result of change in P-wave velocity using differential approach. The signal to noise ratio is 20 dB.

# Chapter 5

# Conclusions and Further Work

In the introduction, we highlighted the value of time-lapse data modelling and expressed the hope that the work in this thesis could give us new insights in the use of approximations based on scattering theory for modelling and inversion of time-lapse data. In this final chapter, we will conclude by describing the progress made towards our thesis objectives in terms of using the first order scattering approaches to solve time-lapse problems in a range of domains. We will also recommend some further research directions that could provide the next steps along the path of Born theory to address more practical and realistic scenarios involving time-lapse seismic.

## 5.1   Conclusions

The aim of this thesis has been to investigate the seismic forward and inverse problems for time-lapse data using approximations of scattering approaches. In Chapter 1, we gave an overview of these problems and also presented an overview of the thesis. In Chapter 2, we reviewed the theory of seismic forward modelling and derived the Born approximation and distorted-Born approximation formulations for a constant density acoustic wave equation. We performed forward modelling experiments and generated synthetic seismograms for three different models by considering the traditional Born which utilises a homogeneous background medium and distorted Born approximation that utilises a general heterogeneous background

media. In Chapter 3, we reviewed the theory of geophysical inversion and gave an in-depth treatment to only the method of least squares matrix inversion and Tikhnov regularization. We implemented the theory by using a toy example to get a clear understanding of the underlying principles before applying the methods to more complex cases in the chapter that follows. In Chapter 4, the inverse problem for time-lapse seismic data was addressed using Born linearised inversion and the distorted Born iterative T-matrix inversion (DBIT) method which is a non-linear inversion approach. Both inversion methods were used with a Tikhonov regularization technique. Two different time-lapse inversion strategies were used to characterise time-lapse velocity changes.

The forward modelling numerical results suggest that the performance of the Born approximation in predicting time-lapse seismograms is limited to applications involving small velocity contrasts as well as small volume contrasts. On the other hand, the distorted-Born employed in the study gave accurate results even in cases where the spatial extension of the reservoir in terms of thickness is large and the velocity contrasts are big. This is clearly seen in all numerical experiments presented, as the results of the distorted-Born approximation agree excellently with the exact T-matrix solution. A heterogeneous background medium which is close to the actual medium is therefore required to estimate accurately the travel times and amplitude of the rays which are essential for the computation of Green's function.

Waveform inversion based on linearized Born approximation recovers the time-lapse velocity models well both in shape and amplitude. The differential approach to waveform inversion which considers the data difference caused by changes in the monitoring region gives improved subsurface reconstructions of the time-lapse velocity changes. The inversion results obtained using the conventional sequential approach locates the approximate location of the reservoir but reconstructs the magnitudes of its velocity changes with more errors. The DBIT method produce good inversion results and was found to be very good even in time-lapse models involving relatively large velocity contrasts. The computational cost of the DBIT method is low and this gives good promise of this method for full waveform inversion. The resolution of the images are improved when the high frequencies components of the seismic data are included. Although we may define time-lapse variations as high-frequency details in

the model at the reservoir scale, going beyond certain frequency limits during inversion may lead to the creation of false events (Lecerf and Reiser, 2004).

In conclusion, our numerical examples demonstrate that the application of Born approximation with a heterogeneous background medium close to the actual medium is still relevant in modelling time-lapse seismograms. In addition, linearized waveform inversion has potential for recovering time-lapse velocity changes in the absence and presence of noise effects and can be a sufficient tool for seismic reservoir monitoring of geologic structures but within the limits of Born approximation. The DBIT method which considers a dynamic background media and a variational T-matrix approach may be very useful in seismic characterisation of petroleum reservoirs under production and may be more efficient in monitoring of $CO_2$ sequestration.

## 5.2   Suggestion for Further Work

A number of concerns must be addressed to allow for a detailed characterization of complex media and petroleum reservoirs in the modelling process. These concerns suggest a variety of research directions that need to be pursued to make Born theory feasible in modelling time-lapse data.

One such obvious direction is to extend the modelling to 3D. In this thesis, only numerical experiments based on 2D acoustic wave equation for constant density modelling are discussed. Ideally, it would be preferable to modify the algorithms to 3D modelling since the Earth is realistically three-dimensional.

Another important suggestion would be to consider a real media generalization based on the elastic wave equation (Appendix B) to allow for different levels of medium complexity. Our current work employed an acoustic approximation which may not be sufficient for many complex seismic imaging problems. Allowing elastic wave propagation improves the characterization of complex media and makes it possible to account for S-waves which carry important information about subsurface rocks and their pore fluids. In addition, different elastic wave effects such as anisotropy and attenuation can be dealt with in modelling.

While we assume that there is a change only in the velocity for the time-lapse problem,

this is not necessarily true. In the real world, seismic modelling depends on many factors that cannot be ignored. In order to obtain realistic results, important ingredients such as density variations, rock physics relations, stress conditions that affect overburden pressure, pore fluids, fractures, porosity and attenuation would be taken into consideration and applied in the modelling formulation.

Finally, in the sense of time-lapse seismic inversion, it could be interesting to consider more robust non-linear inversion methods. The DBIT method could be further developed for an elastodynamics case and its performance improved for large 3D models. An investigation of different approaches such as joint inversion would be worthwhile in order to consider practical aspects of waveform inversion. The fundamental FWI is quite promising for time-lapse seismics (e.g., Asnaashari et al., 2015; Raknes and Arntsen, 2014) and as computers increase in processing power, future applications of waveform inversion to large 3D models is essential.

## 5.3 Summary

In summary, we have investigated the modelling of acoustic wave propagation in 2D using scattering approaches in the frequency domain for time-lapse seismic problems. We applied Born inversion and DBIT method to the modelled data. The developments were done in MATLAB. We have demonstrated that Born approximation based inversion can sufficiently image the time-lapse velocity changes for small model contrasts. The distorted-Born approximation with its corresponding DBIT inversion method introduced later improves the validity range of Born approximation and Born inversion significantly allowing for accurate results for the different seismic imaging problems considered in our work.

# Appendix A

# T-matrix approach

The T-matrix (or transition operator) approach whose underlying principles follow from the quantum mechanical potential scattering theory can be used to approximate or obtain an exact solution of the Lippmann-Schwinger integral equation. The T-matrix does not depend on the source-receiver configuration and contains the whole Born Neumann series (Jakobsen, 2012) when it is not used in approximation form. The independence on source-receiver geometry is useful especially in applications involving many sources and receiver positions. The full forward numerical solution of the Lippmann-Schwinger equation using the T-matrix only requires the knowledge about the scattering potential and the Green's function for the reference medium. However, the exact T-matrix solution which allows for arbitrary contrast volumes and includes all the effects of scattering is computationally expensive but is convenient especially in cases of time-lapse seismics when the models are not too large (Jakobsen, 2012). In what follows we derive a T-matrix representation of a full numerical solution of the Lippmann-Schwinger equation which we used for comparing our numerical results.

## A.1 Derivation of T-matrix formulation

In the quantum mechanical potential scattering approach (e.g., Pike and Sabatier, 2002; Jakobsen, 2012; Jakobsen and Ursin, 2015), the so-called T-matrix (or transitional operator)

**T** is defined by the relation

$$\mathbf{V}\mathbf{P}_V = \mathbf{T}\mathbf{P}_V^{(0)}. \tag{A-1}$$

where $\mathbf{P}_V$ and $\mathbf{P}_V^{(0)}$ represent the wavefield in actual medium and reference medium respectively for a discretized scattering volume $V$ and $\mathbf{V}$ is a diagonal matrix with the scattering potential for a heterogeneous model. Combining the above relation with the Lippmann-Schwinger equation (2.43), we obtain

$$\mathbf{P}_V = \mathbf{P}_V^{(0)} + \bar{\mathbf{G}}_{VV}^{(0)}\mathbf{T}\mathbf{P}_V^{(0)}. \tag{A-2}$$

Multiplying Equation (A-2) with **V** from the left, we obtain

$$\mathbf{V}\mathbf{P}_V = \mathbf{V}\mathbf{P}_V^{(0)} + \mathbf{V}\bar{\mathbf{G}}_{VV}^{(0)}\mathbf{T}\mathbf{P}_V^{(0)}. \tag{A-3}$$

Using the definition for the relation in (A-1) together with the above equation (A-3), we obtain

$$\mathbf{T}\mathbf{P}_V^{(0)} = \mathbf{V}\mathbf{P}_V^{(0)} + \mathbf{V}\bar{\mathbf{G}}_{VV}^{(0)}\mathbf{T}\mathbf{P}_V^{(0)}. \tag{A-4}$$

Since $\mathbf{P}_V^{(0)}$ is arbitrary, it follows from (A-4) that

$$\mathbf{T} = \mathbf{V} + \mathbf{V}\bar{\mathbf{G}}_{VV}^{(0)}\mathbf{T}. \tag{A-5}$$

Equation (A-5) is often called the Lippmann-Schwinger equation for the T-matrix (Jakobsen, 2012) and the fundamental definition of the T-matrix used for the numerical computations is written as

$$\mathbf{T} = (\mathbf{I} - \mathbf{V}\bar{\mathbf{G}}_{VV}^{(0)})^{-1}\mathbf{V}. \tag{A-6}$$

The equation (A-6) represents a full numerical solution of the Lippmann-Schwinger equation. It calculates the T-matrix by matrix inversion and is applicable regardless of the strength of the scattering potential (Jakobsen and Ursin, 2015). The formulation above allows us to use the T-matrix to compute for wavefields in the actual medium for a given scattering potential and background (reference) medium.

# Appendix B

# Elastic wave scattering

In this thesis, an acoustic approximation was used to implement the Born approximation and the distorted-Born approximation to simplify the mathematical formulation and reduce the computational burden of both the forward and inverse modelling problems. Although results based on acoustic approximation are considered accurate and may be used to test new algorithms for many seismic problems, a real media generalization based on the elastic wave equation is needed to allow for different levels of medium complexity. Allowing elastic wave propagation improves the characterization of complex media and makes it possible to account for S-waves which carry important information about subsurface rocks and their pore fluids. In addition, different elastic wave effects such as anisotropy and attenuation can be dealt with in modelling without exhibiting an ambiguity (e.g, Eaton and Stewart, 1994; Richard L. Gibson, 2008; Sato et al., 2012). As a potential future research consideration of the Born approximation and distorted-Born approximation, we include below a derivation of the integral equation formulation of scattering (Lippmann-Schwinger equation) assuming a general elastic case where the earth model is anisotropic. We then follow the same procedure for acoustic media and the treatment given in Pike and Sabatier (2002) and Červenỳ (2001) to derive the Born approximation corresponding to the general elastic case.

112

## B.1 The Lippmann-Schwinger Equation for Elastic Waves

If we assume the displacement **u** due to a source **f** in a medium of density $\rho$ and general elasticity tensor $C_{ijkl}$, the elastic wave equation in shorthand notation in the frequency domain corresponds to (Pike and Sabatier, 2002):

$$\mathbf{Lu} = \mathbf{f} \tag{B-1}$$

where the operator **L** is defined (using index notation) by

$$L_{ij} = \rho\omega^2\delta_{ij} + \partial_k C_{iklj}\partial_l \tag{B-2}$$

Note that $\partial_i$ stands for the derivative with respect to the $xi$ coordinate and $\delta_{ij}$ is the Kronecker delta function defined by $\delta_{ij} = 1$ when $i = j$ and $\delta_{ij} = 0$ when $i \neq j$. The dependence of $C_{iklj}$, $\rho$ on spatial position and $u_i$, $G(\mathbf{x}, \mathbf{x}')$ (Greens function introduced below) on the angular frequency $\omega$ is suppressed for compactness purposes.

The displacement wave field **u** can be represented by the volume and surface (representation theorem) integrals Pike and Sabatier (2002):

$$
\begin{aligned}
u_i(\mathbf{x}') &= \int_V G_{in}(\mathbf{x}, \mathbf{x}')f_n(\mathbf{x}')dV' \\
&+ \int_S \left[G_{in}(\mathbf{x}, \mathbf{x}')n_j c_{njkl}\partial_k' u_l(\mathbf{x}') - u_n(\mathbf{x}')n_j c_{njkl}\partial_k' G_{il}(\mathbf{x}, \mathbf{x}')\right] dS',
\end{aligned}
\tag{B-3}
$$

where the Green's tensor $G_{in}(\mathbf{x}, \mathbf{x}')$ is the the displacement at location $\mathbf{x}$ in the $i$ direction due to a point source $\delta_{in}\delta(\mathbf{x} - \mathbf{x}')$ and is defined by

$$L_{ij}G_{jn}(\mathbf{x}, \mathbf{x}') = -\delta_{in}\delta(\mathbf{x} - \mathbf{x}'). \tag{B-4}$$

The volume integral in equation (B-3) represents the displacement at $\mathbf{x}'$ due to the exciting force $f_n(\mathbf{x}')$ within the volume $V$. The surface integral represents the displacement at $\mathbf{x}$ due to the displacement field $u_n(\mathbf{x}')$ and the associated traction $n_j c_{njkl}\partial_k' u_l(\mathbf{x}')$ along the surface S.

In order to describe scattering its convenient to split the elastic parameters $\mathbf{c}$ and the density $\boldsymbol{\rho}$ into a reference $\mathbf{c}^{(0)}$ and $\boldsymbol{\rho}^{(0)}$ and a perturbation $\mathbf{c}^{(1)}$ and $\boldsymbol{\rho}^{(1)}$ as follows:

$$\begin{aligned} \mathbf{c}(\mathbf{x}) &= \mathbf{c}^{(0)}(\mathbf{x}) + \mathbf{c}^{(1)}\mathbf{x}, \\ \boldsymbol{\rho}(\mathbf{x}) &= \boldsymbol{\rho}^{(0)}(\mathbf{x}) + \boldsymbol{\rho}^{(1)}\mathbf{x}. \end{aligned} \tag{B-5}$$

We shall assume that the solution $\mathbf{u}^{(0)}$ for the reference medium (not necessarily homogeneous) and the associated Green's function $\mathbf{G}^{(0)}$ is known. We can decompose the operator $\mathbf{L}$ defined in equation (B-1) into an operator $\mathbf{L}^{(0)}$ for the reference medium and operator $\mathbf{L}^{(1)}$ corresponding to the perturbation. The total wave field in the perturbed medium for a source distribution $\mathbf{f}(\mathbf{r})$ is given by

$$\mathbf{L}^{(0)}\mathbf{u}(\mathbf{x}) = - \left( \mathbf{f}(\mathbf{x}) + \mathbf{L}^{(1)}\mathbf{u}(\mathbf{x}) \right), \tag{B-6}$$

where

$$L_{ij}^{(0)} G_{jn}^{(0)}(\mathbf{x}, \mathbf{x}') = -\delta_{in}\delta(\mathbf{x} - \mathbf{x}'). \tag{B-7}$$

Using result (B-6), we can use the representation theorem (B-3) for the reference medium taking $\mathbf{f}(\mathbf{x}) + \mathbf{L}^{(1)}\mathbf{u}(\mathbf{x})$ as the effective force, so that the total wavefield is given by

$$\begin{aligned} u_i(\mathbf{x}') &= \int_V G_{in}^{(0)}(\mathbf{x}, \mathbf{x}') f_n(\mathbf{x}') dV' + \int_V G_{in}^{(0)}(\mathbf{x}, \mathbf{x}') L_{nj}^{(1)} u_j(\mathbf{x}') dV' \\ &\quad + \int_S \left[ G_{in}^{(0)}(\mathbf{x}, \mathbf{x}') n_j c_{njkl}^{(0)} \partial_k' u_l(\mathbf{x}') - u_n(\mathbf{x}') n_j c_{njkl}^{(0)} \partial_k' G_{il}^{(0)}(\mathbf{x}, \mathbf{x}') \right] dS'. \end{aligned} \tag{B-8}$$

Note that the first term on the right-hand side is the reference field:

$$u_i^{(0)}(\mathbf{x}) = \int_V G_{in}^{(0)}(\mathbf{x}, \mathbf{x}') f_n(\mathbf{x}') dV'. \tag{B-9}$$

We assume that the reference medium has zero tractions at the surface $S$ so that the last term in (B-8) vanishes. A similar assumption for the perturbed medium implies:

$$n_j \left( c_{ijkl}^{(0)} + c_{ijkl}^{(1)} \right) \partial_k u_l(\mathbf{x}) = 0. \tag{B-10}$$

Using the above equation (B-10) in conjunction with the definition (B-1) for operator $\mathbf{L}^{(1)}$, we get

$$
\begin{aligned}
u_i(\mathbf{x}') = u_i^{(0)}(\mathbf{x}) &+ \boldsymbol{\omega}^2 \int_V G_{ij}^{(0)}(\mathbf{x}, \mathbf{x}')\boldsymbol{\rho}^{(1)}(\mathbf{x}')u_j(\mathbf{x}')dV' \\
&+ \int_V G_{in}^{(0)}(\mathbf{x}, \mathbf{x}')\partial_k' \left( c_{nklj}^{(1)}(\mathbf{x}')\partial_l' u_j(\mathbf{x}') \right) dV' \\
&- \int_S G_{in}^{(0)}(\mathbf{x}, \mathbf{x}')n_j c_{njkl}^{(1)}\partial_k' u_l(\mathbf{x}')dS'.
\end{aligned}
\tag{B-11}
$$

Transforming the volume integral in the second line of equation (B-11) into a surface integral, we obtain the Lippmann-Schwinger equation for the elastic wave scattering Pike and Sabatier (2002):

$$
\begin{aligned}
u_i(\mathbf{x}') = u_i^{(0)}(\mathbf{x}) &+ \boldsymbol{\omega}^2 \int_V G_{ij}^{(0)}(\mathbf{x}, \mathbf{x}')\boldsymbol{\rho}^{(1)}(\mathbf{x}')u_j(\mathbf{x}')dV' \\
&- \int_V \partial_k' \left( G_{in}^{(0)}(\mathbf{x}, \mathbf{x}') \right) c_{nklj}^{(1)}(\mathbf{x}')\partial_l' u_j(\mathbf{x}')dV'.
\end{aligned}
\tag{B-12}
$$

We note that the first and second term on the right-hand side represents the reference and scattered fields, respectively.

## B.2    Born approximation of Elastic Waves

The Born approximation allows us to simplify the Lippmann-Schwinger equation (B-8) and formulate an approximate forward modelling problem that is useful for calculating the seismic reflection data. By assuming that the perturbations are sufficiently small, the approximation is obtained by replacing the total wavefield on the right-hand side of equation (B-8) with the reference field. This means that the Born approximation for the scattered waves states (e.g., Pike and Sabatier, 2002; Červený, 2001)

$$
\begin{aligned}
u_i(\mathbf{x}') = \boldsymbol{\omega}^2 &\int_V G_{ij}^{(0)}(\mathbf{x}, \mathbf{x}')\boldsymbol{\rho}^{(1)}(\mathbf{x}')u_j^{(0)}(\mathbf{x}')dV' \\
&- \int_V \partial_k' \left( G_{in}^{(0)}(\mathbf{x}, \mathbf{x}') \right) c_{nklj}^{(1)}(\mathbf{x}')\partial_l' u_j^{(0)}(\mathbf{x}')dV'.
\end{aligned}
\tag{B-13}
$$

Equation (B-13) is a single-scattering approximation for the scattered wavefield and is valid if the inhomogeneities are small perturbations of the reference (background) medium. For an

isotropic elastic medium, the elastic parameters $C_{ijkl}$ reduces to Lamè's constant $\lambda$ or rigidity $\mu$.

# Bibliography

Abubakar, A., Van Den Berg, P., and Fokkema, J. (2003). Towards non-linear inversion for characterization of time-lapse phenomena through numerical modelling. Geophysical Prospecting, **51**(4):285–293.

Aki, K. and Richards, P. G. (2002). Quantitative seismology. University Science books, 2nd edition.

Alaei, B. (2012). Seismic modeling of complex geological structures. INTECH Open Access Publisher.

Anger, G. (1990). Inverse problems in differential equations, volume **79**. Springer.

Ashcroft, W. (2011). A petroleum geologist's guide to seismic reflection. John Wiley & Sons.

Asnaashari, A., Brossier, R., Garambois, S., Audebert, F., Thore, P., and Virieux, J. (2015). Time-lapse seismic imaging using regularized full-waveform inversion with a prior model: which strategy? Geophysical Prospecting, **63**(1):78–98.

Aster, R. C., Borchers, B., and Thurber, C. H. (2013). Parameter estimation and inverse problems. Academic Press.

Ayeni, G. and Biondi, B. (2010). Target-oriented joint least-squares migration/inversion of time-lapse seismic data sets. Geophysics, **75**(3):R61–R73.

Ayeni, G., Biondi, B., et al. (2011). Wave-equation inversion of time-lapse seismic data sets. In SEG Technical Program Expanded Abstracts, volume **30**, pages 4149–4154.

Ayeni, G., Biondi, B., et al. (2012). Time-lapse seismic imaging by linearized joint inversion–a valhall field case study. In 2012 SEG Annual Meeting. Society of Exploration Geophysicists.

Bansal, R. and Sen, M. K. (2010). Ray-born inversion for fracture parameters. Geophysical Journal International, **180**(3):1274–1288.

Ben-Hadj-Ali, H., Operto, S., and Virieux, J. (2011). An efficient frequency-domain full waveform inversion method using simultaneous encoded sources. Geophysics, **76**(4):R109–R124.

Bertero, M. (1992). Inverse problems in scattering and imaging: proceedings of a NATO advanced research workshop held at Cape Cod, USA, 14-19 April 1991. Hilger.

Bleistein, N., Cohen, J. K., John Jr, W., et al. (2001). Mathematics of multidimensional seismic imaging, migration, and inversion, volume 13. Springer Science & Business Media.

Bouma, A. H., Stone, C. G., et al. (2000). Fine-Grained Turbidite Systems: AAPG Memoir 72, volume **72**. AAPG.

Buland, A. and Omre, H. (2003). Bayesian linearized avo inversion. Geophysics, **68**(1):185–198.

Červenỳ, V. (1992). Ray born synthetic seismograms for complex structures containing scatterers. Journal of seismic exploration, **1**:191–206.

Červenỳ, V. (2001). Seismic ray theory. Cambridge University Press.

Chapman, C. (2004). Fundamentals of seismic wave propagation. Cambridge University Press.

Chopra, S. et al. (2005). Seismic elastic modelling. In 2005 SEG Annual Meeting. Society of Exploration Geophysicists.

Cohen, J. K. and Bleistein, N. (1977). An inverse method for determining small variations in propagation speed. SIAM Journal on Applied Mathematics, **32**(4):784–799.

De Basabe, J. D. and Sen, M. K. (2009). New developments in the finite-element method for seismic modeling. The Leading Edge, **28**(5):562–567.

Downton, J. E. (2005). Seismic parameter estimation from AVO inversion. PhD thesis, The University of Calgary, Department of Geology and Geophysics.

Eaton, D. W. and Stewart, R. R. (1994). Migration/inversion for transversely isotropic elastic media. Geophysical Journal International, **119**(2):667–683.

Farquharson, C. G. and Oldenburg, D. W. (2004). A comparison of automatic techniques for estimating the regularization parameter in non-linear inverse problems. Geophysical Journal International, **156**(3):411–425.

Golub, G. H. and van Van Loan, C. F. (1996). Matrix computations (Johns Hopkins studies in mathematical sciences). The Johns Hopkins University Press.

Hadamard, J. (1923). Lectures on Cauchy's problem in linear partial differential equations. Yale University Press.

Hansen, P. C. (1998). Rank-deficient and discrete ill-posed problems: numerical aspects of linear inversion, volume **4**. Siam.

Hearn, D. and Krebes, E. (1990). On computing ray-synthetic seismograms for anelastic media using complex rays. GEOPHYSICS, **55**(4):422–432.

Ikelle, L. T. and Amundsen, L. (2005). Introduction to petroleum seismology. Investigations in Geophysics No. 12. Society of Exploration Geophysicists Tulsa, OK.

Innanen, K., Naghizadeh, M., Kaplan, S., et al. (2011). Direct inversion of differenced seismic reflection data for time-lapse structural changes. In 2011 SEG Annual Meeting. Society of Exploration Geophysicists.

Jackson, D. D. (1979). The use of a priori data to resolve non-uniqueness in linear inversion. Geophysical Journal International, **57**(1):137–157.

Jackson, D. D. and Matsu'Ura, M. (1985). A bayesian approach to nonlinear inversion. Journal of Geophysical Research: Solid Earth (1978–2012), **90**(B1):581–591.

Jakobsen, M. (2012). T-matrix approach to seismic forward modelling in the acoustic approximation. Studia Geophysica et Geodaetica, **56**(1):1–20.

Jakobsen, M., Keers, H., Ruud, B., Psencik, I., and Shahraini, A. (2010). Waveform inversion of 4d seismic data using the ray-born approximation in the frequency domain. In 72nd EAGE Conference & Exhibition.

Jakobsen, M. and Ursin, B. (2015). Full waveform inversion in the frequency domain using direct iterative t-matrix methods. Journal of Geophysics and Engineering, **12**(3):400.

Johnston, D. H. (2013). Practical applications of time-lapse seismic data. Distinguished Instructor Series, Society of Exploration Geophysicists.

Kelly, K., Ward, R., Treitel, S., and Alford, R. (1976). Synthetic seismograms: a finite-difference approach. Geophysics, **41**(1):2–27.

Kirchner, A. and Shapiro, S. A. (2001). Fast repeat-modelling of time-lapse seismograms. Geophysical prospecting, **49**(5):557–569.

Klie, H. and Toro, W. (2000). Modeling in transversely isotropic media with the acoustic wave equation. In Fifth International Conference on Mathematical and Numerical Aspects of Wave Propagation, pages 168–172. Siam.

Komatitsch, D. and Tromp, J. (1999). Introduction to the spectral element method for three-dimensional seismic wave propagation. Geophysical journal international, **13**(3):806–822.

Komatitsch, D. and Vilotte, J.-P. (1998). The spectral element method: an efficient tool to simulate the seismic response of 2d and 3d geological structures. Bulletin of the seismological society of America, **88**(2):368–392.

Kouri, D. J. and Vijay, A. (2003). Inverse scattering theory: Renormalization of the lippmann-schwinger equation for acoustic scattering in one dimension. PHYSICAL REVIEW-SERIES E-, **67**(4; PART 2):046614–046614.

Krebes, E. (2004). Seismic forward modeling. CSEG Recorder, **30**:28–39.

Lai, C. G. and Wilmanski, K. (2005). Surface waves in geomechanics: Direct and inverse modelling for soils and rocks, volume **481**. Springer.

Lanczos, C. (1961). Linear differential operators, volume **393**. SIAM.

Landrø, M. (2001). Discrimination between pressure and fluid saturation changes from time-lapse seismic data. Geophysics, **66**(3):836–844.

Lecerf, D. and Reiser, C. (2004). High-resolution processing for time-lapse seismic. First Break, **22**(8).

Li, Y., Downton, J., and Xu, Y. (2007). Practical aspects of avo modeling. The Leading Edge, **26**(3):295–311.

Liner, C. L. (2004). Elements of 3D seismology, volume **1**. PennWell Books.

Liu, Y. and Sen, M. K. (2009). Advanced finite-difference methods for seismic modeling. Geohorizons, December, pages 5–16.

Lo, T.-w. and Inderwiesen, P. L. (1994). Fundamentals of seismic tomography. Number 6 in Geophysical monograph series. Society of Exploration Geophysicists.

Ma, Y., Hale, D., Gong, B., and Meng, Z. (2012). Image-guided sparse-model full waveform inversion. Geophysics, **77**(4):R189–R198.

Maharramov, M. and Biondi, B. (2014). Robust joint full-waveform inversion of time-lapse seismic data sets with total-variation regularization. arXiv preprint arXiv:1408.0645.

Menke, W. (2012). Geophysical data analysis: discrete inverse theory:MATLAB edition. Academic press.

Minakov, A., Tengesdal, H., and Keers, H. (2013). Ray-born modeling in acoustic and elastic media. In EGU General Assembly Conference Abstracts, volume **15**, page 5804.

Morse, P. M. and Feshbach, H. (1953). Methods of theoretical physics. 2 volumes. McGraw-Hill Book Co., Inc., New York-Toronto-London.

Moser, T. J. (2012). Review of ray-born forward modeling for migration and diffraction analysis. Studia Geophysica et Geodaetica, **56**(2):411–432.

Pike, E. R. and Sabatier, P. C. (2002). Scattering and inverse scattering in Pure and Applied Science. Academic press.

Plessix, R.-E., Michelet, S., Rynja, H., Kuehl, H., Perkins, C., de Maag, J., and Hatchell, P. (2010). Some 3d applications of full waveform inversion. In 72nd EAGE Conference & Exhibition-Workshops and Fieldtrips.

Prieux, V., Operto, S., Brossier, R., Virieux, J., et al. (2009). Application of acoustic full waveform inversion to the synthetic valhall velocity model. In The Society of Exploration Geophysicists (SEG 2009), volume **28**, pages 2268–2272.

Queißer, M. and Singh, S. C. (2013). Full waveform inversion in the time lapse mode applied to $CO_2$ storage at sleipner. Geophysical prospecting, **61**(3):537–555.

Raknes, E. B. and Arntsen, B. (2014). Time-lapse full-waveform inversion of limited-offset seismic data using a local migration regularization. Geophysics, **79**(3):WA117–WA128.

Ramm, A. G. (2005). Inverse problems: mathematical and analytical techniques with applications to engineering. Springer.

Richard L. Gibson, J. (2008). Seismic models of reflections from attenuating layers, chapter 424, pages 2117–2121. Society of Exploration Geophysicists.

Ricker, N. (1953). The form and laws of propagation of seismic wavelets. Geophysics, **18**(1):10–40.

Robertsson, J. O. and Chapman, C. H. (2000). An efficient method for calculating finite-difference seismograms after model alterations. Geophysics, **65**(3):907–918.

Rüger, A. (2001). Reflection coefficients and azimuthal AVO analysis in anisotropic media. Society of Exploration Geophysicists.

Santos, L. T., Schleicher, J., Tygel, M., and Hubral, P. (2000). Seismic modeling by demigration. Geophysics, **65**(4):1281–1289.

Sarkar, S., Gouveia, W. P., Johnston, D. H., et al. (2003). On the inversion of time-lapse seismic data. In 2003 SEG Annual Meeting. Society of Exploration Geophysicists.

Sato, H., Fehler, M. C., and Maeda, T. (2012). Seismic wave propagation and scattering in the heterogeneous earth, volume **496**. Springer.

Sayers, C. and Chopra, S. (2009). Introduction to this special section: Seismic modeling. The Leading Edge, **28**(5):528–529.

Scales, J. A. and Smith, M. L. (1994). Introductory Geophysical Inverse Theory. Samizdat Press.

Sheriff, R. E. and Geldart, L. P. (1995). Exploration seismology. Cambridge university press.

Simmons Jr, J. L. and Backus, M. M. (1996). Waveform-based avo inversion and avo prediction-error. Geophysics, **61**(6):1575–1588.

Sirgue, L. and Pratt, R. G. (2004). Efficient waveform inversion and imaging: A strategy for selecting temporal frequencies. Geophysics, **69**(1):231–248.

Snieder, R. (2009). A guided tour of mathematical methods for the physical sciences. Cambridge University Press, Cambridge, second edition.

Stolt, R. H. and Weglein, A. B. (2012). Seismic imaging and inversion: Volume 1: Application of linear inverse theory. Cambridge University Press.

Symes, W. W. and Kern, M. (1994). Inversion of reflection seismograms by differential semblance analysis: algorithm structure and synthetic examples1. Geophysical Prospecting, **42**(6):565–614.

Tarantola, A. (2005). Inverse problem theory and methods for model parameter estimation. siam.

Tengesdal, H., Minakov, A., and Keers, H. (2014). Hybrid ray-born and finite-difference full waveform inversion. In 76th EAGE Conference and Exhibition 2014.

Thierry, P., Operto, S., and Lambaré, G. (1998). Fast 2-d ray+ born migration/inversion in complex media. Geophysics, **64**(1):162–181.

Tikhonov, A. N., Arsenin, V. Y., and John, F. (1977). Solutions of ill-posed problems. Winston Washington, DC.

Tura, A. and Lumey, D. E. (1999). Estimating pressure and saturation changes time-lapse AVO data, chapter 423, pages 1655–1658. Society of Exploration Geophysicists.

Ulrych, T. J., Sacchi, M. D., and Woodbury, A. (2001). A bayes tour of inversion: A tutorial. Geophysics, **66**(1):55–69.

Vermeer, G. J. and Beasley, C. J. (2002). 3-D seismic survey design, volume **12**. Society of Exploration Geophysicists Tulsa.

Vesnaver, A., Janex, G., Madrussani, G., Mazzotti, A., Pajchel, J., Stucchi, E., and Williamson, P. (2001). Target-oriented time-lapse analysis by avo and tomographic inversion. In 71st SEG meeting, San Antonio, Texas, USA, Expanded Abstracts, Session INV, volume **2**.

Wang, Y. (2003). Seismic amplitude inversion in reflection tomography. Elsevier.

Weglein, A. B., Araújo, F. V., Carvalho, P. M., Stolt, R. H., Matson, K. H., Coates, R. T., Corrigan, D., Foster, D. J., Shaw, S. A., and Zhang, H. (2003). Inverse scattering series and seismic exploration. Inverse problems, **19**(6):R27.

Wu, R.-S. and Xie, X.-B. (2009). Modeling primaries of acoustic/elastic waves by one-return approximation. The Leading Edge, **28**(5):576–581.

Xu, Y. and Bancroft, J. C. (1997). Joint avo analysis of pp and ps seismic data. The CREWES Project Research Report, **9**.

Yilmaz, Ö. (2001). Seismic data analysis, volume **1**. Society of Exploration Geophysicists Tulsa.

Zhang, H. (2006a). Direct non-linear acoustic and elastic inversion: towards fundamentally new comprehensive and realistic target identification. PhD thesis, University of Houston.

Zhang, M. (2006b). Simultaneous inversion of time-lapse data. Master's thesis, University of Alberta.

Zhang, Z. and Huang, L. (2013). Double-difference elastic-waveform inversion with prior information for time-lapse monitoring. Geophysics, **78**(6):R259–R273.

Zhdanov, M. S. (1993). Tutorial: Regularization in inversion theory. Colorado School of Mines.

Zhdanov, M. S. (2002). Geophysical inverse theory and regularization problems, volume **36**. Elsevier.

Zhou, H.-W. (2014). Practical Seismic Data Analysis. Cambridge University Press.